8-2019

INVESTIGATIONS OF THE STRUCTURE-FUNCTION RELATIONSHIP IN KAINATE RECEPTORS USING FӦRSTER RESONANCE ENERGY TRANSFER

Douglas Litwin

Recommended Citation

Litwin, Douglas, "INVESTIGATIONS OF THE STRUCTURE-FUNCTION RELATIONSHIP IN KAINATE RECEPTORS USING FӦRSTER RESONANCE ENERGY TRANSFER" (2019). *UT GSBS Dissertations and Theses (Open Access)*. 966.
https://digitalcommons.library.tmc.edu/utgsbs_dissertations/966

INVESTIGATIONS OF THE STRUCTURE-FUNCTION RELATIONSHIP IN KAINATE RECEPTORS USING FÖRSTER RESONANCE ENERGY TRANSFER

by

Douglas Bryan Litwin, M.S.

APPROVED:

Vasanthi Jayaraman, Ph.D.
Advisory Professor

Darren F. Boehning, Ph.D.

Shane R. Cunha, Ph.D.

Jeffrey A. Frost, Ph.D.

Irina I. Serysheva, Ph.D.

APPROVED:

Dean, The University of Texas
MD Anderson Cancer Center UTHealth Graduate School of Biomedical Sciences

INVESTIGATIONS OF THE STRUCTURE-FUNCTION RELATIONSHIP IN KAINATE RECEPTORS USING FÖRSTER RESONANCE ENERGY TRANSFER

A

DISSERTATION

Presented to the Faculty of

The University of Texas

MD Anderson Cancer Center UTHealth

Graduate School of Biomedical Sciences

in Partial Fulfillment

of the Requirements

for the Degree of

DOCTOR OF PHILOSOPHY

by

Douglas Bryan Litwin, M.S.

Houston, Texas

May, 2019

Copyright

Sections of this dissertation were based on previously published research.

- Litwin, D. B., R. J. Durham, and V. Jayaraman. Single-molecule FRET methods to study glutamate receptors. *Methods in Molecular Biology -Glutamate Receptors*. Humana Press. 2018; 1941: 3-16 © Springer Nature Switzerland AG.
    - Copyrights for the written article remain with the authors, but JoVE has been granted the exclusive, royalty-free, perpetual use of the article.
- Litwin, D. B., E. Carrillo, S. A. Shaikh, V. Berka, and V. Jayaraman. The structural arrangement at intersubunit interfaces in homomeric kainate receptors. *Scientific Reports*. 2019; 9(1):6969 © Springer Nature Publishing AG.
    - Copyrights for the written article remain with the authors.
- Litwin, D. B., N. Paudyal, E. Carrillo, V. Berka, and V. Jayaraman. The structural arrangement and dynamics of the heteromeric GluK2/GluK5 kainate receptor as determined by smFRET. *Biochimica et Biophysica Acta- Biomembranes*. 2019; DOI: 10.1016/j.bbamem.2019.05.023 © Elsevier B.V.
    - Permission is automatically granted for authors to reuse their work for a dissertation.
- Prakash, P., D.B. Litwin, H. Liang, J. Hancock, V. Jayaraman and A. Gorfe. Dynamics of membrane-bound G12V-KRAS from simulations and single-molecule FRET in native nanodiscs. *Biophysical Journal*. 2019; 116(2): 179-183 © Biophysical Society.
    - Permission is automatically granted for authors to reuse their work for a dissertation.

Dedication

This dissertation is dedicated to my parents:

Bruce Douglas Litwin

and

Mary Bryan Litwin

Thank you for always supporting my curiosity

and providing me with the life and opportunities you have.

Acknowledgements

I would first like to acknowledge my advisor Dr. Vasanthi Jayaraman. Her mentorship, support and motivation were instrumental to my success throughout graduate school. Her knowledge and expertise were crucial to my development as a scientist. I would like to thank her for providing me the opportunity and patience to experience the process of scientific investigation.

I would like to thank my wife, Dr. Jessica Cardenas, for being the best wife imaginable. Thank you for loving and taking care of Isaac and me the way you do. You have been patient and understanding under often unpredictable and chaotic circumstances over the last five years, and I realize that. We have been through a lot during my years as a PhD student and I am grateful for your love and support through it all.

I would like to thank my parents, Mary and Bruce Litwin, for sacrificing so much to ensure I had a privileged life and making me aware of how fortunate we are, and for being so loving and patient. I would like to thank my siblings; Jake, Elizabeth, Bryce and Kirstin Litwin. I would also like to thank my in-laws, Roxie and Dr. Jose Cardenas. I am blessed to have you all in my life. Y’all are the best family; thank you for sticking by my side through my life decisions good and bad, and providing me with unwavering love and support.

I would like to thank my committee members: Dr. Darren Boehning, Dr. Shane Cunha, Dr. Jeffrey Frost and Dr. Irina Serysheva. You have all been great mentors, teachers and friends through this process. The scientific rigor and kindness alike are greatly appreciated.

I would like to thank my labmates: Ryan Durham, Dr. Drew Dolino, Dr. Sana Shaikh, Dr. David MacLean, Dr. Garam Lee, Dr. Vladimir Berka, Dr. Elisa Carrillo, Dr. Nidhi Bhatia, Nabina Paudyal, Dr. Swarna Ramaswamy, Dr. Rita Sirrieh, and Dr. Catie Nurik. You have all been instrumental to my development as a scientist and more importantly kept me sane through the process. Ryan, Drew and Dave, you have been particularly influential to my intellectual development, both scientifically and interpersonally-thank you.

I would like to thank the graduate school faculty and staff past and present: Dr. Eric Wagner, Dr. William Mattox, Dr. Mikhail Bogdanov, Dr. Heidi Vitrac, Dr. Richard Kulmacz, Dr. Ilya Levental, Leticia Zarate, Brenda Gaughan and Lourdes (Bunny) Perez. You have all been so helpful and supportive. Thank you for participating in my education in the ways you have.

I would like to thank current and former HAMBP fellows, faculty and staff. Dr. Theodore Wensel, Vanessa Herrera, Dr. Dan Nguyen, Sarah Alvarado, Dr. Michael Bell, Jake Ezerski. You have been excellent colleagues and friends. Thank you for my funding and the endless training opportunities you provided.

I would like to thank current and past GSBS students and postdocs. Dr. Tré O'Brien, Dr. Nick Parchim, Dr. Romain Harmancey, Jessica Chen, and Scott Collum. You have all greatly contributed the development of my scientific prowess and enjoyment of graduate school.

I would like to thank my past principle investigators and teachers: Dr. Heidi Kaplan, Dr. Philip Lyons, Dr. Penny Morris-Smith, Dr. Donald Musselwhite, Dr.

Millicent Goldschmidt, Dr. Jerry Johnson, Dr. Lisa Morano, and Dr. Kevin Morano.

Thank you all for believing in me and fostering my scientific curiosity.

INVESTIGATIONS OF THE STRUCTURE-FUNCTION RELATIONSHIP IN KAINATE RECEPTORS USING FÖRSTER RESONANCE ENERGY TRANSFER

Douglas Bryan Litwin, M.S.

Advisory Professor: Vasanthi Jayaraman, Ph.D.

Kainate receptors belong to the family of ion channels known as the ionotropic glutamate receptors. Ionotropic glutamate receptors mediate the majority of excitatory synaptic transmission, modulate the release of presynaptic glutamate, and facilitate dendrite formation. Kainate receptors are unique among the ionotropic glutamate receptors in being modulated by sodium ions. They have also been implicated in the development of higher learning and epilepsy. In recent years a wealth of structural data has become available for the AMPA and NMDA classes; however, the structural characterization of kainate receptors has been limited. The work in this dissertation utilizes luminescence resonance energy transfer (LRET) and single molecule Förster Resonance Energy Transfer (smFRET) in order to address this gap in the knowledge. We have characterized the structural arrangement and dynamics of the homomeric (GluK2) receptors and identified structural changes involved in the functional modulation by ions and auxiliary proteins. Additionally, we have characterized the arrangement and dynamics of the heteromeric (GluK2/GluK5). These data will build a

foundation for the full biophysical characterization of kainate receptors; and contribute to the development of subunit-specific modulatory compounds to be used for disease therapies, and for more detailed characterization of brain function at the molecular level.

Table of Contents

List of Illustrations

List of Tables

Abbreviations

ABD	Agonist-Binding Domain
AMPA	α-amino-5-methyl-3-hydroxy-4-isoxazole propionate
ATD	Amino-Terminal Domain
CNS	Central Nervous System
CTD	Carboxyl-Terminal Domain
D1	Upper lobe of the LBD
D2	Lower lobe of the LBD
DDM	*n*-dodecyl-β-D-maltoside
EM	Electron Microscopy
FLIM	Fluorescence Lifetime Imaging Microscopy
FRET	Förster Resonance Energy Transfer
iGluR	ionotropic Glutamate Receptor
LRET	Luminescence Resonance Energy Transfer
LTD	Long-Term Depression
LTP	Long-Term Potentiation
M1	First Membrane-spanning helix of the NMDA receptor
M2	Re-entrant Membrane loop between M1 and M3 of the NMDA receptor
M3	Second Membrane-spanning helix of the NMDA receptor
M4	Third Membrane-spanning helix of the NMDA receptor
MD	Molecular Dynamics
MFD	Multi-parameter Fluorescence Detection
MNG-3	Lauryl Maltose Neopentyl Glycol

MSP	Membrane Scaffold Protein
NMDA	*N*-Methyl-D-Aspartate
PBS	Phosphate-Buffered Saline
PEG	Poly-Ethylene Glycol
PIE	Pulsed Interleaved Excitation
R_0	Förster Radius, the distance at which FRET is half-maximal
S1	Sequence of the ABD prior to M1
S2	Sequence of the ABD after M3
SiMPull	Single-Molecule Pulldown
SMA	Styrene-Maleic Acid
smFRET	single molecule Förster Resonance Energy Transfer
STaSI	Step Transition and State Identification
TCSPC	Time-Correlated Single Photon Counting
TIRF	Total Internal Reflection Fluorescence
TMD	Trans-Membrane Domain

Chapter 1: Introduction

Cell signaling with the speed required for the complex physiology found in vertebrates is made possible through the modulation of an electrical voltage gradient within neurons. These signals are conducted at high speed down neuronal axons where they are sent to downstream neurons at junctions called synapses. At the synapse, the signal can be electrically relayed between neurons or converted to a chemical signal which can then generate an electrical signal in the downstream neuron, known as synaptic transmission.

The voltage gradient utilized for synaptic transmission is created and maintained by numerous classes of ion pumps and channels. These channels and pumps modulate the voltage gradient by displacing ions in (K^+) and out (Na^+ and Cl^-) of the cell which creates net positive charge outside of the neuron. Synaptic transmission can induce both excitatory and inhibitory signals in the receiving neuron. Excitatory reception induces depolarization by allowing Na^+ back into the cell and inhibitory signals induce hyperpolarization by allowing Cl^- to reenter the postsynaptic membrane or K^+ out of the cell. Ionotropic glutamate receptors (iGluRs) are the primary carriers of excitatory signaling and Gamma-aminobutyric acid (GABA) receptors are the primary carriers of inhibitory signaling in the central nervous system (CNS).

Kainate receptors are members of the iGluR family of ion channels which are typically permeable to Na^+, K^+ and sometimes Ca^{2+}. The iGluR family consists of the α-amino-3-hydroxy-5-methyl-4-isoxazole propionate (AMPA), kainate, and *N*-methyl-D-aspartate (NMDA) receptor subtypes. All subtypes assemble as tetrameric proteins composed of a combination of subtype-specific subunits; GluA1-4 for AMPA, GluK1-5 for kainate, and GluN1-3 for NMDA (1, 2). Prior studies have revealed that iGluRs function in the reception of excitatory synaptic signaling, the facilitation and inhibition of presynaptic GABA and glutamate release, and neuronal dendrite formation and growth (2-4).

Although the exact mechanisms behind cognition, learning and memory are not fully resolved, it is well established that iGluRs are critical in these processes. Not surprisingly, iGluRs have been implicated in various disease states including neurological developmental disorders, schizophrenia, autism, and epilepsy (5, 6). This makes iGluRs of particular interest for the development of novel modulatory compounds for therapeutic applications. These novel compounds would not only be of interest to physicians treating patients affected by neurological disorders but would also make it possible for scientists to more accurately study the specific roles of iGluRs in the brain. However, attempts to target iGluRs for the therapeutic intervention of diseases has yielded little progress due to the ubiquitous integration of iGluR function into basal physiological activity. Targeting AMPA, NMDA, and kainate receptors individually has consistently been limited by off-target effects resulting from overlap in their pharmacological profiles. The solution to this issue is to target not only iGluR subtypes but also the different subunit combinations with which subtypes assemble in the brain.

Since the first pharmacological characterization of iGluRs, numerous groups have attempted to identify novel iGluR-modulating compounds (7-15). However, developing methods capable of high throughput screening potential compounds for iGluR modulating activities has been a difficult and time-consuming process. These investigations have yielded a number of compounds with high specificity for iGluR subtypes, particularly the AMPA and NMDA subtypes, but the majority of these compounds have been limited to use in the laboratory. The most promising clinically-relevant compounds produced have been NMDA antagonists including ketamine, memantine, methadone, and dextromethorphan.

While these compounds have proven useful in certain neuropathies, their applications, as with other AMPA and kainate candidate compounds, have been limited by unwanted and/or toxic side effects (16-20). Therefore, given the success of structure-based drug design with other proteins including the NMDA receptor (21-23), it seems likely that a thorough understanding of the structural conformations and solvent-accessible topological chemistries unique to each iGluR subtype will be required to allow for the design of compounds with higher subtype specificity.

Beginning in the early 2000's, researchers began resolving the first structural models of iGluRs. These studies initially resolved crystal structures of isolated extracellular domains and eventually culminated with high-resolution crystallography and cryo-EM models of the full-length proteins (24-32). The vast majority of the full-length models available are of AMPA and NMDA receptors with limited structural data produced for full-length kainate receptors. These structural models have revolutionized our understanding of the mechanics underlying iGluR function. However, uncertainties resulting from the static conditions required for X-ray and electron-based imaging, and functional data produced that conflicts with structure-based interpretations of the dynamic requirements for receptor gating have left many unanswered questions concerning the structural characteristics unique to each subtype (33, 34).

To address this gap in knowledge, the work presented in this dissertation aims to examine the dynamic movements and conformational changes involved in full-length kainate receptor gating and the unique aspects of their functional characteristics, including modulation by ions and auxiliary proteins. The FRET data presented herein seeks to build on prior knowledge available for the structure-function relationship in kainate receptors and resolve the structural and dynamic properties that give rise to the unique structure-function characteristics of kainate receptors.

Chapter 2: Kainate Receptor Function and Physiology

Kainic acid (kainate) is a naturally occurring marine toxin produced by certain species of seaweed. It was historically known that ingestion of kainate induced severe excitotoxic and convulsive responses in mice and humans. In 1974 the first study identifying the excitatory effect of kainate on crayfish muscles was published (35). This study showed that kainate induces excitatory responses in neuromuscular junctions that are nearly identical to those induced by glutamate. It was later discovered that kainate was acting preferentially on a subtype of glutamate receptor that became known as kainate receptors.

Shortly after the first studies on kainate, it was shown that exposure to alpha-Amino-3-hydroxy-5-methyl-4-isoxazolepropionic acid (AMPA) produced similar excitotoxic effects in animals (36). The similar physiological responses resulting from kainate and AMPA exposure were quickly explained by significant overlap in their pharmacological profiles (37) and this overlap was not found with NMDA class receptors. While the pharmacological similarities between the kainate and AMPA receptor have made it difficult to resolve the functional characteristics of each subtype, distinct and unique functional properties have since been identified for kainate receptors.

It was subsequently shown that iGluRs exist in three functional states: resting, active and desensitized. Under resting conditions, the receptor is not bound to agonist and non-conductive. Under active conditions the receptor is agonist-bound and conducts ions. Under desensitized conditions the receptor is agonist-bound and non-conductive. The transitions between these states are described by their activation, deactivation, and desensitization and resensitization kinetics. Activation kinetics describe the receptors speed of response to agonist. Deactivation kinetics describe the speed of channel inactivation under sub-saturating agonist conditions. Desensitization kinetics describe the speed of channel inactivation under saturating agonist conditions, and resensitization kinetics describe the speed at which the receptors recover from the non-active state.

On the post-synaptic neuron, kainate and AMPA receptors function to mediate the fast component of excitatory synaptic transmission. Both kainate and AMPA receptors carry the initial response to presynaptically released glutamate; however, kainate receptors typically have a slower activation and prolonged deactivation kinetics (2). Additionally, kainate receptors show longer rates of recovery from the inactive state. In contrast, NMDA receptors are characterized by a delayed response induced by Mg^+ blocking the ion channel pore, which requires a prior depolarization at the post-synaptic membrane to release (2). These data are not surprising given the high primary sequence homology between AMPA and KARs which is significantly lower between the two and the NMDAR.

Studies characterizing the *in vivo* electrophysiological functions of KARs have been limited due to the lack of specific pharmacological compounds; however, the development of the 2,3-benzodiazepine class of antagonists, which are more selective for AMPARs than KARs, made it possible to characterize the synaptic functions of KARs for the first time. Using these antagonists it was shown that KARs mediate excitatory synaptic transmission in the CA1 region of the hippocampus (38).

Subsequent studies identified their involvement in excitatory synaptic transmission at other hippocampal synapses (39-41), in the retina (42), spinal cord (43), amygdala (44), and cortex (45).

The most interesting finding resulting from these initial studies was that high agonist concentration inhibited presynaptic glutamate release (38). These results hinted that KARs could be localized and functioning pre-synaptically, which was later confirmed by studies showing that KARs are able to inhibit presynaptic glutamate release in the neocortex (46) and cerebellum (47). The presynaptic roles of KARs were expanded when it was shown that KARs can regulate the release of the inhibitory neurotransmitter GABA at hippocampal synapses (48, 49). Additional studies showed that kainate receptors are able to facilitate and inhibit GABA release through metabotropic signaling mechanisms (49, 50). These presynaptic roles of kainate receptors are still not fully resolved yet highlight their potential of regulating excitatory networks in specific regions of the brain.

After being cloned and characterized in greater molecular detail, it was shown that KARs are tetrameric assemblies of subunits GluK1-5. Each subunit was shown to be modular with an amino-terminal domain (ATD), agonist-binding domain (ABD), a transmembrane domain (TMD) and a Carboxyl-terminal domain (CTD). While these studies confirmed that all iGluR have similar architecture, the structure/function relationship of each class remained to be characterized.

KARs function to produce excitatory post-synaptic currents (EPSCs) with different properties through the combination of different subunits in homomeric and heteromeric receptors. GluK1-3 function as homomeric or heteromeric assemblies, while GluK4-5 require co-expression with either GluK1 or GluK2 to form functional channels (1). The homomeric GluK2 receptor has been studied in the greatest detail, however, the GluK2/GluK5 heteromeric receptors are the most commonly expressed KAR in the brain. Interestingly, KAR subunits able to form homomeric channels have a significantly lower affinity for glutamate than those that cannot. This has led to GluK1-3 being termed low affinity and GluK4-5 being termed high affinity KARs.

Different functional properties can also be obtained from mRNA editing, alternative splicing, and post-translational modifications of the receptors. mRNA editing at sites within the transmembrane helices of GluK1 and GluK2 can result in changes of ion permeability (51). Alternative splicing within the GluK1 and GluK2 C-terminal results in endoplasmic reticulum retention of the receptors (52). Phosphorylation of the C-terminal of GluK1 results in receptor internalization, while phosphorylation of the GluK2 C-terminal results in potentiation (2, 53-55). It is also known that SUMOylation of the KAR C-terminal domain can reversibly induce receptor internalization.

While the kainate-mediated EPSCs first found in the CA1 region were small in amplitude, it was later shown that KARs produce significant currents in the CA3 region of the hippocampus and in the cortex (45, 56). Biochemical, pharmacological, and genetic methods have provided some insight into the composition of the KAR subunits within these regions. The GluK1-specific agonist 2-Amino-3-(3-hydroxy-5-tert-butylisoxazol-4-yl) propionic acid (ATPA) revealed that the GluK1 subunit participates in the EPSCs found in the CA1 region. Immunohistochemistry studies have found that GluK2/GluK5 subunits are enriched in the hippocampus and that knockout of either GluK2 or GluK5 significantly reduces kainate-induced EPSCs in the CA3 region of the hippocampus (57, 58).

Importantly, it has been shown that KARs function in long-term potentiation (LTP) and long-term depression (LTD), processes shown to be involved with learning and memory formation (59, 60). It was shown that blocking presynaptic KARs within hippocampal synapses can eliminate LTP (61) while synapses within the perirhinal cortex require KARs for LTD (62). It was additionally shown that inhibition of KAR-induced LTP in the agranular insular cortex reduced anxiety behavior in mice (63).

Not long after the physiological functions of KARs were first being characterized using electrophysiology, KAR knockout models began to be studied. It was surprising to find that kainate receptor subunit knockout phenotypes displayed no severe somatic defects, with the only effects found involving cognition and psychology (57, 64-69). The behavioral studies performed have shown that GluK1 knockout mice display reduced cognition and fear response, and increased anxiety (64, 65). GluK2 knockout mice display reduced sociability, cognition and fear response, an increase in seizures and symptoms of mania (57, 64, 66, 69). GluK4 knockout mice display symptoms associated with depression and mood dysregulation and impaired memory formation (67, 68). Knock out of all kainate receptor subunits (GluK1-5) resulted in compulsive and perseverative behaviors involving grooming, as well as dysfunction in motor functions (70).

The lack of severe somatic defects in kainate receptor subunit knockout mice initially led to limited interest and even questioning of their physiological relevance. However, mRNA expression profiles of iGluRs in the brain showed that while each iGluR subtype has its own unique expression patterns, kainate receptors show enrichment in areas important for learning, behavior, and anxiety (71). Additionally, a recent study identified a gain-in-function mutation in GluK2 that causes severe neurodevelopmental delay and intellectual disability (72). These results corroborated the phenotypes of the knockout models.

The abundance of kainate receptors in these areas, combined with their mild knockout phenotypes and varied functional roles, might position them as the most ideal iGluR subtype for the treatment of neurological disorders, particularly psychiatric and psychological disorders. However, progress on this front will require drugs with the specificity necessary to discriminate between kainate receptors in their various functional roles.

Chapter 3: Functional Modulation of Kainate Receptors

Auxiliary proteins

Through their initial functional characterization, it was discovered that kainate receptors produced currents in heterologous expression systems that differed significantly from kainate receptor currents recorded in native tissue. Kainate receptors expressed in heterologous systems showed rapid activation and deactivation kinetics, while currents recorded in tissue showed rapid activation with prolonged deactivation kinetics (73, 74). The mechanisms contributing to these differences were initially a mystery. However, since that time it has been well established that iGluRs associate with a number of post-synaptic membrane proteins that alter their localization and function (75-77).

Function-modulating auxiliary proteins have since been discovered for AMPA and kainate receptors; there are six Transmembrane AMPA receptor Regulatory Proteins (TARPs) and a Germ cell-Specific Gene 1-Like (GSG1L) protein for AMPA receptors and Neto1 and Neto2 proteins for kainate receptors (77-79). Currently no auxiliary proteins are believed to be NMDA receptor-specific. Neto1 was initially thought to modulate NMDA receptors (80), but was later shown to be specific to kainate receptors (81). Neto2 was discovered through co-immunoprecipitation experiments and was found to increase the function by delaying the onset of deactivation in kainate receptors (77).

The functional effects of Neto1 and Neto2 on kainate receptors have been extensively tested in heterologous systems and show a gain in function that varies according to the kainate receptor subunit composition (77, 81-83) (84). The gain in function induced by Neto co-expression results in kinetics with delayed onset of deactivation and desensitization. These currents behave more similarly to currents obtained from tissues. These studies have refined our understanding of the *in vivo* functional properties attributed to kainate receptors, but it is worth noting that studies on kainate receptors in tissue are hampered by the difficulty of isolating AMPA receptor and kainate receptor currents. This is an area that would specifically benefit from advances in iGluR-modulating compounds that have high specificity.

Currently the structure of Neto proteins has not been solved. It has been shown biochemically that both Neto proteins consist of two N-terminal extracellular complement subcomponents Clr/Cls, Uegf, Bmp1 (CUB) domains followed by a low-density lipoprotein (LDL)-like domain, a transmembrane region, and a C-terminal intracellular domain. Studies have shown that the CUB and LDL domains are involved in the modulation of kainate receptors and that the second CUB domain is the most influential on receptor function (81, 85). The transmembrane region is believed to contribute stability to the Neto-kainate receptor interaction and the C-terminal is known to be involved in trafficking (86).

While there are no structural data available for Neto proteins, there are a number of studies characterizing the structure of other CUB- and LDL-containing proteins (87-97). These studies have shown that, 1) CUB domains consist of anti-parallel beta sheets with conserved disulfide bridges and a conserved tyrosine-glutamic acid-aspartic acid-aspartic acid (YEDD) motif, and 2) CUB domains mediate a variety of protein-protein interactions that are amongst classes of proteins that are important for developmental regulation. The acidic YEDD motif has been shown to be the mediator of protein-protein interactions in a variety of other proteins and likely binds to a basic pocket within the agonist-binding domain or transmembrane linker regions of the kainate receptor. A similar acidic motif has been identified for AMPA auxiliary proteins (98, 99).

While the majority of our current understanding of the structure of Neto proteins is derived from studies performed on homologous proteins, a coherent picture of the structure-function relationship can be conceptualized. The functional data currently available for Neto protein truncations make it clear that like other homologous proteins, Neto modulation is mediated by extracellular CUB domain interactions. However, the full structure-function relationship between kainate receptors and Neto proteins cannot be fully resolved until high-resolution structural models of the receptor complex are available.

Monovalent ions

iGluRs are known to be functionally sensitive to extracellular ion concentration. NMDA receptors are inhibited by zinc (100, 101), while AMPA and kainate receptors can be inhibited or potentiated by divalent ions such as calcium, barium, magnesium, and zinc (102-109). However, kainate receptors are unique by being modulated by the monovalent ions sodium and chloride (78, 110-115).

The effects of sodium modulation have been well characterized in the homomeric GluK2 receptor with very few studies reported on heteromeric kainate receptors. It has been thoroughly shown that GluK2 homomeric receptors require 150 mM NaCl for glutamate-induced currents and replacement with other monovalent cations like Cs^+ nullifies function, reducing currents by 80-90% as compared to Na^+-containing currents (116). Heteromeric GluK2/GluK5 receptors are also sensitive to CsCl replacement although to a lesser degree with currents reduced by 65-75% (116). Molecular dynamic simulations suggest that it is the displacement of the Na^+ ion from the ABD dimer interface that initiates transition from the active to desensitized state (117). Additionally, it has been shown that co-expression of Neto2 with both homomeric and heteromeric receptors reduces their sensitivity to cations. Co-expression with homomeric GluK2 showed a 63% reduction in currents and heteromeric GluK2/GluK5 showed a 46% reduction in current, as compared to their corresponding Na^+ currents (118).

There are now many studies characterizing the ion sensitivity of KARs in heterologous systems and precious few on native receptors. However, these studies have established that homomeric, heteromeric, and auxiliary protein-associated kainate receptors all require 150 mM Na^+ ions in order to exhibit a normal response to glutamate. Additionally, it has been shown that cultured hippocampal cells (116) display kainate receptor-mediated ion sensitivity and that the concentration of sodium ions in the synaptic cleft is predicted to drop by as much as 40 mM during normal synaptic transmission (119). Therefore, it is hypothesized that the sensitivity of kainate receptors to synaptic sodium concentration would act as a feedback mechanism in which reduced synaptic sodium levels in an overactive synapse would cause the kainate receptors to become unresponsive to glutamate release (115).

Unfortunately, this hypothesis will be difficult to test in native systems, however, a mechanism of this nature should not be discounted.

There are now several converging lines of abductive evidence for a physiological role involving the modulation of KARs by ions. First, mathematical modeling of the ion flux during normal synaptic activation produced a conservative estimate of a 40 mM decrease in Na^+ concentration (119). This would place the affinity of KARs for Na^+ within the dynamic range of ion flux at the synapse. Second, it is unlikely that a relationship of this nature would be retained throughout evolution without conferring some kind of advantage to the animal's phenotype. Third, there are several other classes of channels and receptors that functionally respond to flux in Na^+ ion concentration on either the extra- or intercellular membrane (120-123). Therefore, it seems plausible that future experiments will show that the dependence of KARs on Na^+ concentration is a mechanism which adds to the complexity found in the systems regulating excitatory signaling at certain synapses.

Chapter 4: Kainate Receptor Structure

Kainate receptors, like all iGluRs, are tetrameric proteins with each subunit comprising two large extracellular domains, a transmembrane channel and intercellular C-terminal domain (**Figure 1**). They form functional homomeric and heteromeric proteins, although the most commonly expressed KARs are heteromeric. Based on photobleaching and crystallography studies of the isolated ATDs, the stoichiometry of heteromeric GluK2/K5 KARs is believed to be 2:2 with GluK2 mediating ATD dimer-dimer interactions (124, 125).

Each subunit is composed of domains that are modular in architecture and are structurally and functionally distinct: the extracellular amino-terminal domain (ATD), the extracellular agonist-binding domain (ABD), the transmembrane domain (TMD), and the intracellular carboxyl-terminal domain (CTD). A unique architectural characteristic of iGluRs is termed domain swapping, which involves asymmetry in which subunits associate within the ATD and ABD dimer pairs (**Figure 1**). Linker regions connect the ATD to the ABD, and the ABD to the TMD. The structure and function of the individual domains will be discussed in greater detail below.

Amino-terminal domain

The ATDs of the kainate receptor are positioned above the ABDs on the extracellular side of the membrane (**Figure 1**). They are preceded in the open reading frame only by a membrane localization peptide signal sequence. These are the largest

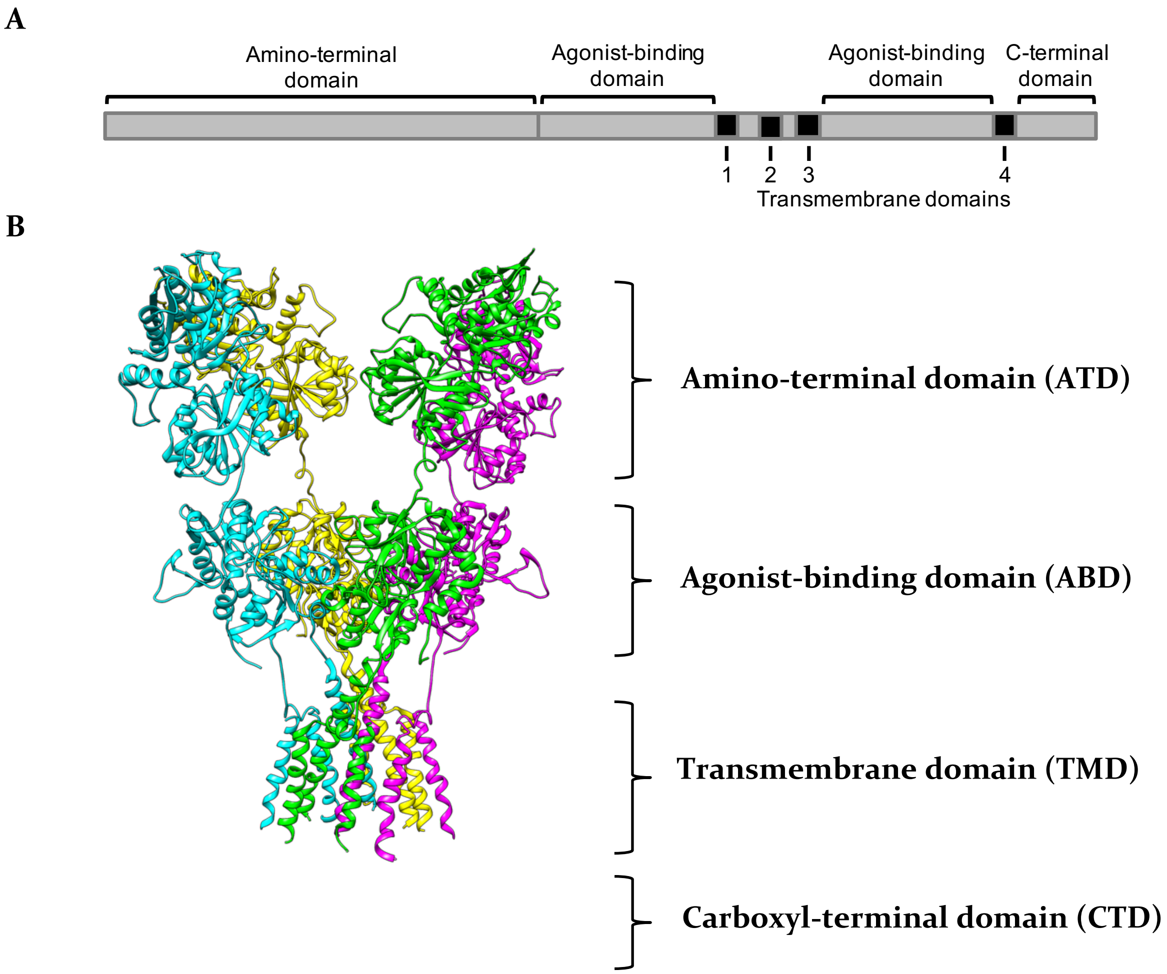

Figure 1. Structural model of the homomeric GluK2 receptor.

(A) Architecture of the GluK2 primary sequence. (B) The homomeric kainate receptor shown under glutamate-bound conditions with each subunit individually colored. The modular domains are labeled, and the carboxyl-terminal domain is not shown as it has not yet been resolved. The image is derived from PDB:5KUF resolved using cryo-EM (29).

domains within the KAR and have the most diversity in primary sequence (126); however, their functional roles have been difficult to resolve.

Several studies have shown that the individual KAR ATDs are arranged as bi-lobed clamshell-like structures composed of an R1 upper lobe and R2 lower lobe (26, 29). These subunits assemble into dimers to form the dimer of dimer architecture found in all iGluRs. The similarities of the ATDs to metabotropic glutamate receptor agonist-binding domains initially left researchers looking for additional ATD specific ligands; however, no ATD specific modulating ligands have been found for KARs.

While ATD allosteric modulation of receptor function has been shown in the NMDAR, no allosteric role has been shown for KARs or AMPARs. This led to the idea that the main role of the ATD involves the initiation of assembly and likely determines the subunit arrangement of the receptor. This was supported by many studies showing that the affinities of the various subunit ATD dimers coincide with the combinations of subunits that form functional channels (127-129), and studies showing which subunits likely mediate heteromeric KAR ATD dimerization (125). While these data support the role of ATDs in receptor assembly, it has also been shown that complete deletion of the ATD in both KARs, AMPARs and NMDARs has no effect on receptor assembly or function in heterologous systems (130, 131). This would suggest a different primary role for the ATD in receptor function.

Following these initial studies, functional roles were identified for KAR ATDs involving receptor and auxiliary subunit localization. Studies have shown that while GluK2 subunits localize to the membrane independent of auxiliary proteins, the surface expression of auxiliary proteins Neto1 and Neto2 depend on GluK2 ATD-Neto interactions (86). Additionally, GluK1 shows an ATD dependent increase in surface expression in the presence of Neto1 and Neto2 (132). This suggests that KAR ATDs are associating with Neto proteins and that interaction can direct receptor and auxiliary protein localization. Interestingly, the localization of GluK1 can also be affected by the membrane signal sequence even after being cleaved (133). These data point to the role of ATDs in receptor and auxiliary protein localization; however, it is possible that additional roles remain to be characterized.

While structural studies of the isolated ATDs have shown that KAR ATDs have a similar architecture as the closely related AMPARs, differences were found when full length receptor models became available. While both the AMPA and kainate receptor showed a compact and coupled arrangement between ATD dimer pairs in the apo state, three classes of arrangements were observed in the glutamate-bound state of the AMPAR with varying degrees of decoupling between the ATD dimer pairs (26). This decoupling was not found in the full-length KAR models of the glutamate-bound state (26, 29). The glutamate-bound state KAR models showed only small ATD rotations relative to the antagonist-bound state. The AMPA ATD decoupling has since been confirmed with smFRET studies (134); however, currently there are no complementary studies available characterizing the conformational dynamics of KAR ATDs in the full-length receptor.

Agonist-binding domain

The agonist binding domain resides between the ATD and the TMDs in the extracellular space (**Figure 1**). As described by name, the ABD is responsible for binding agonists and initiating the process of activation. It is connected to the ATD and TMD layers through linker regions that, in the case of the TMD, transfer conformational changes to the pore region to activate the channel. It was shown biochemically that the interface within the ABD dimer pairs plays a significant role in receptor kinetics, but it took full length iGluR models to identify what the structural implications of this interface involve. While it is now believed that decoupling between the dimer pairs is the driver of the desensitization process, there have been studies that question the nature of the decoupling needed for receptor function (33).

The ABD maintains the highest degree of primary sequence homology among the iGluR subtypes and the glutamate coordinating residues are maintained between all three classes, R492, T659 and E507 in GluK2. Similar to the ATD, the ABD is arranged in a bi-lobed configuration. The ABD architecture resembles a clamshell with a cleft that clamps down on agonists, leading to closure of the cleft. The ABD is composed of two peptide segments within the primary structure named S1 and S2. The S1 segment connects with the ATD and terminates at the first transmembrane helix while the S2 segment is positioned between two of the transmembrane helices. The tertiary folding structure of the S1 and S2 segments results in an upper D1 and lower D2 lobe that comprise the clamshell structure.

Structural studies initially characterized the isolated ABDs of the various KAR subtypes which gave valuable insight into their role in receptor gating. These studies showed that different ligands impose varying degrees of cleft closure in the different subunits that correlate with their efficacy (135-140). Subsequent studies using LRET and smFRET on the all three receptor subtypes confirmed the agonist induced cleft closure (141). These studies also identified the sites responsible for the ion sensitivity found in KARs.

Studies characterizing the isolated ABD of GluK1 and GluK2 using X-ray crystallography identified a Na^+ binding pocket driven by atomic interactions between the Na^+ ion and residues Q509 and K516 (113). Not surprisingly, this pocket was found to reside at the ABD dimer interface and highlights the importance of this interface. Subsequent molecular dynamic simulations showed that the unbinding of Na^+ from this pocket likely induces the desensitization process in KARs, and that with Na^+ present significantly more energy is required to separate ABD dimers (117, 142).

The importance of the ABD dimer interface was further highlighted by separate studies characterizing the effect of varying mutations within the dimer interface of GluK2. These studies identified point mutations that both delayed (143) and eliminated desensitization (144). Most importantly, they showed that introduction of a positively charged lysine residue at site D776 in GluK2 induced constitutive activity in the receptor. These were intriguing results that were later hypothesized to further explain Na^+ sensitivity in KARs. Later, MD simulations showed that the lysine introduced at position 776 can potentially occupy the Na^+ binding pocket and confer stability between the dimer pairs that prevent decoupling, and entrance into the desensitized state (117).

Importantly, the structural arrangement of the ABD as determined using isolated domains was subsequently verified by full-length structures of the AMPA, kainate and NMDA receptor. However, while there has been a plethora of full-length receptor models produced for the AMPA and NMDA classes, full-length kainate receptor models have been difficult to obtain. To date there is a single PDB deposited in the Research Collaboratory for Structural Bioinformatics (RCSB) structural database for the antagonist-bound state and two PBD deposited for the agonist-bound state (26, 29). The antagonist-bound studies could only produce a low resolution (21 Å) electron density map in which previously resolved crystal structures of the isolated ABD were fit (29). The two agonist-bound models are nearly identical showing full decoupling of the ABD dimers, moving to almost four-fold symmetry within the ABDs.

These structures confirmed many previous findings and have collectively been used to construct models for the gating mechanism of iGluRs. It is believed that binding of agonist induces cleft closure at the ABD, which causes strain on the TMD linkers, leading to channel activation. Once activated, the dimer interface within the ABD dimers maintains the open channel conformation until that interface gives way and decouples; KARs being unique in requiring the unbinding of ions for decoupling to proceed. Once the ABDs decouple, the strain is relieved from the TMDs and the channel closes, leading to desensitization.

As previously mentioned, the decoupling process is now believed to be the mechanism initiating desensitization. There is clear evidence for this being the case; however, structural models of the full-length AMPA and KARs have shown vastly different conformations under desensitized conditions. Studies of the homomeric GluA2 show three classes of desensitized conformation with varying degrees of decoupling (26). Additionally, a study characterizing the effect of crosslinks made between AMPAR ABD dimers showed that decoupling is not required for normal receptor function (33).

Therefore, the question of decoupling and the conformations that the KAR ABDs occupy in various conditions remains unclear. The apo state full length models leave assumptions about dynamics resulting from low resolution electron densities, while the agonist-bound state differs significantly from agonist-bound AMPA structures. These questions will be further addressed in this dissertation.

Transmembrane domain

The transmembrane domains of iGluRs are responsible for forming the channel pore in which ions flow and conferring selectivity to which ions are allowed to pass through the pore. Before detailed iGluR structural models of became available, their transmembrane topology was predicted using classical biochemical techniques with remarkable precision. These studies used glycosylation and protease protection assays to determine that despite there being four TM regions predicted from analysis of iGluR primary sequence, there were likely only three transmembrane helices in the mature protein (145, 146). These findings were later confirmed by structural models.

Structural models of the AMPAR first showed that the TMDs are composed of three transmembrane helices, M1, M3 and M4, and one membrane reentrant loop M2. The architecture of the TMD is arranged in pseudo four-fold symmetry and have high primary sequence homology with both K^+ channels and bacterial GluR0 K^+ selective channels (2). The transmembrane helices anchor the receptor to the membrane and play a critical role in channel function.

The pore is formed by the M2 loop, lining the inner cavity, while the M3 helix line the outer pore cavity (24). The apex of the M2 reentrant loop harbors residue Q590 which is known to be commonly RNA edited to an arginine residue. RNA editing at this cite renders the channels impermeable to Ca^{2+} ions, which is critical for Ca^{2+} induced intercellular signaling mechanisms (147). The M1 helix runs exterior to the pore forming M2 loop and M3 helix and is likely key structural support, although mutations with the M3 helix have been found that effect receptor function and cause intellectual impairment (72). Surprisingly, the intracellular loop connecting the M2 loop and M3 helix in the GluK5 subunit has been shown to contain a trafficking signal that retains the receptor in the ER (148). The M1 and M3 helix with the M2 loop forms the channel domain and this architecture is well conserved through evolution (24).

The M4 helix lies peripheral to the pore domain and is unique to eukaryotic glutamate receptors (24, 149). It encases the pore domain and interacts with the M3 helix of adjacent subunits. Given its recent appearance in evolution, the function of the M4 helix has been of interest; however, studies of the M4 helix in AMPA and NMDA have shown mixed results. It was shown that in the AMPA receptor the M4 helix is involved only in receptor assembly, while it is not critical for assembly in NMDA but shows effects on gating kinetics (149). Currently no studies are available characterizing the M4 helix in KARs directly.

While the role of the TMD in channel pore formation seems straight forward, studies have also found that the linker regions connecting the M3 helix to the ABD are critical in modulation by Neto proteins. These studies found residues in this linker region that when mutated either attenuate or abolish Neto modulation and reduce the ion sensitivity of both homomeric and heteromeric KARs (118). These data suggest a significant role for the M3 linker in auxiliary protein modulation and it is likely that the TMDs play additional roles in the KAR-Neto interaction; however, further studies will be required to fully resolve the mechanism of interaction and modulation for Neto proteins.

C-terminal domain

The C-terminal domain has been the most difficult to resolve structurally among all iGluRs. Due to high structural dynamics, it has not been fully resolved using imaging techniques. It is classified as a disordered region that mediates protein-protein interactions, receptor localization and can modulate function through post-translational modifications.

Similar to the ATD, trafficking and localization roles have been identified for the C-terminal domain. It is now understood that alternative splicing and post-translational modifications are able to affect the subcellular localization of KARs. It has been shown that GluK2 harbors a motif of basic amino acids (CQRRLKH) within the C-terminal domain that allows for exit from the endoplasmic reticulum (150), and GluK5 harbors a similar basic motif (RRRRR) that promotes retention in the ER (151). It is known that the CTDs of KARs are commonly modified through alternative RNA splicing which can either add or remove these trafficking motifs; therefore, it is believed that alternative splicing regulates the surface localization of KARs in different brain regions.

The effects of the CTD on receptor localization were also highlighted by studies showing that palmitoylation, phosphorylation and SUMOylation effect receptor surface expression. Palmitoylation of the GluK2 C-terminal domain at C858 and C871 promotes surface localization of the receptor (152). Phosphorylation of serines 879 and 885 on the GluK2 and GluK3 C-terminal domain reduces surface localization of the receptors. It was additionally shown that SUMOylation of GluK2 K886 can reversibly mediate GluK2 surface localization (153).

The CTD has been shown to regulate receptor localization though a variety of protein-protein interactions. It has been well established that the CTD mediates interactions important for localization, post-translational modification and receptor kinetics including but not limited to: CASK, GRIP, GRIP2, mLIN-10, PICK1, PSD95 SAP97, Shank3, Syntenin, Actinfilin, Contactin, Dynamin-1, Dynamitin, Profilin, SUMO, and Calmodulin (2).

Phosphorylation sites within the C-terminal domain have also been found that directly affect KAR function. Phosphorylation at serines 825 and 837 on GluK2 results in potentiation of receptor currents (2). Phosphorylation of site Y590 on GluK2 results in potentiation and increased KAR mediated intercellular $Ca2^+$ signaling (154). Additional phosphorylation sites have been found on GluK1, GluK2 and GluK4; however, testing the functional effects remains to be done.

The structural conformations and dynamics that produce the unique functional characteristics previously described in the scientific literature for KARs will be more closely examined in the following chapters.

Chapter 5: Förster Resonance Energy Transfer in Structural Biology

This chapter is based upon research originally published in *Methods in Molecular Biology*. Litwin, D. B., R. J. Durham, and V. Jayaraman. Single-molecule FRET methods to study glutamate receptors. *Methods in Molecular Biology -Glutamate Receptors*. Humana Press. 2018; 1941: 3-16 © Springer Nature Switzerland AG.

The first biological X-ray crystallography experiments characterizing myoglobin and hemoglobin not only opened our eyes to the relation of function and form in biology, but also revealed the utility of structural biology for studying the evolutionary origins of proteins and for designing useful drugs. X-ray crystallography and cryo-electron microscopy have since emerged as the front runners in the field of structural biology and have provided new insight into all fields of biological science. These techniques will without question continue to lead the way in structural biology. They both, however, suffer from the limitation that they lack the ability to provide the complete structural landscape, dynamics in terms of transitions between states and energetics of transitions between states. This limitation in current methods has created a niche for studying the structure of unresolvable molecules in addition to validating and studying the true dynamics of previously resolved X-ray and cryo-EM models (155, 156). Fluorescent spectroscopy, including Luminescence Resonance Energy Transfer (LRET) and single-molecule fluorescent resonance energy transfer (smFRET), have emerged as the leading methods for this role (134, 157, 158).

smFRET has become of particular interest to groups studying highly dynamic proteins and proteins composed of multiple domains acting in concert to perform mechanically complex motions. Initial efforts have focused on characterizing the structure of DNA/RNA molecules, DNA/RNA protein complexes, enzymes, signaling proteins, and ion channels (134, 157-174). LRET is a complementary FRET method useful for characterizing large scale conformational arrangements of proteins near native conditions. iGluRs are a family of ion channels that serve as a perfect subject for smFRET and LRET studies (134, 155-158, 164, 170). iGluRs are multimeric, have four domains with little functional overlap, operate with millisecond kinetics, and have previously-resolved X-ray and cyro-EM models.

iGluRs are tetrameric proteins with two extracellular domains, a transmembrane domain (TMD), and an intercellular C-terminal domain. iGluRs are divided by their selective agonists into AMPA, kainate, and NMDA subgroups, and some subgroups can express as homomers or heteromers depending on the subunits used. The extracellular amino terminal domain (NTD) and ligand binding domain (LBD) are of particular interest for smFRET studies due to the complex rearrangements proposed during the operation of the protein. smFRET and LRET are complementary techniques where LRET is able to monitor the average distance between two fluorophores in an ensemble of molecules and smFRET is able to characterize the distance and changes in distance at a single molecule level. In this chapter we will discuss the approach to and execution of smFRET and LRET to study the conformational dynamics of iGluRs.

Förster resonance energy transfer

Förster (or fluorescent) resonance energy transfer (FRET) is a term describing the non-radiative transfer of energy from a donor fluorophore to an acceptor fluorophore. This relay of energy relies on the overlap of the donor and acceptor spectra, specifically that the emission of the donor overlaps with the excitation of the acceptor as seen in **Figure 2**.

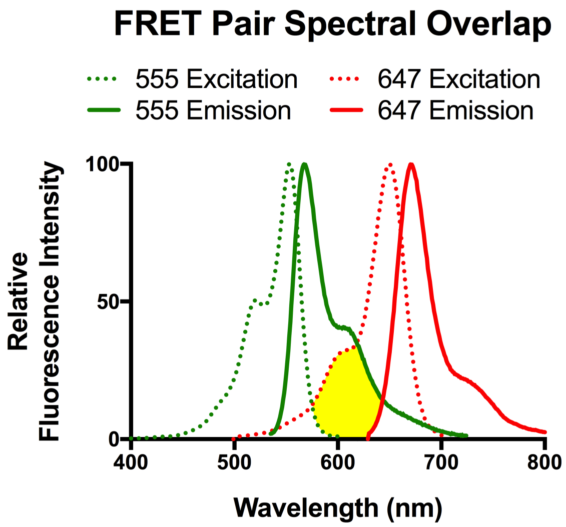

Figure 2. Excitation and emission spectrum of Alexa 555 and Alexa 647.

Spectral data for the excitation (Dotted) and emission (Solid) wavelengths of Alexa 555 (Green) and Alexa 647 (Red).

This phenomenon is distance-dependent where the closer the fluorophore pairs are in space the more likely they are to FRET. The efficiency of energy transfer is related to the inter-dye distance (R_{DA}) and the distance of half-maximal energy transfer for a given fluorophore set (R_0), as seen in equation 1. The effective distance of FRET for fluorophores ranges between 10 and 100 Angstroms, making FRET ideal for measuring distances at the protein level.

$$\boldsymbol{E = \frac{1}{1 + (R_{DA}/R_0)^6}}$$

Eq. 1

When choosing a fluorophore pair for a FRET experiment the most important factors to consider are the distance intended to be measured and the R_0 of the fluorophore pair. The factors contributing to the R_0 of a fluorophore pair are the orientation factor, k; the quantum yield of the donor, Φ_D; the spectral overlap integral, J; and the refractive index of the media, n. The relationship between these values and the R_0 is shown in equation 2. There are many detailed reviews on the physics of FRET if additional information is needed (175).

$$\boldsymbol{R_0 = \left(\frac{8.785 \times 10^5 \times k^2 \times \Phi_D \times J}{n^4}\right)^{1/6}}$$

Eq. 2

Luminescence resonance energy transfer

LRET is a FRET based technique adapted to utilize organic fluorophores attached to chosen sites within a protein. The measurement is conducted on a population of molecules, typically still retained within the cell membrane, while the sample is kept near native temperature and ionic strength. The disadvantage of LRET, similar to traditional FRET experiments, is that a measurement is made on a large population of molecules and the signal obtained is an ensemble their collective behavior. This is useful when looking at large protein movements and proximity; however, these measurements provide an ensemble average and the complete structural landscape along with transitions between the states cannot be resolved.

Single-molecule Förster resonance energy transfer

In order to circumvent the previously mentioned limitations of traditional FRET and LRET experiments, total internal reflection microscopy (TIRF), 2-photon excitation microscopy, and confocal microscopy have been adopted to bring measurements to the single molecule level of both immobilized and freely diffusing molecules as well as in living cells.

These advantages of smFRET have vastly improved our ability to characterize sub-millisecond dynamics in protein, DNA, and RNA in addition to resolving protein subunit stoichiometry. However, collecting data with such detail does not come without its caveats. Data analysis has become the most difficult part of smFRET and methods for collecting and analyzing data have had to evolve. The advent of multiparameter fluorescence detection (MFD), time correlated single photon counting

(TCSPC), pulsed interleaved excitation (PIE), and fluorescence correlation spectroscopy (FCS) have vastly improved the potential quality of smFRET data, discussed further in the data analysis section. Instruments capable of collecting data using MFD, FCS, PIE and TCSPC simultaneously are now available. The collective use of these techniques has greatly improved our ability to resolve the inherent complications of fluorophore photophysics and movements from true FRET signal (176). In this chapter we will focus smFRET and LRET measurements using confocal imaging and lifetime-based measurements respectively.

Experimental design

The design of LRET and smFRET experiments are similar. Any requirement unique to one or the other will be noted. When designing a LRET or smFRET experiment studying iGluRs, the labeling strategy used will depend on the subunit being studied and the intended measurement. The main design step is site selection and considerations here will be the subunit arrangement, distance to be measured, and fluorophore pairs.

In a heteromeric iGluR such as the NMDA receptor there will be two sets of the subunits arranged in a defined orientation. By taking this into account it is possible to pick a surface-exposed amino acid position on either of the subunits used that is 0.5-1X the R_0 of the fluorophore pair. In this case labeling with a site-specific cysteine is recommended. For example, in **Figure 3** the heteromeric NMDA receptor is shown with transmembrane residues selected to measure the change in distance across the axis of the pore. Only the highlighted residues will be labelled and measured.

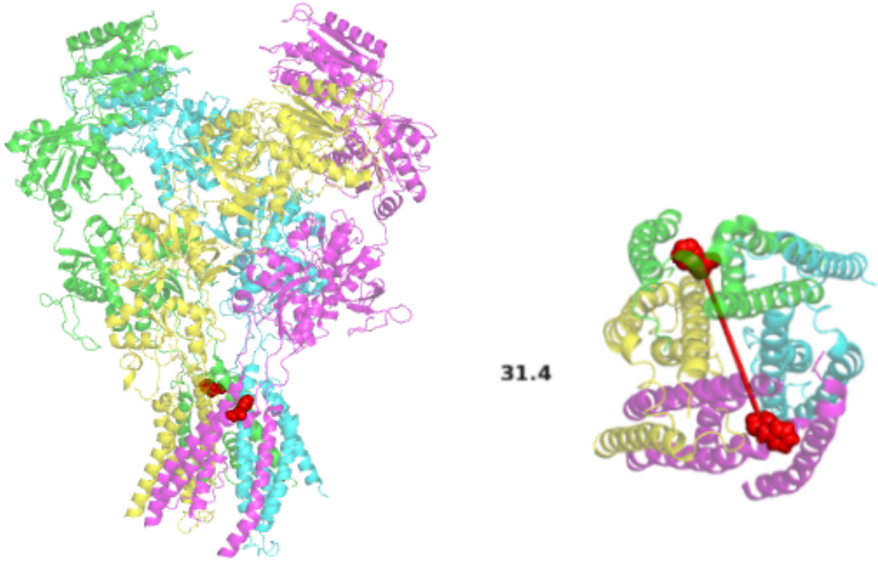

Figure 3. Model of the NMDA receptor showing an ideal FRET measurement in a heteromeric receptor.

A structural model of the NMDA receptor showing phenylalanine 554 (Red) as the fluorescent labeling site for measurements across the ion pore (PDB:5UP2) *(27)*, side view (left) and top view (right).

If using a homomeric iGluR such as in homomeric AMPA receptors, choosing sites for study could be more complicated. This is the result of having the site of interest on all four subunits. In this case, it is required that the site of interest has one high FRET distance 0.5-1X the R_0 and one distance ideally well above the R_0 of the fluorophore pair for a given state. As seen in **Figure 4**, the site chosen will have a primary FRET distance of 41 Å with an additional distance of 64 Å across dimer pairs. This ensures that the main FRET component, 41 Å, is 0.5-1X the R_0 and will be easily resolved from the longer component. In this chapter we will focus on the use of heteromeric iGluRs.

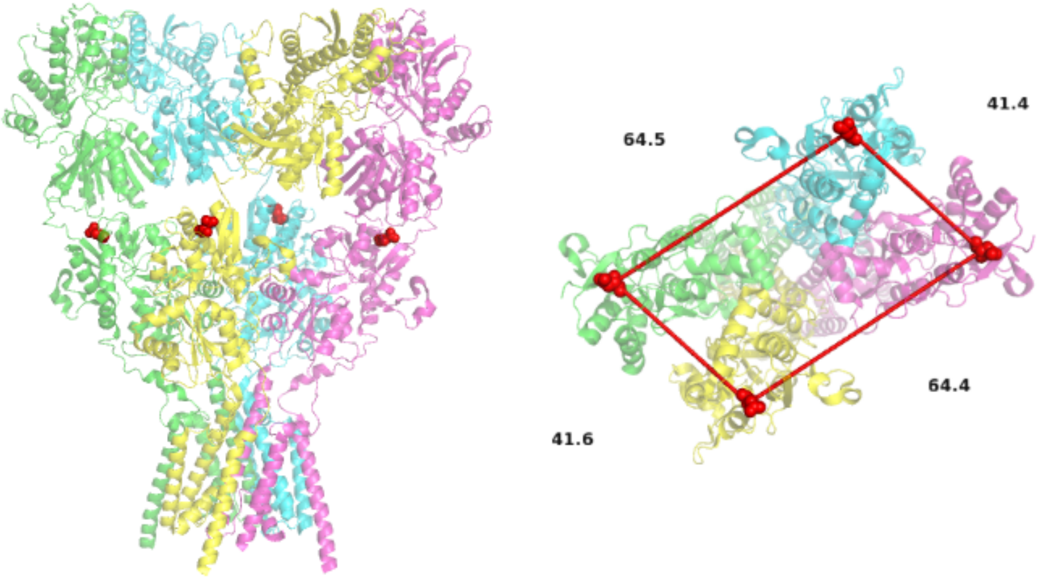

Figure 4. Model of the AMPA receptor showing an ideal FRET measurement in a homomeric receptor.

A structural model of the AMPA receptor showing aspartic acid 473 (Red) as the fluorescent labeling site for measurements between the LBDs (PDB:5VHZ) *(28)*, side view (left) and top view (right).

When studying iGluRs using smFRET, immobilizing the protein on slide via antibody pull-down is preferred. Any antibody with high specificity will work; it is recommended, however, to introduce an affinity tag at the C-terminus to minimize the effect of antibody binding on protein function. When using a new antibody it is critical to run western blots to confirm specificity of the antibody. When performing LRET, antibodies are only required for validation of expression.

Cysteine labeling

The best option for fluorophore labeling for both LRET and smFRET is by introducing a cysteine at the site of interest. This allows use of many commonly available thiol-reactive fluorophores and retains high expression levels. This does however require that all the native non-disulfide bonded cysteines be mutated to provide a clean background. Once this is achieved, the expression and function of the cysteine-less construct must be verified. When approaching the design of an experiment it is ideal that one choose sites that will show a change in distance and will also have one effective FRET distance. It is not always possible to achieve the ideal labeling strategy in every region of the protein, or the measurement may need to be made within the subunit itself. If either of these is the case, utilizing unnatural amino acids allows for additional site specific labeling.

Unnatural amino acid labeling

Unnatural amino acids are advantageous in that one retains the native coding sequence of the protein; however additional plasmids must be maintained for use and expression of the protein needs to be verified by western blotting and function of the protein verified. The principle behind utilizing unnatural amino acids is using a tRNA and aminoacyl-tRNA synthetase that have been artificially evolved to suppress the amber stop codon (TAG). The TAG can be inserted by mutagenesis into any position along the protein and, when co-transfected with plasmids containing the tRNA and aminoacyl-tRNA synthetase, will be suppressed by the incorporation of the unnatural amino acid into the peptide chain (177).

LRET sample preparation

HEK293T cells are transiently transfected according to manufacture's protocol and maintained in DMEM. The transfected cells are collected and washed three times in extracellular buffer containing 160 mM NaCl, 1.8 mM $MgCl_2$, 1 mM $CaCl_2$, 3 mM KCl, 10 mM glucose, and 10 mM HEPES (pH 7.4). The washed HEK cells are then labeled with 400 nM donor and 100 nM acceptor fluorophores in 3 ml extracellular buffer, rotating at room temperature in the dark for 1 hr. The donor fluorophore typically used is terbium chelate (Invitrogen), and the acceptor fluorophore used is fluorescein maleimide (Thermo Fisher Scientific), for cysteine mutants. After labeling, cells are washed and resuspended in 2 ml extracellular buffer and are ready for use in LRET measurements.

Data collection LRET

A cuvette-based system consisting of a fluorescence lifetime instrument (EasyLife L;Hoiba) and analysis software (Fluorescan 5.5; Optical building blocks) is needed for

LRET measurements. Samples should be excited at 337 nm when using terbium chelate. Emission is detected at 545 nm for donor-only samples, at 515 nm for fluorescein-labeled samples. LRET measurements should be taken in triplicate for a given condition followed by scans after Factor Xa protease cleavage to quantitate the samples' background signals without the labeled receptors' contribution to the signal.

Data analysis LRET

Fluorescent decay plots obtained for given conditions and the background for that condition should be plotted in graphing software like Origin (OriginLab) and averaged, and then the background can be subtracted from the full signal. Following background subtraction, the resulting decay plots are fit to exponential decay functions thereby quantitating the decay lifetime of the acceptor fluorophore. Error in the distance estimates is calculated by propagating the errors in the donor and acceptor lifetimes using the Error Propagation Calculator developed by Thomas Huber in the Physics Department of Gustavus Adolphus College. Lifetimes should also be quantitated for samples labeled with only the donor (t_D) and samples labeled with both donor and acceptor (t_{DA}), to be used to calculate the distance between the fluorophores using the Forster equation:

$$\boldsymbol{R} = \boldsymbol{R_0}\left(\frac{\tau_{DA}}{\tau_D - \tau_{DA}}\right)^{1/6}$$

Eq. 3

where *R* is the distance between donor and acceptor fluorophore, R_0 is the distance yielding half-maximal energy transfer for a given fluorophore pair (45 Å for terbium-fluorescein), t_D is the measured lifetime of the donor when bound to the protein and without acceptor fluorophore present, and t_{DA} is the lifetime of the donor fluorophore when bound to the protein and transferring energy to the acceptor fluorophore, which can be measured as the lifetime of the sensitized emission of the acceptor. Final lifetime values for given conditions are obtained by averaging the background-subtracted lifetime values per day.

smFRET sample preparation

HEK293T cells should be transiently transfected, 10 μg per 10 cm plate for JetPrime reagent. One day post-transfection, cells from two 10-cm dishes are harvested and washed with extracellular buffer and labeled for 1 h at room temperature with 400 nM of donor fluorophore Alexa 555 maleimide (ThermoFisher) and 400 nM of acceptor fluorophore Alexa 647 maleimide (ThermoFisher) in 3 mL extracellular buffer. This concentration of fluorophore was determined to be optimal for single donor and single acceptor labeling. After washing, the labeled cells are then solubilized for 1 h at 4 °C in solubilization buffer (SB) consisting of phosphate-buffered saline, 1% lauryl maltose neopentyl glycol (Anatrace), 2 mM cholesteryl hydrogen succinate (MP Biomedicals), and ¼ protease inhibitor tablet (Pierce). The unsolubilized debris is then spun down for 1 h at 100,000 × g at 4°C, and the supernatant is used as the smFRET sample. Samples are then diluted 1:2 in cold SB before application.

Data collection smFRET

A confocal microscope is used for data collection. An example confocal system that is used for such smFRET experiments is the PicoQuant MicroTime 200 Fluorescence Lifetime Microscope. Scan a 20 μm x 20 μm area of the slide to identify molecules for imaging, then record the fluorescence intensity of each molecule until the donor and acceptor fluorophores undergo photobleaching. Example traces showing anticorrelation between the donor and acceptor are shown in **Figure 5**.

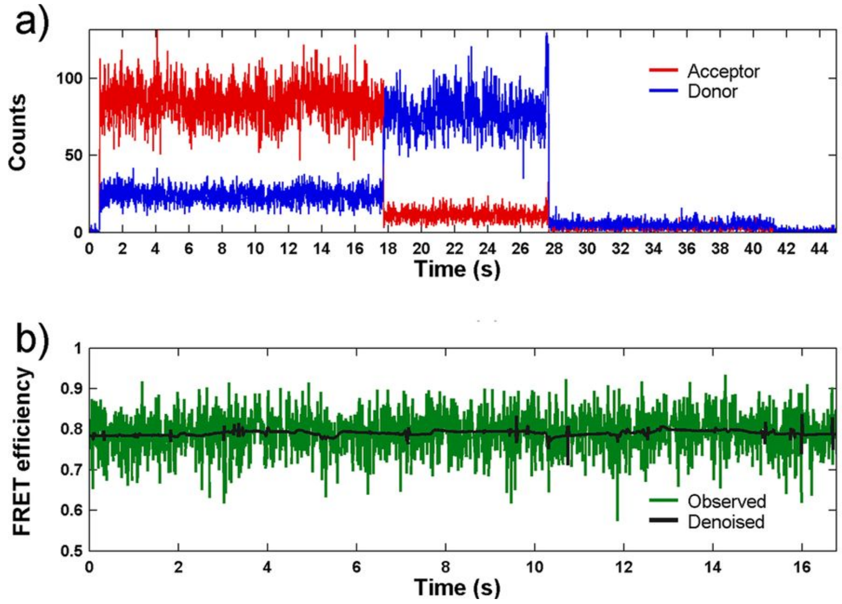

Figure 5. Representative smFRET fluorescence and efficiency traces.

(a) A representative smFRET trace measured from an agonist binding domain of AMPA receptor showing raw trajectories of the donor (blue) and acceptor (red) photons as a function of time. (b) The resulting calculated FRET trajectory (green) and its denoised counterpart (black). This research was originally published in the Journal of Biological Chemistry (157) © the American Society for Biochemistry and Molecular Biology.

To ensure that the fluorescence is from the receptor tagged at the site of interest, one will need to perform control experiments with no protein, protein with a single labeled site, and protein with two labeled sites as shown in **Figure 6**.

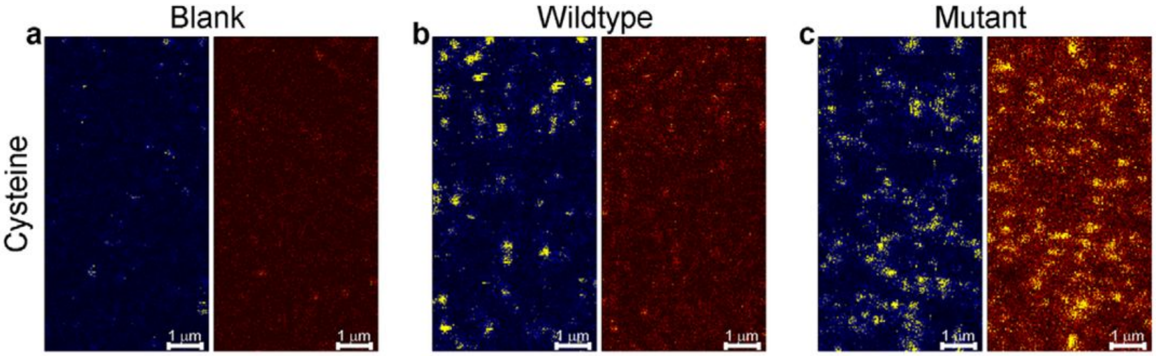

Figure 6. smFRET slide imaging showing the specificity of labeling strategies. smFRET slide imaging showing the specificity of the labeling strategy. Blue pane corresponds to donor channel, and brown pane is FRET channel (acceptor frequency emission with donor frequency excitation). As seen in (a) there is no labeling when protein is not applied to the slide. In (b), the appearance of donor signal is seen when protein with single cysteine labeled with fluorophores is applied to the slide. In (c), the appearance of FRET is seen when protein with two cysteine labeling sites labeled with fluorophores is applied to the slide. This research was originally published in the Journal of Biological Chemistry (178) © the American Society for Biochemistry and Molecular Biology.

Data analysis smFRET

For data analysis, the donor and acceptor data must be exported as ASCII files. Then, corrected FRET efficiencies (E_A) can be calculated according to equations 4 and 5:

$$\boldsymbol{E_A = (1 + \gamma \frac{I_D}{I_A})^{-1}}$$

Eq. 4

$$\boldsymbol{\gamma = \frac{\eta_A \Phi_A}{\eta_D \Phi_D}}$$

Eq. 5

where I_D is the intensity of donor fluorescence, I_A is the intensity of acceptor fluorescence, γ is a correction factor accounting for the efficiencies of the detectors used and for the quantum yield of the fluorophores, η is the efficiency of a given detector, and Φ is the quantum yield of a given fluorophore. Once corrected FRET efficiencies have been calculated, plot the histograms depicting the distribution of various FRET efficiencies and analyze those histograms using any graph software.

To identify states in the single molecule trajectory, the Hidden Markov Modeling (HaMMy) analysis (179) or the State Transition and State Identification (STaSI) analysis can be used (180).

Conclusions

With the incredible advances made in cryo-EM electron detector technology in the past 10 years, there is no question that the number and quality of cryo-EM based molecular structures will continue to grow. These models provide the foundation for our understanding of the molecular world; however, limitations in the conclusions that can be made concerning the dynamics involved in complex molecular functions make it critical that experiments capable of characterizing dynamics be executed in parallel. Through the use of MD simulations, molecular models can be integrated with structural dynamic experiments and provide a full picture of underlying biophysical mechanisms.

Chapter 6: FRET Studies of the GluK2 Homomeric Receptor

This chapter is based upon research originally published in *Scientific Reports*. Litwin, D. B., E. Carrillo, S. A. Shaikh, V. Berka, and V. Jayaraman. The structural arrangement at intersubunit interfaces in homomeric kainate receptors. *Scientific Reports*. 2019; 9(1):6969 © Springer Nature Publishing AG.

As discussed in chapter 4, several structures are now available for the different subtypes of the glutamate receptor (24, 26-32, 181-183). These structures show that the receptor is organized as a dimer of dimers and ligands bind to the clamshell-like agonist-binding domain (**Figure 7A**). The binding of agonist induces a cleft closure conformational change which, when propagated to the transmembrane segments, is thought to lead to activation. The activated state also exhibits a coupled dimer interface at the agonist-binding domain; decoupling of the dimer interface relieves the stress on the transmembrane segments induced by the cleft closure, resulting in desensitization (24, 26-29, 31, 32, 117, 181, 182).

However, most of these structures are for the AMPA and NMDA subtype of the glutamate receptors. Only three full-length kainate receptor structures are available, two in the antagonist-bound form (25, 29) and two in the agonist-bound form thought to be in the desensitized state (26, 29). These structures fall into two classes, the antagonist-bound structure with tight coupling at the interfaces at both the amino-terminal domain and agonist-binding domain, and the agonist-bound structure

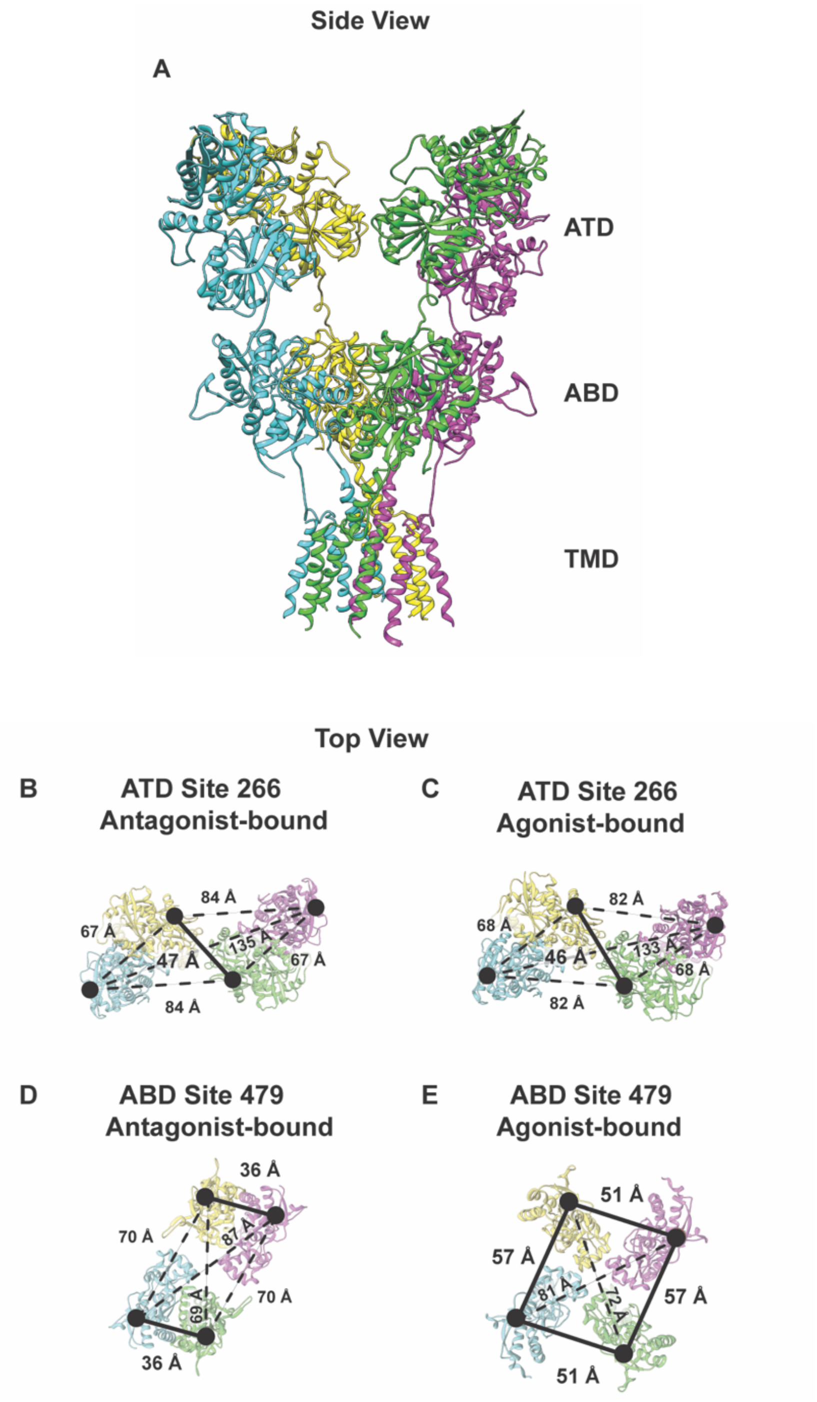

Figure 7. Structural arrangement of the GluK2 receptor and its FRET sites.

(A) Cryo-EM structure of GluK2 (PDB:5KUF) showing amino-terminal domains (ATD), agonist-binding domains (ABD), and transmembrane domains (TMD). (B and D) GluK2 ATD and ABD in antagonist-bound form (PDB:5KUH). (C and E) GluK2

ATD and ABD in agonist-bound form (PDB:5KUF). Labeling sites are shown as black spheres.

of the kainate receptor showing large decoupling at the agonist-binding domain with a near four-fold symmetry due to extreme decoupling between the dimers (**Figure 7A and E**). The closely related AMPA receptor structure exists in multiple conformations with varying degrees of decoupling at the amino-terminal and agonist-binding domain interfaces in the apo (27) and agonist-bound forms (24, 26-29, 31, 32, 181, 182). Thus, the question remains as to whether there is an inherent difference in the structure of kainate receptor relative to that of the AMPA receptor or is the perceived lack of heterogeneity due to the limited structural data currently available.

Kainate receptors are also unique among the glutamate receptor subtypes in exhibiting modulation by Na$^+$ ions. Functional studies have shown that kainate receptors require the presence of Na$^+$ and Cl$^-$ ions at physiologically relevant concentrations to mediate glutamate-gated channel opening and that substitution of the sodium ions with other monovalent cations, such as cesium ions, results in the inhibition of the receptor-mediated currents (110, 112-115). Structural and computational studies on the isolated agonist-binding domain, as well as indirect functional studies, indicate that the dimer interface is the binding site for the Na^+ (110, 112-115, 117, 142, 184). Given that the structural insight is based on the isolated agonist-binding domain, what is still needed to build on this foundation is insight into the modulation of the conformational and energy landscapes at this dimer interface by ions in the full-length receptor.

Recently, advances in fluorescence microscopy have made it possible to study the conformation-energy landscapes of a variety of molecules. When used in combination with previously published structural models, fluorescence resonance energy transfer (FRET) allows for the measurement of conformational heterogeneity and the energetic quantitation of dynamics within molecules (134, 155-158, 160, 170, 178). Herein we use this methodology to study the homomeric full-length kainate receptor at sites that are able to monitor proximity within the amino-terminal domain and within the agonist-binding domain dimer interfaces that are expected to show the conformational variability associated with desensitization and ion modulation. The smFRET studies presented herein provide the first look into the structural arrangement and dynamics associated with full-length kainate receptor antagonist-binding, activation, desensitization, and sodium modulation, specifically focusing on the interfaces which are thought to be critical in these processes. One limitation of this methodology is the millisecond (5 ms bins) resolution of the method, thus rapidly fluctuating conformations will appear as an average.

Results

Functional characterization of FRET constructs and selection of sites

The $GluK2_{EM}$ construct used previously in cyro-electron microscopy studies (26, 29) was modified for FRET experiments to allow for site-specific labeling by mutating the non-disulfide bonded cysteines C91, C199, C432 to serines (GluK2*). Site 266 and site 479 were chosen to introduce the donor and acceptor fluorophores based on two requirements (**Figure 7**). First, the sites reflected the large-scale conformational changes expected based on the currently available end state structures of the antagonist- and agonist-bound forms of the kainate receptor and closely related AMPA receptor. Second, the sites are arranged such that the distance being investigated (highlighted as darker line) has high FRET efficiency for the FRET donor-acceptor pair, all other distances are expected to have less than 15% FRET efficiency and if present should occur well separated from the distance of interest (134, 178, 185, 186). GluK2*-266C and GluK2*-479C constructs were characterized using electrophysiology and show kinetics similar to those of the wild type receptor (**Figure 8**). Additionally, these two mutants show a similar decrease in currents upon exchange of Cs^+ for Na^+ in the extracellular buffer (**Figure 8**).

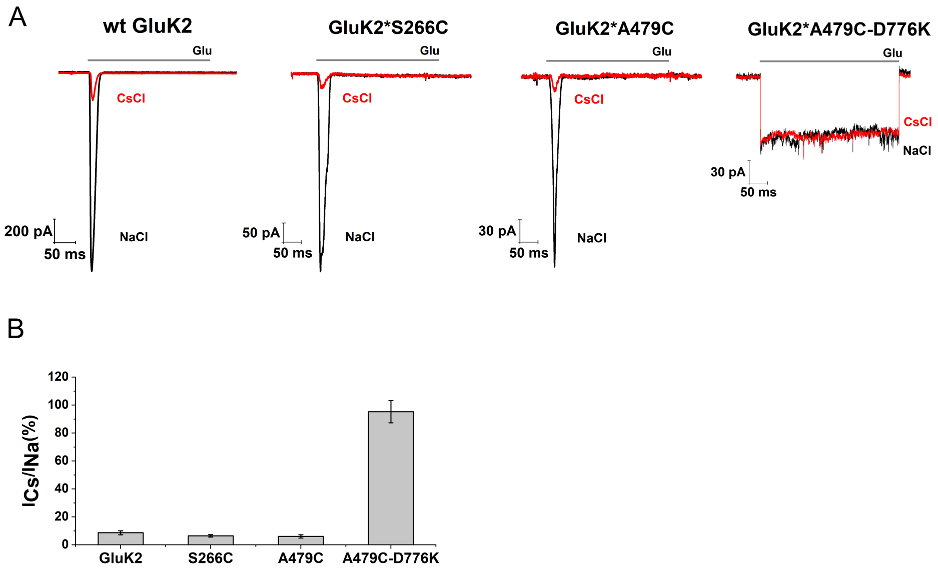

Figure 8. FRET construct characterization for homomeric studies.

(A) Representative whole-cell recordings for wild-type GluK2, and fluorophore-labeled GluK2*266C, GluK2*479C and GluK2*479C-D776K with extracellular 150mM NaCl (black traces) or 150mM CsCl (red traces) and in the presence or absence of 10mM glutamate. (B) Bar graph showing currents obtained using Cs$^+$ buffer normalized to currents obtained using Na$^+$ buffer.

Conformational changes at the amino-terminal domain

In order to compare measurements made with the receptor retained in a lipid bilayer with those obtained under detergent solubilized conditions using smFRET, LRET measurements were performed on construct GluK2*266C. The LRET fluorescent decay plots for construct GluK2*266 under apo conditions show a lifetime of 619 μs, which corresponds to a distance of 42 ± 0.47 Å. The LRET plots for construct GluK2*266 under glutamate-bound conditions show a lifetime of 569 μs, which corresponds to a distance of 41 ± 0.39 Å, **Figure 9**. These data show that there is no significant change in distance at this site between the apo and glutamate-bound conditions.

Denoised smFRET efficiency histograms for the GluK2*-266C receptor and representative smFRET traces are shown for the apo, antagonist and glutamate-bound states in **Figure 10A, B and C**, respectively. The denoised smFRET efficiency histogram was obtained using traces that exhibited single donor and single acceptor photobleaching, **Figure 20A**, thus ensuring that the efficiency corresponds to a single donor-acceptor distance. Additional representative smFRET traces are provided in **Figure 11**. The smFRET trajectories were analyzed using the statistical software suites STaSI (180) (**Figure 10 A, B and C**) and HAMMY(179) **Figure 20B**. STaSI determines the number of states within a data set using a t-test to identify step transitions and a minimum description length algorithm to determine the optimal number of states. HAMMY creates a model of the step transitions and states that best describe a data set using hidden Markov modeling. A comparison of different software by Sigel and coworkers showed that STaSI is more accurate in predicting number of states and

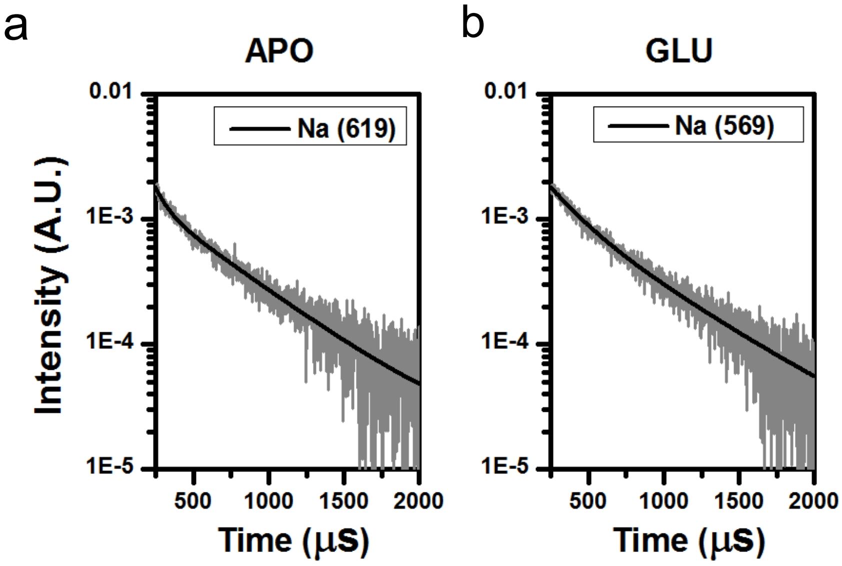

Figure 9. LRET data for the N-terminal domain construct GluK2*266C.

Acceptor fluorophore decay plots for GluK2*S266C in the presence of 150 mM NaCl under (a) apo conditons and (b) glutamate-bound conditions. Measurements were made using terbium chelate (donor) and fluorescein (acceptor).

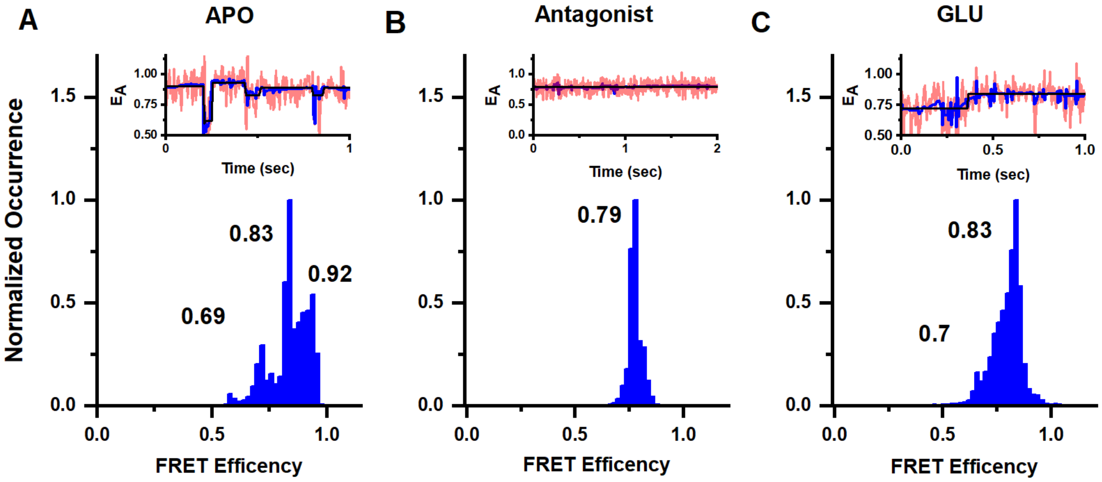

Figure 10. smFRET efficiency histograms for construct GluK2*266C.

Conformational landscape of the dimer-dimer interface at the amino-terminal domain at site 266 in full length homomeric GluK2 receptors. Representative smFRET traces and FRET histograms showing fractional occurrence as a function of FRET efficiency in (A) the apo state (data from 47 molecules), (B) presence of 1mM UBP310 (data from 29 molecules) and (C) presence of 1mM glutamate (data from 50 molecules). Traces show observed signal in pink, denoised signal in blue, and state transitions in black.

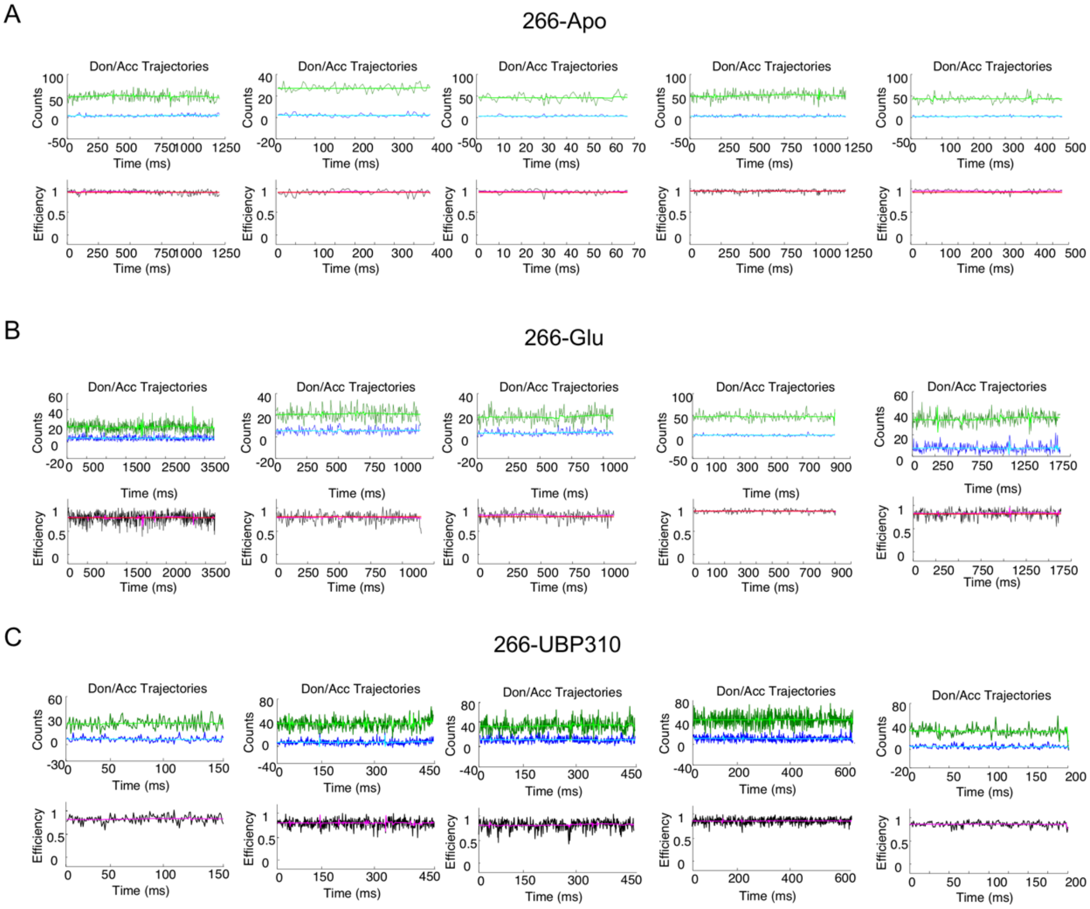

Figure 11. Representative FRET efficiency traces for constuct GluK2*266C. Representative FRET efficiency traces showing the observed acceptor (green), donor (blue) and FRET efficiency (black) in the FRET region for site 266 in the (A) apo state (B) glutamate-bound state, and (C) UBP310 bound state. The wavelet based denoised data is shown in neon green, cyan and magenta overlaid on the observed data.

state efficiencies (187). However, STaSI uses denoised data while HAMMY is performed on observed data, hence we have used both to ensure that denoising is accurate.

Under apo conditions three FRET efficiency peaks are observed at 0.69, 0.83 and 0.92 corresponding to distances of 45 Å, 39 Å, and 34 Å. The smFRET histogram for the antagonist UBP-310, on the other hand, shows a single peak at 0.79 FRET efficiency indicating a single conformation, which corresponds to a distance of 41 Å. The distances of 45 Å in the apo and 41 Å in antagonist-bound state are similar to the distances of 45 Å (PDB:5WEN(31), 5LIB(183), 3KG2(24), 4U4G(28)) and 42 Å (PDB:4U2P(27)) at equivalent sites seen in the antagonist and apo state structures of closely related AMPA receptors. In the glutamate-bound state two FRET efficiency peaks are observed at 0.7 and 0.83 that correspond to distances 44 Å and 39 Å . These distances are similar to the 46 Å (PDB:5VHZ(32), 4U4F(28)) and 40 Å (PDB:4U2Q(27)) seen in the glutamate-bound structures of closely related AMPA structures, and 46 Å in the agonist-bound structure of kainate receptors (PDB:4UQQ(26)). The spread of states observed in the amino-terminal domain in the glutamate-bound state of kainate receptors does not show large decoupling as seen in Class II and Class III agonist-bound structures of AMPA receptors (15).

Conformational changes at the agonist-binding domain

To characterize the conformational and energy landscape at the dimer interface of the agonist-binding domain, smFRET experiments were conducted using GluK2*-479C. smFRET histograms for mutant GluK2*-479C in the apo, antagonist, and glutamate-bound states in the presence of Na^+ are shown in **Figure 12A-C**. Additional representative smFRET traces are provided in **Figure 13** and corresponding

HAMMY fits for the data are show in **Figure 20C**. The apo state in the presence of Na^+ has a single peak in histogram showing a single state with a FRET efficiency of 0.89, corresponding to a distance of 36 Å. The antagonist-bound state also shows a single peak but with a more narrow half width indicating a more rigid protein. The FRET efficiency is also higher 0.95 corresponding to a distance of 31 Å. These data are representative of a coupled agonist-binding domain dimer interface and similar to the 33 Å seen in the antagonist-bound structure of kainate receptor (PDB:5KUH(29)).

The smFRET histogram in the presence of glutamate and Na^+, on the other hand, shows five FRET efficiencies, (**Figure 12C**), corresponding to distances of 55 Å, 49 Å, 44 Å, 39 Å and 33 Å. These distances are similar the two distances of 57 Å and 51 Å between the dimers in current kainate receptor models (PDB:4UQQ(26), 5KUF(29)). However, a large fraction of the receptors show a less decoupled interface and these shorter distances have been observed in AMPA receptors, with structures showing a distance of 46 Å (PDB:5VHZ(32), 5VOV(30)) and a distance of 39 Å (PDB:4U2Q(27), 4U4F(28)) at the equivalent sites.

smFRET was next used to characterize the active state structural dynamics of the kainate receptor using a D776K mutant, which stabilizes the receptor in the open state (144) (**Figure 12D**). Additional representative smFRET traces are provided in

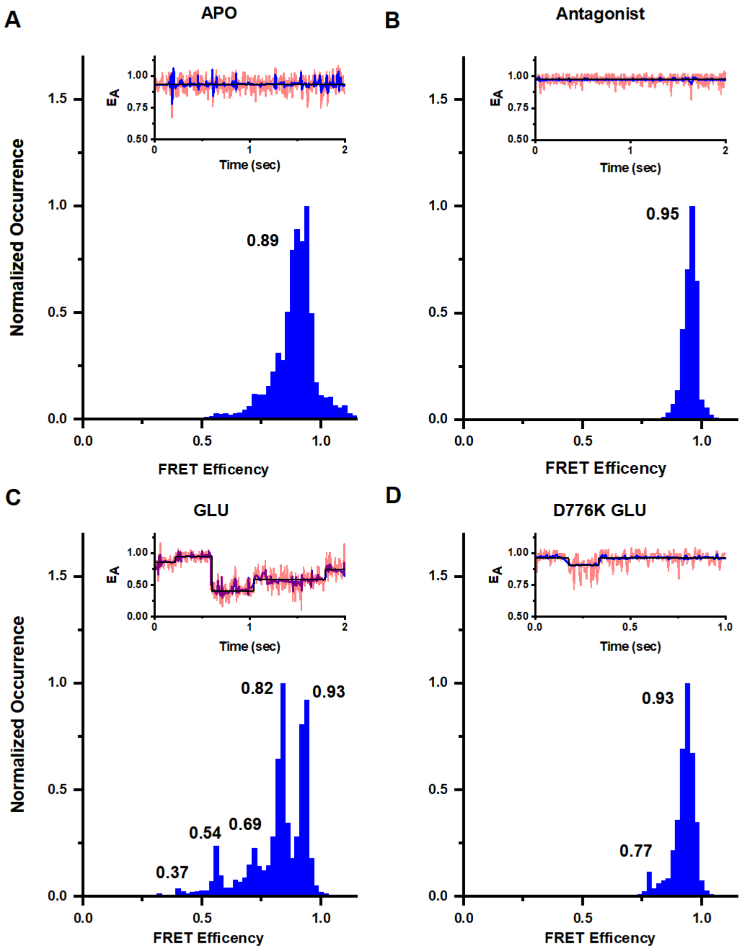

Figure 12. smFRET efficiency histograms for construct GluK2*479C.

Conformational landscape at dimer interface at the agonist-binding domain at site 479 in full length homomeric GluK2 receptors. Representative smFRET traces and FRET histograms showing fractional occurrence as a function of FRET efficiency in presence of 150 mM NaCl in the (A) apo state (data from 57 molecules), (B) presence of 1mM UBP310 (data from 28 molecules), and C) presence of 1 mM glutamate (data from 66 molecules), and (D) D776K mutant in the presence of 1mM glutamate (data from 47 molecules).

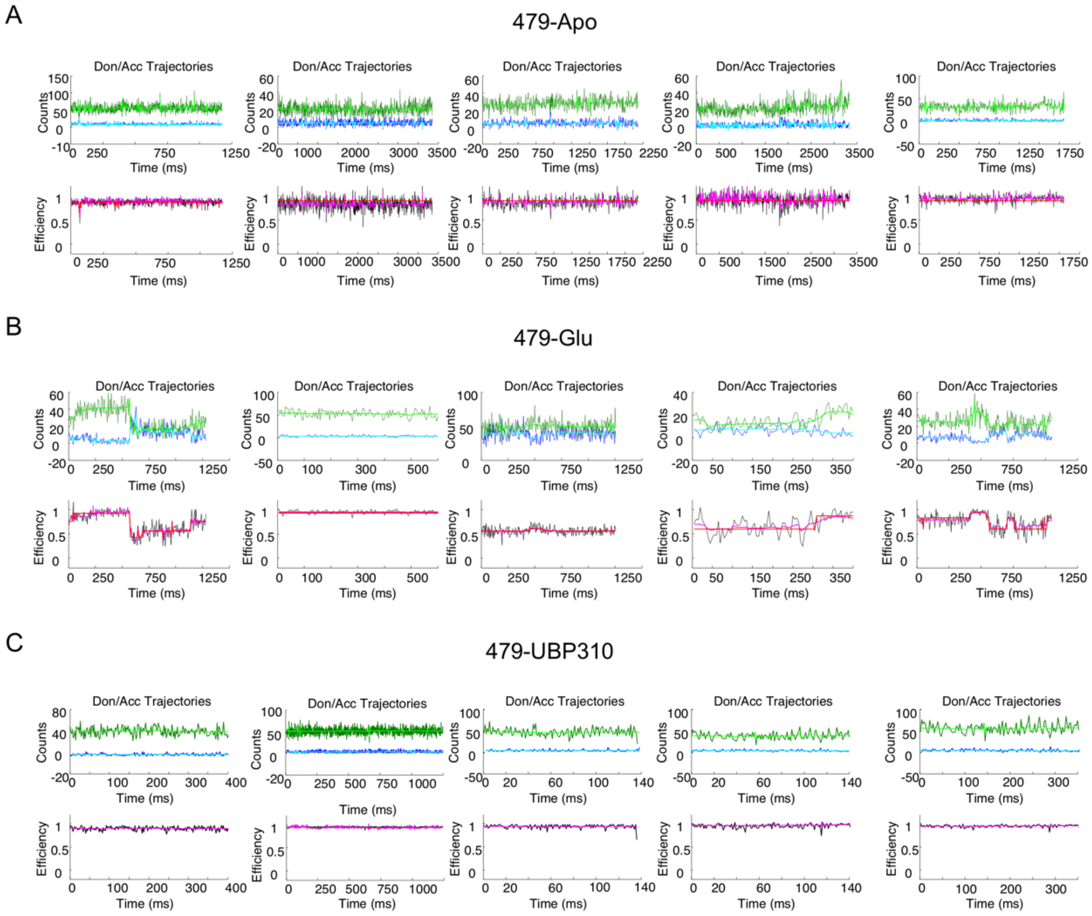

Figure 13. Representative FRET efficiency traces for constuct GluK2*479C. Representative FRET efficiency traces showing the observed acceptor (green), donor (blue) and FRET efficiency (black) in the FRET region for site 479 in the (A) apo state (B) glutamate-bound state, and (C) UBP310 bound state. The wavelet based denoised data is shown in neon green, cyan and magenta overlaid on the observed data.

Figure 14. The smFRET data show that for this open-state stabilized receptor, the primary state has a FRET efficiency of 0.93, which corresponds to a distance of 33 Å. While both the apo state and the D776K glutamate-bound state have primarily one main conformation, the striking difference between the two is the half width of these states. The half width is narrower in the D776K glutamate-bound state relative to that in the apo state of the receptor, indicating that the protein is more rigid in the D776K glutamate-bound state relative to the apo state of the receptor.

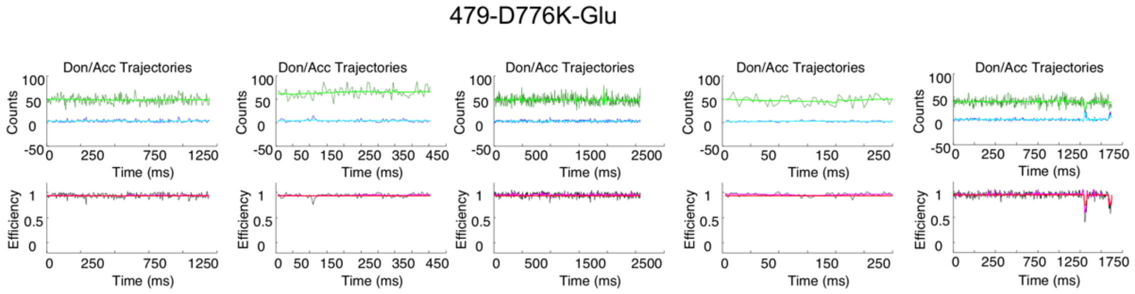

Figure 14. Representative FRET efficiency traces for constuct GluK2*479C-D776K.

Representative FRET efficiency traces showing the observed acceptor (green), donor (blue) and FRET efficiency (black) in the FRET region for site 479 in the D776K background for glutamate bound state in NaCl. The wavelet based denoised data is shown in neon green, cyan and magenta overlaid on the observed data.

Conformational modulation by ions

To study the structural effects of ion modulation, smFRET and LRET measurements were performed with the kainate receptor in the presence of Cs^+ (replacing the Na^+ ions). Cs^+ was chosen as there are extensive electrophysiological studies performed under these conditions showing large decreases in currents (110, 112-114). Thus, direct correlations can be made between the smFRET data and this large body of functional studies. Changes are observed between the Na^+ and Cs^+ conditions in the apo state of the receptor.

When Na^+ is replaced with Cs^+ a LRET lifetime of 560 μs is found for the apo state at site 266, which corresponds to a distance of 41 ± 0.22 Å, **Figure 15**. For the glutamate-bound state a lifetime of 629 μs is found, which corresponds to a distance of 42 ± 0.17 Å. These data show that similar to Na^+ containing conditions, there are no significant changes in distance at this site between that apo and glutamate-bound conditions. The lifetimes obtained under these conditions correspond to distances of 41 Å (569 and 560 μs) and 42 Å (619 and 629 μs). These distances fit well with the distances obtained for this site using smFRET under conditions contain either Na^+ or Cs^+.

The smFRET denoised histograms show three efficiency peaks in the presence of Cs^+ (**Figure 16A**) for site 479, corresponding to distances of 48 Å, 41 Å, and 34 Å, respectively. Additional representative smFRET traces are provided in **Figure 17**. The Cs^+ conditions are in contrast to the apo state of the receptor in the presence of Na^+, where the receptor exists primarily in the high FRET more coupled state. The smFRET denoised traces for the glutamate-bound state in the presence of Cs^+ (**Figure 16B**)

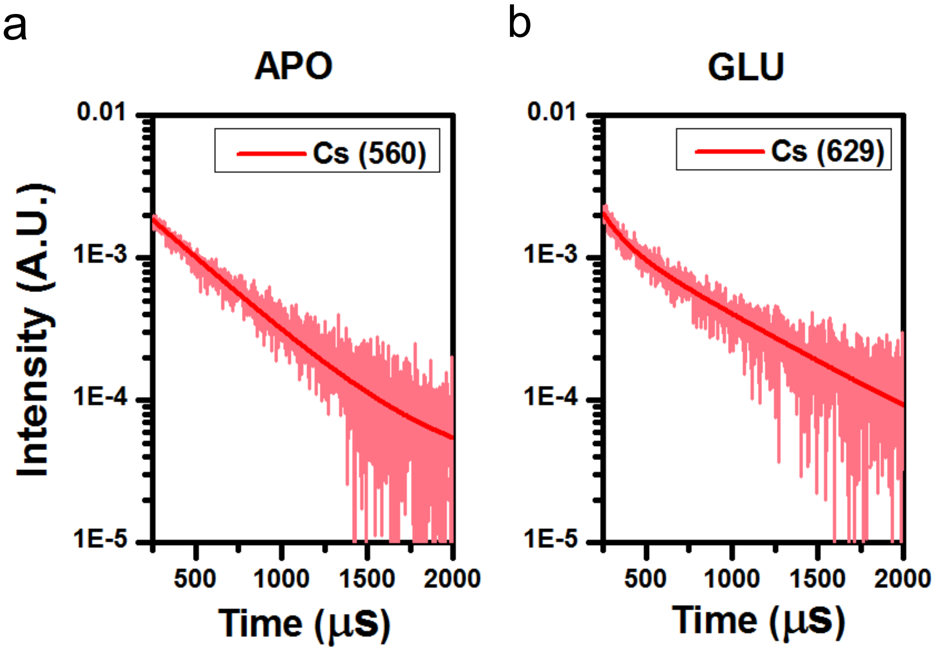

Figure 15. LRET data for the amino-terminal domain construct GluK2*S266C. Acceptor fluorophore decay plots for GluK2*S266C in the presence of 150 mM CsCl under (a) apo conditons and (b) glutamate-bound conditions. Measurements were made using terbium chelate (donor) and fluorescein (acceptor).

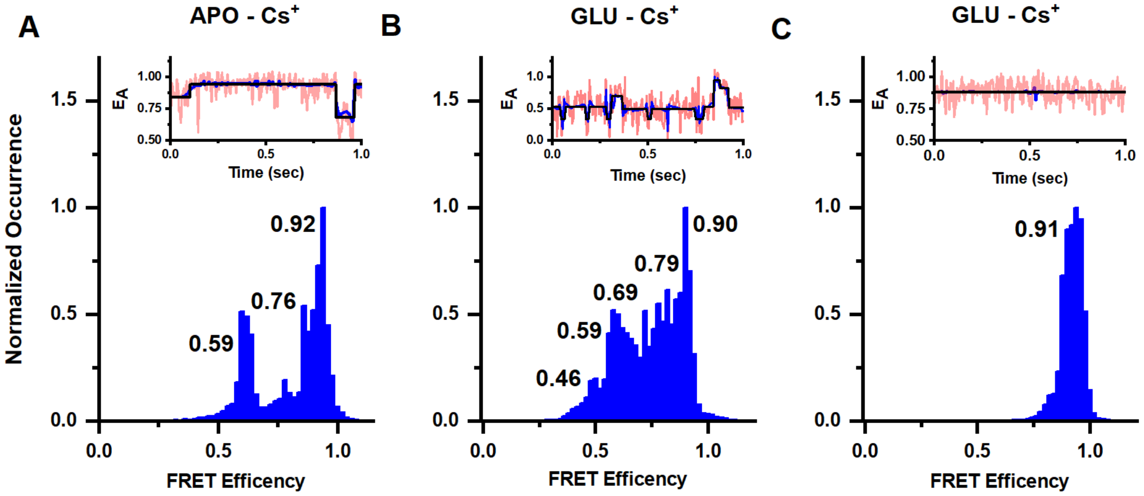

Figure 16. smFRET efficiency histograms for construct GluK2*479C and GluK2*479C-D776K in the presence of CsCl.

Conformational landscape of the dimer interface at the agonist-binding domain at site 479 in full length homomeric GluK2 receptors. Representative smFRET traces and FRET histograms showing fractional occurrence as a function of FRET efficiency in presence of 150 mM CsCl in the (A) apo state (data from 55 molecules), (B) presence of 1 mM glutamate (data from 52 molecules), and (C) D776K mutant in the presence of 1mM glutamate (data from 55 molecules).

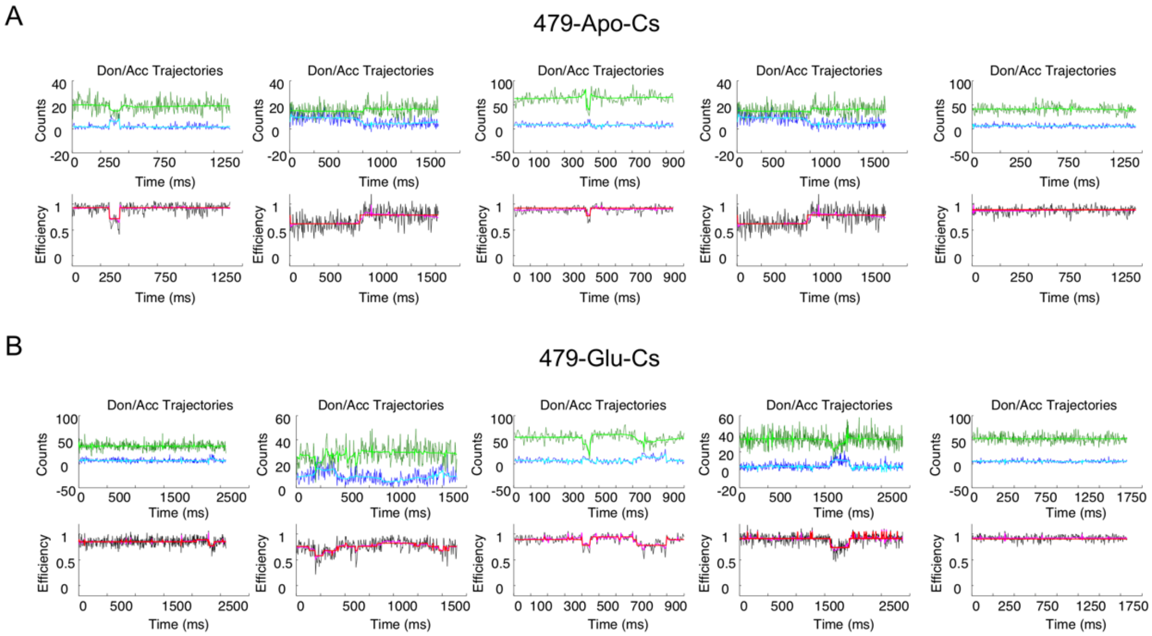

Figure 17. Representative FRET efficiency traces for constuct GluK2*479C in the presence of CsCl.

Representative FRET efficiency traces showing the observed acceptor (green), donor (blue) and FRET efficiency (black) in the FRET region for site 479 in the (A) apo and (B) glutamate-bound stat in the presence of 150 mM CsCl. The wavelet based denoised data is shown in neon green, cyan and magenta overlaid on the observed data. Representative FRET efficiency traces showing the FRET regions for site 479.

showed FRET efficiencies corresponding to five distances of 51 Å, 48 Å, 44 Å, 40 Å, and 35 Å. These distances in Cs^+ are similar to the distances of 55 Å, 49 Å, 44 Å, 39 Å and 33 Å observed in Na^+. However, the occupancies of these states are significantly different, with higher occupancy of lower FRET states in Cs^+ relative to Na^+. These results indicate that while the receptor occupies similar conformational states in both Cs^+ and Na^+, the more decoupled states have higher occupancy in the presence of Cs^+.

The D667K mutant on the other hand did not show any significant shift in the states between Na^+ (**Figure 12D**) and Cs^+ (**Figure 16C**), additional representative traces shown in **Figure 18**. Given that the activated state requires coupling between the dimers, the larger fraction of the receptors in the low FRET decoupled states in the apo state of the receptor in the presence of Cs^+ would contribute to the decrease in activation observed in the presence of Cs^+.

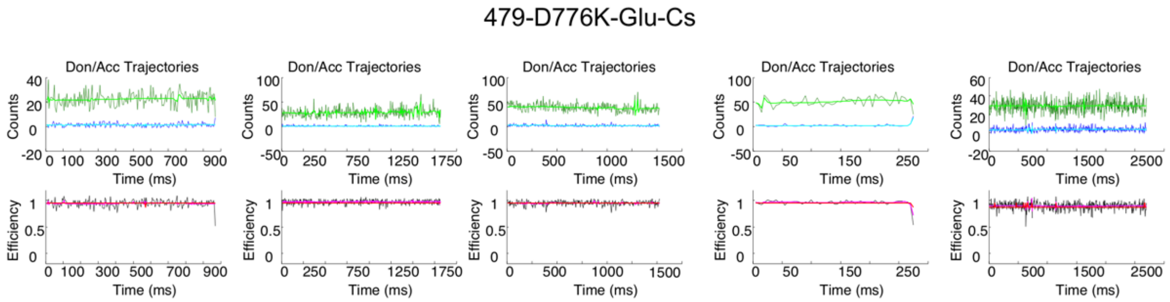

Figure 18. Representative FRET efficiency traces for constuct GluK2*479C-D776K in the presence of CsCl.

Representative FRET efficiency traces showing the observed acceptor (green), donor (blue) and FRET efficiency (black) in the FRET region for site 479 in the D776K background for glutamate bound state in CsCl. The wavelet based denoised data is shown in neon green, cyan and magenta overlaid on the observed data.

State transitions and energy landscape

In addition to providing the state occupancy, the smFRET trajectories allow for the direct observation of transitions between different states, specifically in the desensitized and Cs^+ conditions, as exemplified by the representative traces in **Figures 12 and 16**. Based on these data, we have obtained transition maps showing the relative number of transitions between states (**Figure 19**). The data show that within the agonist-binding domain, transitions primarily occur between states of nearest FRET efficiency, whereas transitions between non-adjacent states are less common. The probability of observing these non-adjacent state transitions is higher in the presence of Cs^+ under desensitizing conditions, which suggests a lower energy barrier for the transitions. These data are consistent with the energy maps and show that in the presence of both glutamate and Na^+, the lowest energy barrier of transition is between the high-FRET states with efficiencies of 0.93 and 0.82. However, in the presence of both glutamate and Cs^+, the activation energy barriers are similar across all states. These data indicate that with Na^+ present the receptor is more stable in the coupled state and requires more energy to transition into states with increasing distance, and that in the presence of Cs^+ the receptor is able to move across states with relatively low energy barriers.

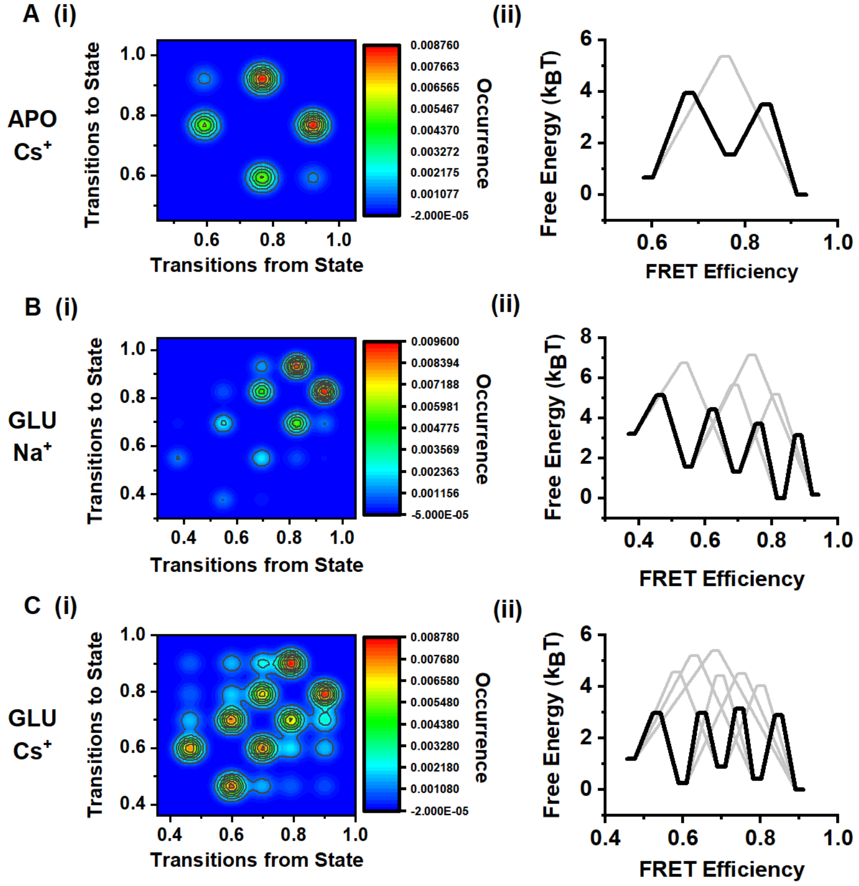

Figure 19. Transition maps and free energy diagrams based on the smFRET data at site 479.

Transition maps showing transitions from a given FRET efficiency to a given FRET efficiency (i) and free energy associated with the transitions (ii) in (A) 150 mM CsCl, (B) 150 mM NaCl and 1mM glutamate, and (C) 150 mM CsCl and 1mM glutamate.

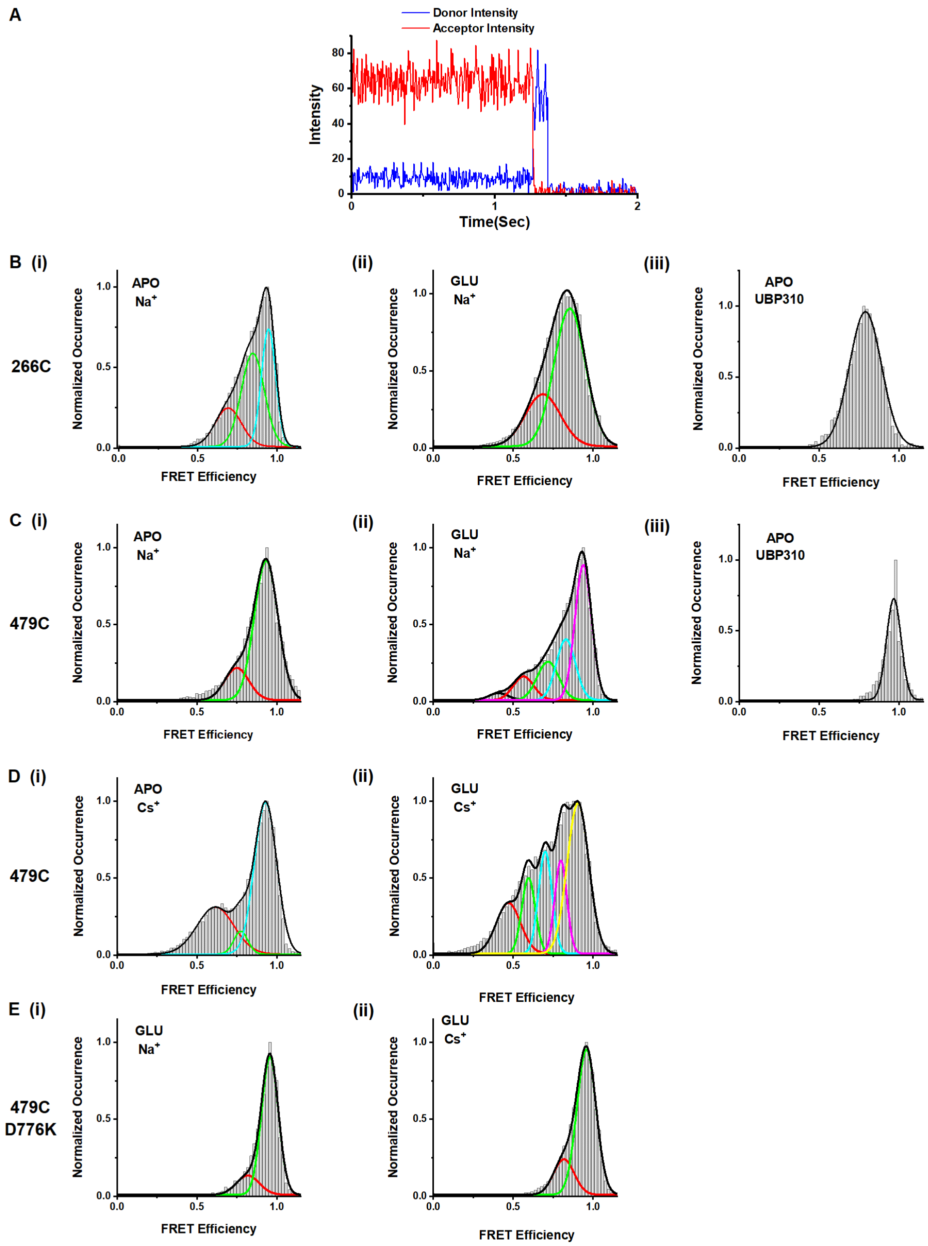

Figure 20. Representative trace and Gaussian fit histograms for homomeric studies.

(A) Representative traces showing single photobleaching step for donor and acceptor and anticorrelation showing that the donor and acceptor are from FRET pairs. Observed histograms with data being fit using Gaussians based on HAMMY analysis for (B) GluK2*S266C (i) in apo conditions, (ii) in the presence of 1mM glutamate and

(iii) in the presence of 1 mM UBP310. (C) GluK2*479C with 160 mM NaCl and in apo conditions (i), (ii) in the presence of 1mM glutamate and (iii) in 150 mM NaCl with 1mM UBP310. (D) GluK2*479C with 150 mM CsCl and in the absence (i) and presence (ii) of 1mM glutamate.(E) GluK2*479C-D776K with (i) 150 mM NaCl and 1mM glutamate and (ii) 150 mM CsCl and 1mM glutamate.

Discussion

There are several X-ray crystallographic structures of isolated domains for all subtypes of the ionotropic glutamate receptor. Studies of the full-length receptor, however, have been primarily focused on the AMPA and NMDA subtypes (24, 26, 27, 29, 32, 181, 182), with only an antagonist- and agonist-bound structure of the full-length kainate receptor. The structures (24, 26-29, 31, 32, 181, 182), spectroscopic investigations (157, 158, 160, 170, 178, 188, 189), and molecular dynamic simulations of AMPA and NMDA receptors (190-192) show that the protein occupies multiple conformations under any given condition and such diversity in conformation is consistent with the diversity of states seen in single channel recordings of these receptors. More importantly, these studies suggest that the receptor function is dictated to a large extent by conformational selection. However, this structural heterogeneity has not been shown for the kainate receptors. Herein we have used a combination of LRET and smFRET measurements to resolve the conformational landscape of the full-length kainate receptor under physiologically-relevant conditions in the antagonist-bound, apo, active, and desensitized states and additionally have identified the changes in kainate receptor dynamics induced by Na^+ modulation.

The resting state

Detailed structural models of the apo state of the kainate receptor have been particularly elusive; the only structural information with respect to the resting state has been derived from the structure of the antagonist-bound form of the receptor. The smFRET data show that under apo conditions in the presence of Na^+, the agonist-binding domain exists primarily in one conformation, with a distance consistent with a coupled dimer interface, but structural heterogeneity is observed at the amino-terminal domain with a small distance range. This is similar to what is seen in the AMPA receptors (31). Additionally, the distances corresponding to the FRET efficiencies obtained match well between LRET and smFRET measurements. In the presence of Cs^+ ions, on the other hand, the dimer interface exhibits both coupled and decoupled conformations. Because the active state requires the agonist-binding domain interface to be coupled, this decoupled dimer interface would require more energy to be converted to the active state and can account for the lower receptor activation observed in the presence of Cs^+.

The antagonist-bound state

The smFRET histograms for the antagonist-bound state at both the amino-terminal domain and agonist-binding domain show single states that are similar to the most probable state seen in the resting apo state. However, the antagonist-bound state is clearly more rigid at these interfaces, exhibiting a smaller half width even in this single state.

The active state

The smFRET data on the D776K mutant, which stabilizes the receptor in the open, activated state, show that the agonist-binding domain dimers remain primarily coupled in the active state and that substituting Cs^+ for Na^+ has no effect. These data are consistent with the structure and molecular dynamics simulations of the D776K mutant that show the introduced lysine can occupy the Na^+ binding site (117), eliminating the requirement for Na^+ to activate. Furthermore, these data are consistent with the electrophysiological measurements which show a similar extent of activation under both Na^+ and Cs^+ conditions (117). The smFRET data showing a tightly coupled active state in the D667K mutant with a much smaller full width at half maximum relative to the apo state, indicates that this structural rigidity at the interface allows for the channel to be constitutively active with high probability of opening as seen in single channel recordings (117).

The desensitized state

Current structures of kainate and AMPA receptors under desensitizing conditions show significant differences between the two closely-related subtypes. At the amino-terminal domain, the kainate receptor showed minimal decoupling, while the AMPA receptor showed varying degrees of decoupling. At the agonist-binding domain the kainate receptors showed complete decoupling with the receptor transitioning into a near four fold symmetry, while the AMPA receptor showed smaller decoupling (24, 27, 28, 32, 182). However, cysteine crosslinking studies by Soblovesky and coworkers question the large decoupling seen in the AMPA receptors (33), as desensitization is observed even in the cross-linked non-decoupled receptor.

The smFRET measurements under desensitizing conditions showed heterogeneity at the dimer-dimer interface at the amino-terminal domain and minimal decoupling. This would be similar to the non-decoupled states seen with crosslinking (33). Additionally, the smFRET data show that the large decoupled agonist-binding domain structure seen in the cryo-EM structure accounts for a small fraction of the receptors in the desensitized state. However, a large fraction of the receptors show no or slight decoupling similar to what has been observed in the AMPA receptors. Based on the smFRET measurements it can be concluded that kainate and AMPA receptors exhibit largely similar trends in terms of structural heterogeneity in the desensitized state with much smaller differences than was previously thought.

SmFRET measurements characterizing the proximity of the agonist-binding domain dimers in the presence of Cs^+ show that the more decoupled states are favored, and the energy barrier is lowered for transitions to more decoupled states. This decrease in energy barrier is consistent with MD simulations that showed a decrease in the work required to decouple the dimer interface in the absence of Na^+ ions (117, 142). The fact that the conformational states of the agonist-binding domain are the same in both Na^+ and Cs^+ conditions suggest a conformational selection mechanism. The occupancy of similar states is consistent with the fact that the X-ray structures of the isolated agonist binding domain are similar under both Na^+ and Cs^+ conditions. The smFRET data adds to this prior knowledge by showing that the occupancy of these states are shifted.

Importantly, similar distances are found between sites 266 when measured using both LRET and smFRET. The comparison of these data indicate that the receptor is in a similar conformational arrangement in either lipid bilayer or detergent solubilized and that a direct comparison can be made between the two techniques. Unfortunately, LRET measurements were limited to the ATD due to functional limitations of the receptor.

Conclusions

Using a combination of LRET and smFRET measurements we have characterized the conformation and energy landscapes of the kainate receptor in the apo, antagonist-bound, active, desensitized, and Na^+-modulated states. These data suggest a similar conformational heterogeneity as seen in the AMPA receptors. The desensitized and resting states of the receptor are energetically altered in the presence of Cs^+, which drives the protein into a decoupled dimer state which in turn leads to lower activation.

Chapter 7: FRET Studies of the GluK2/GluK5 Heteromeric Receptor

This chapter is based upon research originally published in *Biochimica et Biophysica Acta- Biomembranes*. Litwin, D. B., N. Paudyal, E. Carrillo, V. Berka, and V. Jayaraman. The structural arrangement and dynamics of the heteromeric GluK2/GluK5 kainate receptor as determined by smFRET. *Biochimica et Biophysica Acta- Biomembranes*. 2019; DOI: 10.1016/j.bbamem.2019.05.023 © Elsevier B.V.

As discussed in chapter 4, the majority of ionotropic glutamate receptor models available are of the AMPA and NMDA subtype with only three available for full-length homomeric GluK2 kainate receptors, one in the antagonist-bound form (25, 29) and two in the agonist-bound form exhibiting desensitized state (26, 29). The structural data available for the homomeric kainate receptor has laid a foundation for our understanding of the structural characteristics that give rise to the unique function of kainate receptors.

The heteromeric GluK2/GluK5 kainate receptor is known to be the most abundant kainate receptor expressed in the brain (193). Therefore, identifying the structural features that are unique to the GluK2/GluK5 heteromer is crucial to design therapeutically potential kainate receptor specific compounds. Yet, the only structural models currently available for the heteromeric kainate receptor are of the isolated amino-terminal domains (125). MD simulations on the homology model of isolated agonist-binding domain dimer show that the heteromeric receptor has more decoupled dimer interface relative to the homomeric receptors (184). Functionally the

GluK2/GluK5 heteromer has shown higher glutamate sensitivity (85, 194-196) and a faster rate of desensitization ($\tau_{\text{des GluK2/K5}}$ = ~3 ms) compared to the homomeric receptor ($\tau_{\text{des GluK2}}$ = 5.8 ms) in the presence of sodium ions (184). These differences in function leave no question that there are valuable structural characteristics of heteromeric kainate receptors left to be resolved. The only advances in our understanding of the structure of the GluK2/GluK5 heteromer show that they localize to the plasma membrane with a subunit stoichiometry of 2:2 and that the GluK2 amino-terminal domains likely mediate the amino-terminal domain dimer-dimer interface (124, 125).

FRET acts as a molecular ruler providing distances between the donor and acceptor fluorophores attached to specific sites of a molecule, and when used at the single molecule level allows for investigating the conformational landscape and energetics of functionally-significant dynamics within molecules (134, 155-158, 160, 170, 178). For the single molecule FRET (smFRET) measurements, membrane preparations of cells expressing the protein used with minimal purification, thus providing insight into the proteins in a near native conformation (134, 155-158, 160, 170, 178). Here, we have used smFRET to address the specific arrangement of the receptor, and to understand the conformational landscape of the heteromeric receptor, specifically the conformational landscape across the dimer-dimer interface at the amino-terminal domain, the dimer interface at the agonist-binding domain and at the transmembrane segments. These sites were chosen as they are known to play important roles in activation and desensitization in the homomeric kainate receptor and/or the closely related AMPA receptor (33, 143, 197-199). Additionally, the sites at the amino-terminal domain and agonist-binding domain are equivalent to those that we used to study the homomeric receptors (200), thus a direct comparison of differences between the conformational landscape of the heteromeric and homomeric receptors can be made and correlated to differences in function.

Results and discussion

For smFRET measurements we modified the GluK2 and GluK5 receptors to remove accessible cysteines as shown in **Figure 21** (modified constructs are referred to as GluK2* and GluK5*). Additionally, we have introduced a twin strep tag on the background of GluK5 constructs. Since, GluK5 subunits do not express as homomeric receptors (124, 151, 201-203), performing the *in situ* pull down using streptavidin on membrane preparations of HEK-293 cells co-expressing GluK2 and GluK5 subunits allows for the specific attachment of GluK2/GluK5 receptors and excludes the attachment of GluK2 homomeric receptors.

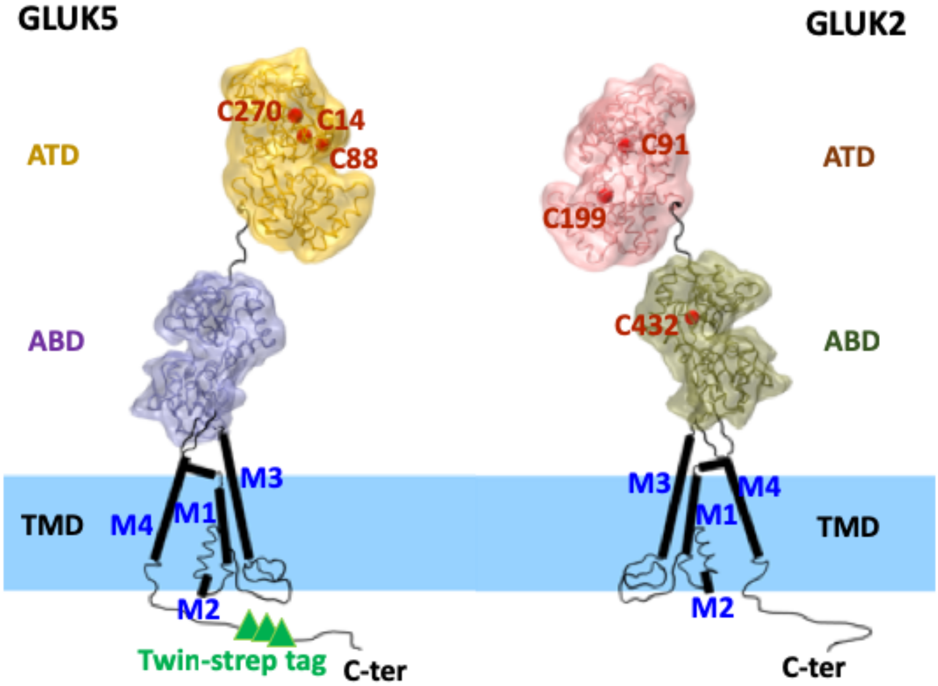

Figure 21. Structural arrangement of the GluK2/GluK5 heteromeric receptor. Extracellular amino-terminal domain (ATD) and agonist-binding domain (ABD) represented as bilobed structures in domain swapping configuration. Accessible cysteines modified to form cysless constructs for GluK5 and GluK2 subunits are shown as red spheres. Transmembrane domain (TMD) consisting of four helices M1, M2, M3 and M4, are represented as cylindrical structure inside the membrane. A twin-strep tag is attached to the C-terminus of GluK5 subunit shown in green.

Arrangement of GluK2 and GluK5 subunit with the kainate receptor.

Given that the kainate receptor subunits are arranged as dimer of dimers, the GluK2 and GluK5 subunits can be assembled in three possible configurations (**Figure 22**). To determine the configuration(s) that the receptor occupies using smFRET, we measured distances between sites 266 and 266 in the two GluK2 subunits, and equivalent sites 272 and 272 in the two GluK5 subunits, within the GluK2/GluK5 heteromeric receptors. These sites were chosen based on homology models of the GluK2/GluK5 receptors generated which show that the distances between these sites can be used to clearly differentiate between the possible configurations (**Figure 23 A-C**). The functionality of GluK2*-266/GluK5* and of GluK2*/GluK5*-272 subunits labeled with Alexa 555 and Alexa 647 fluorophores were established using whole cell current recordings (**Figure 24**).

Figure 22. Representation of the possible arrangments of the heteromeric amino-terminal domains.

Possible configurations for amino-terminal domains of GluK2 and GluK5 subunits in GluK2/GluK5 heterotetramer forming dimer of dimers.

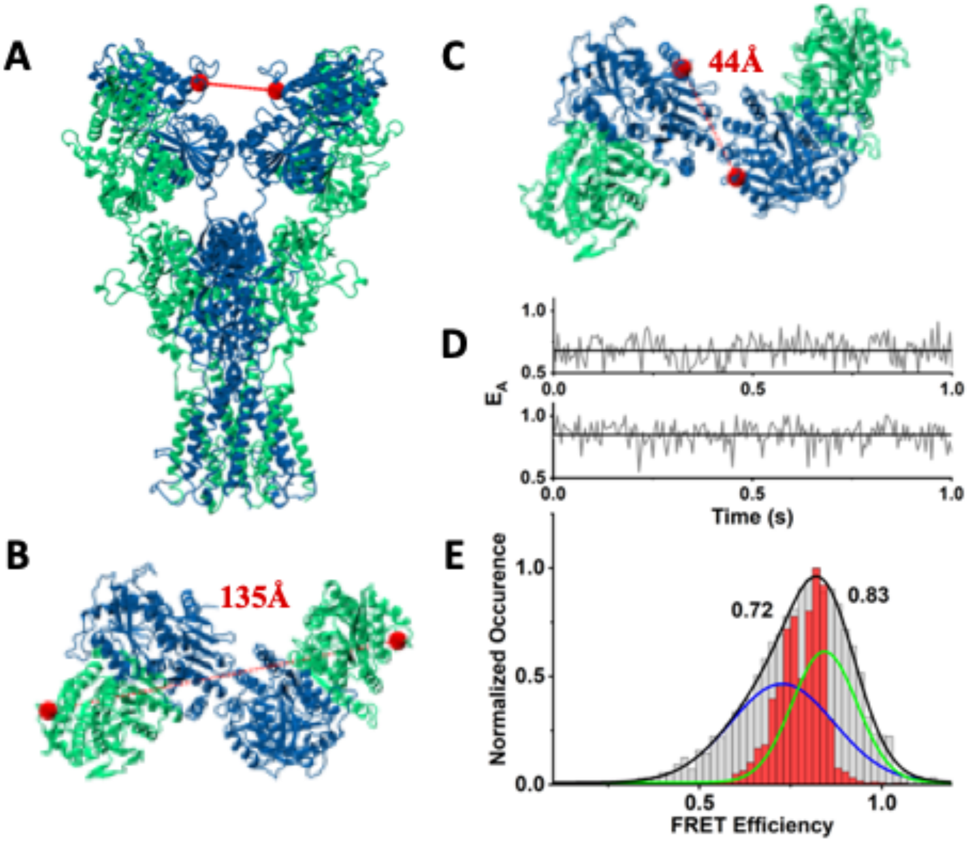

Figure 23. Homology models for heteromeric sites GluK2*-266 and GluK5*-272 with corresponding efficiency histograms.

(A) Full-length structure of the apo state GluK2/GluK5 heteromer (homology model made from PDB 3KG2) with the GluK2 subunits shown in blue and the GluK5 subunits shown in green. Alpha carbon sites at GluK2*-266 are shown as red spheres. (B-C) Top down view of alpha carbon sites at GluK5*-272 and alpha carbon sites at GluK2*-266 with their corresponding distances. (D-E) smFRET data for GluK2*-266 sites; with two representative smFRET efficiency traces for individual molecules shown in panel D and cumulative smFRET efficiency traces with observed data (grey) overlaid on denoised data (red) are shown in panel E. Gaussian fits shown in black, blue and green, represents the smFRET efficiency states.

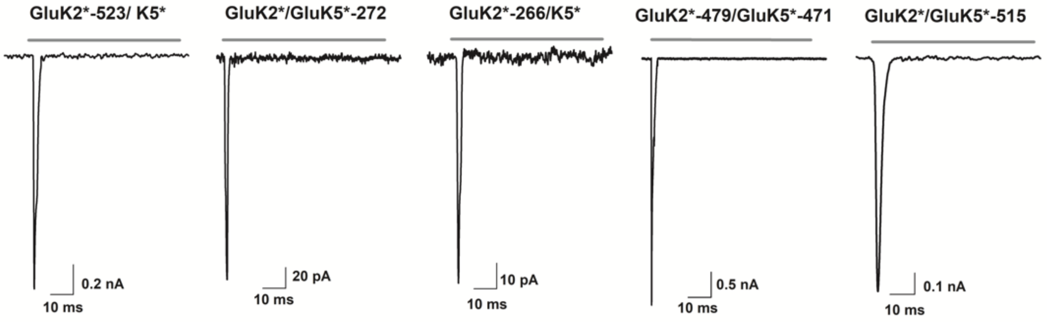

Figure 24. Heteromeric FRET construct characterization.

Representative whole-cell recording for GluK2*-523/GluK5*, GluK2*/GluK5*-272, GluK2*-266/GluK5*, GluK2*-479/GluK5*-471 and GluK2*/GluK5*-515.

smFRET traces for constructs GluK2*-266/GluK5* exhibiting a single donor and single acceptor photobleaching step with anticorrelation upon acceptor bleaching were used for generating the smFRET efficiency traces for individual molecules (representative trace shown in **Figure 23D**). The fractional occurrence in the smFRET efficiency traces were then used to generate the smFRET efficiency histogram. The cumulative histogram from smFRET efficiency traces from 28 molecules, for GluK2*-266/GluK5* is shown in (**Figure 23E**). The donor and acceptor traces were denoised using wavelet based denoising and the denoised FRET histograms generated from these are shown overlaid on the observed histogram (**Figure 23E**). The smFRET histogram shows primarily two states with a FRET efficiency of 0.72 and 0.83, corresponding to distances of 42 Å and 39 Å. These distances are close to the alpha carbon distance between the 266 and 266 residues (values are shown in **Table 1**) as predicated when placing the GluK2 subunits proximal to each other (**Figure 22A**). Additionally, given that this distance is significantly shorter than the distance of 67 Å expected in the configuration placing two GluK2 subunits within the dimer as seen in GluK2 homomer (PDB 5KUH), it can be concluded that the configuration with GluK2 (**Figure 22B**) within the peripheral position the dimer does not exist in the heteromer.

smFRET experiments for the GluK2*/GluK5*-272 receptors on the other hand showed no molecules with significant smFRET efficiency traces. 148 molecules probed exhibited one or multiple donor steps or one or multiple acceptor steps, but no molecules showed FRET between the donor and the acceptor. Based on this observation it can be concluded that no significant fraction of the GluK2/GluK5 heteromeric receptors exist in the configuration placing the GluK5 subunits proximal

Sites	Apo state		Desensitized state		Alpha carbon distance in Å for homology models		
	FRET Eff.*	Gaussian fit	FRET Eff.*	Gaussian fit	5KUF	3KG2	5KUH
GluK2*-266 -	0.72	0.72 (+/- 0.03					
GluK2*-266							
	0.83	0.84 (+/- 0.004	-	-	47	44	-
GluK2*-479 -	0.8	0.80 (+/- 0.003	0.56	0.56 (+/- 0.01)			
GluK5*-471			0.69	0.68 (+/- 0.003)			
	0.9	0.90 (+/- 0.001	0.83	0.83 (+/- 0.001)	37	39	57
			0.84	0.93 (+/- 0.002)			
GluK2*-523 -	0.83	0.83 (+/- 0.005)	0.85	0.83 (+/- 0.008)			
GluK2*-523							
	0.96	0.96 (+/- 0.002)	0.94	0.94 (+/- 0.002)	-	34	38
GluK5*-515 -	0.81	0.81 (+/- 0.003)	0.84	0.85 (+/- 0.01)			
GluK5*-515						34	38
	0.94	0.94 (+/- 0.002)	0.93	0.95 (+/- 0.003)	-		

Table 1. Summary of smFRET efficiencies and distances calculated

to each other (**Figure 22C**) and within a dimer (**Figure 22B**). Therefore, the heteromeric receptor exists primarily in the configuration shown in **Figure 22A**. and is consistent with the X-ray structure of the isolated amino-terminal domain of the GluK2-GluK5 heterotetramer (125).

Comparison of the conformational landscape of heteromeric to homomeric receptors at dimer-dimer interface at the amino-terminal domain.

The smFRET data of GluK2*-266/GluK5* show two states with FRET efficiencies of 0.72 and 0.83, while the smFRET data of homomeric GluK2 receptors at this site showed three states of FRET efficiencies 0.69, 0.83 and 0.92 (200). The most probable state of 0.83 is identical in both suggesting that the two receptors have a similar conformational arrangement of the dimer-dimer interface at the amino-terminal domain for the main conformational state. The similarity in primary conformation and lack of large-scale differences at the amino-terminal domain between the homomeric and heteromeric receptors would be consistent with the previous biochemical studies suggesting that the amino-terminal domain plays a major role in assembly (125, 204).

Conformational landscape of the agonist-binding domain.

To study the conformational dynamics at the dimer interface in the agonist-binding domain, we introduced cysteines at site 479 on GluK2* and 471 on GluK5* (**Figure 25A-B**). These sites are ideal as the distance between these residues are distinct within the dimer, relative to that across the dimers (**Figure 25B**). smFRET traces showing a single donor and single acceptor photobleaching step with anticorrelation between the two were used to generate the FRET efficiency traces, and 26-28 molecules were combined to generate the cumulative smFRET efficiency histograms. The smFRET histograms in the apo state show two states with efficiencies of 0.8 and 0.9 (**Figure 25D**), corresponding to distances of 40 Å and 35 Å. These distances are close to the alpha carbon distance between residues GluK2*-479 and GluK5*-471 (values are shown in Table 1) based on homology models when placing the subunits as in configuration **Figure 22A**, further confirming that this is the primary configuration for the heteromeric receptor. The smFRET histograms for the glutamate-bound state, on the other hand, shows four states with FRET efficiencies of 0.56, 0.69, 0.83 and 0.94 (**Figure 25D**). The lower FRET efficiency state 0.56 with a distance of 49 Å corresponds well with the distance of 51 Å observed in the desensitized state structure of GluK2 homomeric receptor (PDB 5KUH) showing a pseudo four-fold symmetry, suggesting that a fraction of the protein exists in the conformation similar to this structure under desensitizing conditions. However, the conformations with less decoupling at the dimer interface of the agonist-binding domain also exist suggesting that complete decoupling as seen in the pseudo four-fold symmetry is not essential for desensitization.

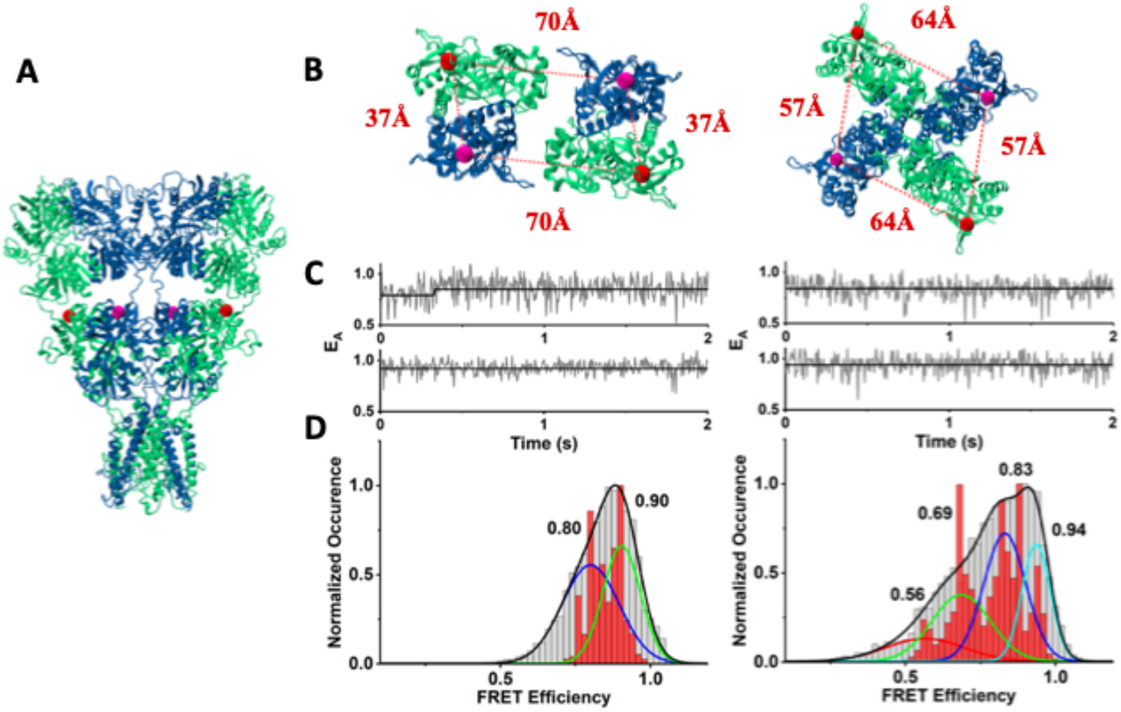

Figure 25. Homology model for heteromeric sites GluK2*-479 and GluK5*-471 with corresponding efficiency histograms.

(A) Full-length structure of the apo state GluK2/Gluk5 heteromer (homology model made from PDB 3KG2) with alpha carbon sites at GluK2*-479 (magenta spheres) and GluK5*-471 (red spheres). (B) Top down view of alpha carbon sites at GluK2*-479 (magenta spheres) and at GluK5*-471 (red spheres) with their corresponding measured distances at apo state (left panel) (homology model made from PDB 5KUH) and desensitized state (right panel) (homology model made from PDB 5KUF) of GluK2/GluK5 heteromer. (C-D) smFRET data for GluK2*-479 and GluK5*-471 sites at the apo state (left panel) and the desensitized state (right panel). (C) Two representative smFRET efficiency traces for individual molecules. (D) Cumulative smFRET efficiency traces with observed data (grey) overlaid on denoised data (red). Gaussian fits shown in black, blue and green, represents the smFRET efficiency states.

Comparison of the conformational landscape of heteromeric to homomeric receptors at the agonist-binding domain dimer interface.

The smFRET histograms of the heteromeric receptor in the apo state shows the additional lower FRET state of 0.8, which is not observed in the smFRET histogram of the homomeric GluK2 receptor in the apo state. The apo state of the homomeric GluK2 receptor exists in a single conformation with a FRET efficiency of 0.89 (200). The existence of a more decoupled second conformation in the heteromeric receptor is consistent with prior MD simulations with the isolated agonist-binding domain where a shift of about 1 Å towards a more decoupled state was observed (184). The smaller shift in the MD simulations versus that seen in the smFRET could be due to the fact that the distances were measured closer to the dimer interface in the MD simulations and not at the same site being studied in the smFRET measurements. Additionally, the simulations were on the isolated domain and it is possible that the changes are larger in the full-length receptor.

A favoring of the more decoupled state is also observed in the smFRET data for the glutamate-bound homomeric (desensitized) state (200). While, the FRET efficiencies of 0.56, 0.69, 0.83 and 0.94 in the glutamate-bound state for the heteromeric receptors are similar to the FRET efficiencies of 0.54, 0.69, 0.82 and 0.93 seen in the homomeric GluK2 receptors, the fractional occupancy is higher for the more decoupled state in the heteromeric receptors relative to the homomeric receptors. This shift towards the more decoupled state would be consistent with the faster desensitization rates observed in the heteromeric receptors relative to the homomeric receptors ($\tau_{\text{des GluK2/K5}}$ = ~3 ms, $\tau_{\text{des GluK2}}$ = 5.8 ms) in the presence of sodium ions (184).

Conformational landscape at the transmembrane segments.

In order to study the conformational dynamics at the transmembrane segments we introduced cysteines at site 523 on GluK2* and 515 on GluK5* (**Figure 26, 27**). These sites are positioned at the top of the first transmembrane segment, which makes them ideal to measure the distance across the pore axis at complementary sites. smFRET traces showing a single donor and single acceptor photobleaching step with anticorrelation between the two were used to generate the FRET efficiency traces, and 27-31 molecules were combined to generate the cumulative smFRET efficiency histograms. The smFRET histograms for GluK2*-523 in the apo state show two states with efficiencies of 0.83 and 0.96 (**Figure 26D**) and correspond to distances of 39 and 30 Å. These distances are close to the alpha carbon distance of residue 523 - 523 in the two GluK2 subunits obtained from the apo state homology model with the channel being in a closed state (**Figure 26 A-B, Table 1**). The higher FRET efficiency peak centered at 0.96 that corresponds to a distance of 30 Å possibly represents a tighter packing at the transmembrane segment. The smFRET histograms for GluK2*-523 in the glutamate-bound state show two peaks with efficiencies of 0.85 and 0.94 (**Figure 26D**), corresponding to distances of 38 and 32 Å. These efficiencies are similar to what is found under apo conditions at this site; however, there is a significant shift in occupancy toward the high FRET state, suggesting the more tightly packed transmembrane conformation is favored in the desensitized state.

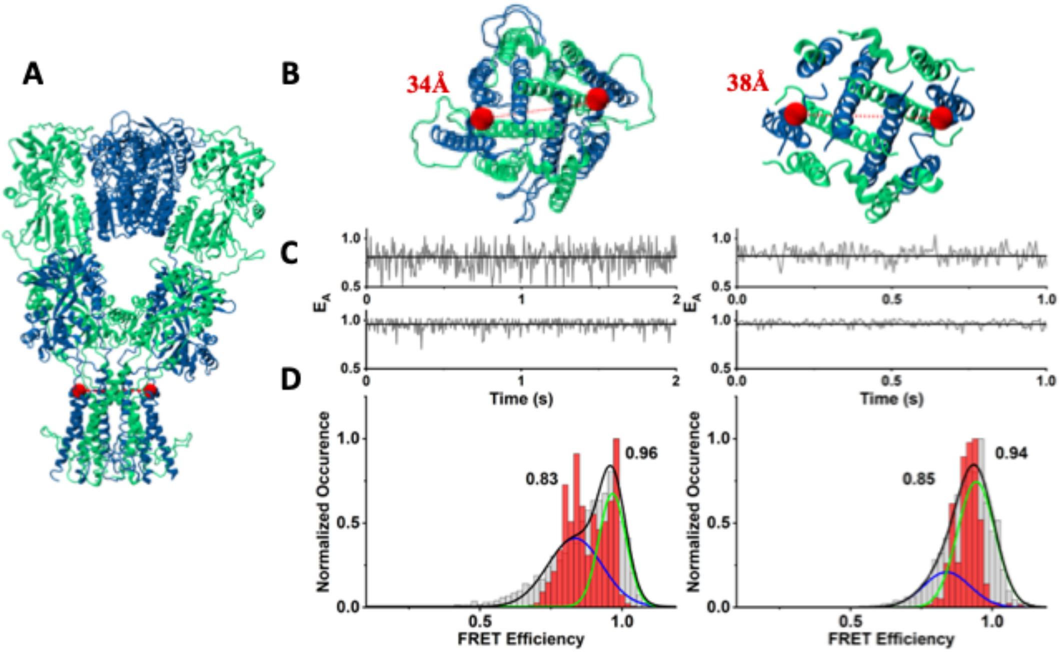

Figure 26. Homology model for heteromeric sites GluK2*523 and GluK5* with corresponding efficiency histograms.

(A) Full-length structure of the apo state GluK2/Gluk5 heteromer (homology model made from PDB 3KG2) with alpha carbon sites at GluK2*-523 (red spheres). (B) Top down view of the apo state (left panel) (homology model made from PDB 3KG2) and the desensitized state (right panel) (homology model made from PDB 5KUF) of GluK2/GluK5 heteromer displaying alpha carbon sites at GluK2*-523 (red spheres) with their corresponding measured distances. (C-D) smFRET data for GluK5*-523 sites at the apo condition (left panel) and the desensitized state (right panel). (C) Two representative smFRET efficiency traces for individual molecules. (D) Cumulative smFRET efficiency traces with observed data (grey) overlaid on denoised data (red). Gaussian fits shown in black, blue and green, represents the smFRET efficiency states.

The smFRET histograms for GluK5*-515 in the apo state show two states with efficiencies of 0.81 and 0.94 (**Figure 27D**) and correspond to distances of 40 and 32, and in the glutamate-bound state show two peaks with efficiencies of 0.84 and 0.93 (**Figure 27D**), corresponding to distances of 39 Å and 33 Å. The smFRET data from site GluK5*-515 are similar to site GluK2*-523 in the glutamate-bound state showing that at this site the protein exhibits a four-fold symmetry in both the apo and glutamate-bound state.

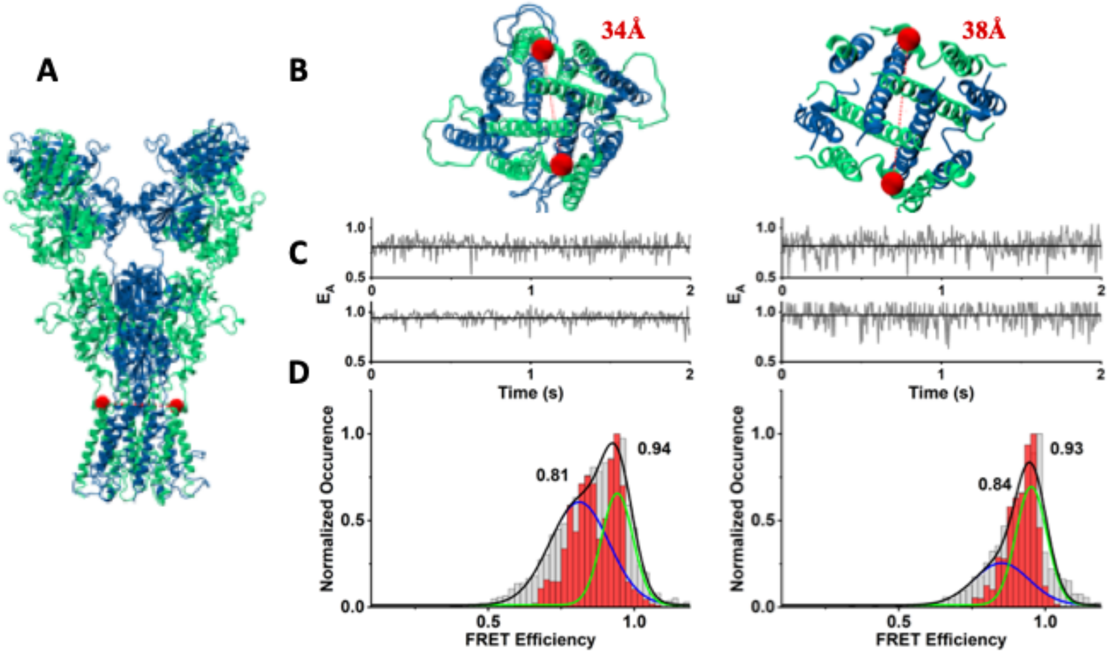

Figure 27. Homology model for heteromeric sites GluK2* and GluK5*-515 with corresponding efficiency histograms.

(A) Full-length structure of apo state GluK2/Gluk5 heteromer (homology model made from PDB 3KG2) with alpha carbon sites at GluK5*-515 (red spheres). (B) Top down view of the apo state (left panel) (homology model made from PDB 3KG2) and the desensitized state (right panel) (homology model made from PDB 5KUF) of GluK2/GluK5 heteromer displaying alpha carbon sites at GluK5*-515 (red spheres) with their corresponding measured distances. (C-D) smFRET data for GluK5*-515 sites at apo condition (left panel) and desensitized state (right panel). (C) Two representative smFRET efficiency traces for individual molecules. (D) Cumulative smFRET efficiency traces with observed data (grey) overlaid on denoised data (red). Gaussian fits shown in black, blue and green, represents the smFRET efficiency states.

Conclusions

There are a plethora of X-ray crystallography and cryo-EM structural models available for the AMPA and NMDA classes of iGluR including both isolated amino-terminal and agonist-binding domains, and also the full-length receptors. However, only three structural models have been produced for the full-length homomeric GluK2 receptor type. Currently, there are no structures of the full-length GluK2/GluK5 heteromeric receptor. Using smFRET investigations, we show that GluK2/GluK5 heteromeric receptor assemble in one configuration with the GluK2 sites occupying proximal positions across the dimer-dimer interface at the amino-terminal domains of the receptor. Additionally, we show that the spread of conformational states is not significantly different between the homomeric and heteromeric receptors at the dimer-dimer interface at the amino-terminal domain suggesting that the primary role of this domain is in assembly. The agonist-binding domain, on the other hand, shows more decoupling and a higher occupancy of the decoupled state at the dimer interface in both the apo and glutamate-bound states of the heteromeric receptors relative to what is observed in the homomeric receptors. Given the prior studies that have shown the decoupling of the dimer interface at the agonist-binding domain as being the primary conformational change driving desensitization, the increase in decoupling at this interface in the agonist binding domain of the heteromeric receptor ties back to the functional studies that show a faster desensitization rate in the heteromeric receptor relative to the homomeric receptors. The smFRET studies also show that the GluK2/GluK5 heteromeric receptors loses its two-fold symmetry and exhibits four-fold symmetry at the start of the first transmembrane segment in both the apo and the glutamate-bound forms of the receptors.

Chapter 8: The Effects of Neto Modulation on Kainate Receptor Structure

Parts of this chapter are based upon research originally published in *Biophysical Journal*. Prakash, P., D.B. Litwin, H. Liang, J. Hancock, V. Jayaraman and A. Gorfe. Dynamics of membrane-bound G12V-KRAS from simulations and single-molecule FRET in native nanodiscs. *Biophysical Journal*. 2019; 116(2): 179-183 © Biophysical Society.

As discussed in chapter 3, there are significant changes in the kinetics of KAR gating when co-expressed with Neto proteins. There is currently no structural data for Neto proteins or KARs as affected by Neto proteins. In order to characterize the structural effects of Neto modulation on KARs, LRET and cryo-EM experiments were conducted on the homomeric GluK2 KAR co-expressed with Neto2.

The architecture of the KAR positions the amino-terminal on the extracellular side of the plasma membrane. Neto proteins are also in this arrangement. Given that the two proteins are positioned with intercellular C-termini, it is not possible to create a tandem construct for structural studies, as has been done with AMPARs and stargazin. This creates difficulty in studying the structure of this complex using smFRET and cryo-EM.

LRET, however, provides an excellent platform for circumventing this issue. LRET experiments allow for measurements to be made on non-purified samples, such as HEK cells expressing the protein of interest as seen in previous chapters. Therefore, the amino-terminal domain constructs which retained function were ideal candidates to begin characterizing the structural influences of Neto proteins and as previously discussed, there is evidence that Neto proteins interact with the ATDs of the KAR. Given that loss of function was observed for KAR mutants designed for measurements in the ABD layer, purification strategies capable of maintaining the KAR-Neto interactions were further investigated.

While detergents like digitonin have been used in structural studies of protein complexes, there have been difficulties in obtaining quality samples of KARs purified using these methods. Therefore, solubilizing agents capable of forming nanodiscs including lipid bilayer were considered for testing. Currently, the only technologies shown to be capable of maintaining protein complexes in nanodiscs are membrane scaffold protein (MSP) and styrene maleic acid copolymers (SMA). Since SMA does not require pre-solubilization in detergents, a purification strategy utilizing SMA was optimized for use in cryo-EM studies of the KAR-Neto2 complex. Preliminary LRET and cryo-EM imaging experiments will be discussed in this chapter.

Amino-terminal domain LRET studies of the KAR-Neto complex

As discussed in chapter 3, several studies have highlighted the role of the ATD in the trafficking of Neto proteins. While the specific mechanisms involved in the KAR-Neto interaction are not currently known, these data hint that there could be important interactions between the KAR ATD and Neto proteins. For this reason, LRET experiments were conducted using construct GluK2*22C and GluK2*266C, and GluK2*22C and GluK2*266C co-expressed with Neto2. These constructs are design to monitor the distance within ATD dimer pairs and between ATD dimer pairs respectively. As previously mentioned, LRET experiments were limited to the ATD due to loss of function with ABD constructs.

In order to characterize the effect of Neto modulation on the KAR ABD dimers, LRET measurements were made on construct GluK2*22C. LRET decay plots for construct GluK2*22C co-expressed with Neto2 are shown in **Figure 28**. Under apo conditions and without Neto2 present, the LRET lifetime obtained is 731 μs. This corresponds to a distance of 44 ± 0.25 Å. Under glutamate-bound conditions without Neto2, the lifetime obtained was 718 μs, which corresponds to a distance of 44 ± 0.61 Å. Under apo conditions and with Neto2 co-expressed, the lifetime obtained was 580 μs which corresponds to a distance of 41 ± 1.1 Å. Under glutamate-bound conditions with Neto2 co-expressed, the lifetime was 573 μs, which corresponds to a distance of 41 ± 0.88 Å. These data show that there is slight decrease in distance at site 22C when GluK2 is expressed with Neto2.

In order to characterize the effects of Neto modulation on the distance between ATD dimer pairs, LRET measurements were conducted on construct GluK2*266C shown in **Figure 7**. The fluorescent decay plots for construct GluK2*266C are shown in **Figure 29**. Under apo conditions without Neto2 co-expressed the lifetime was 619 μs which corresponds to a distance of 42 ± 0.47 Å. Under glutamate-bound conditions without Neto2 co-expression the lifetime was 569 μs which corresponds to a distance of 41 ± 0.39 Å. Under apo conditions with Neto2 co-expressed the lifetime was 1003 μs, which corresponds to a distance of 50 ± 0.91 Å. Under glutamate-bound conditions Neto2 co-expression the lifetime was 990 μs, which corresponds to a distance of 50 ± 1.3 Å. These data indicate that when GluK2 is co-transfected with Neto2, the ATD dimer pairs are separated by a greater distance than when expressed alone.

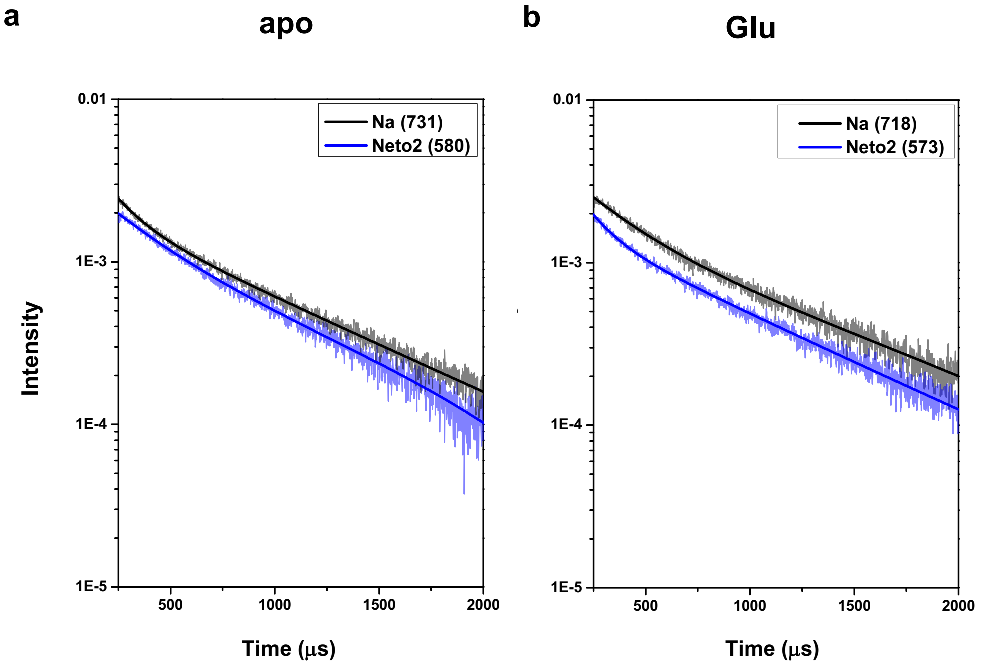

Figure 28. LRET data for amino-terminal domain construct GluK2*22C.

(a) Acceptor fluorophore decay plots under apo conditons for GluK2*22C (black) and in the presence of Neto2 (blue). (b) Acceptor fluorophore decay plots under glutamate-bound conditions for GluK2*22C (black) and in the presence of Neto2 (blue). Measurements were made using terbium chelate (donor) and fluorescein (acceptor).

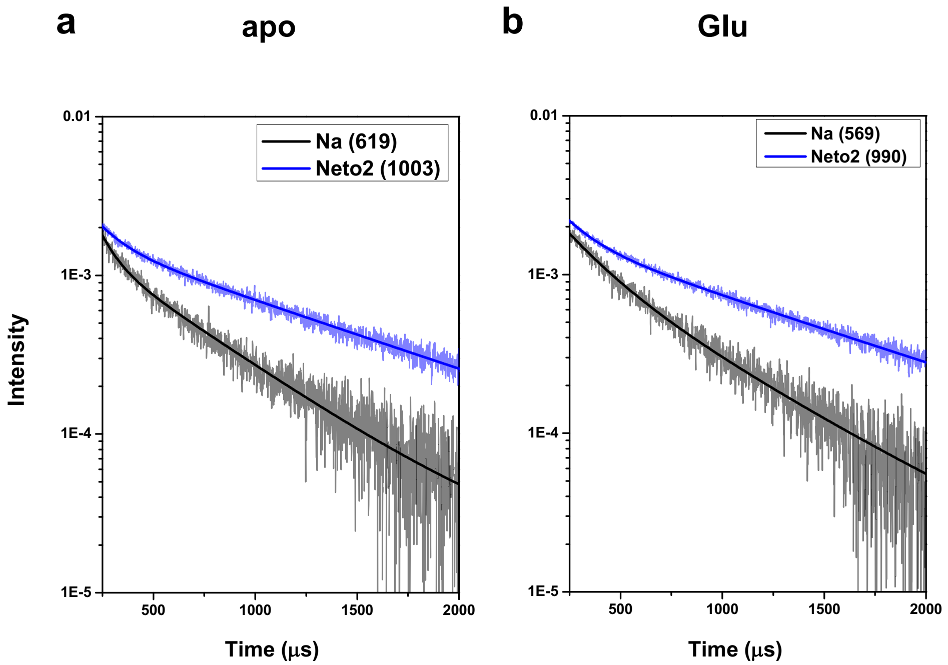

Figure 29. LRET data for the amino-terminal domain construct GluK2*266C. (a) Acceptor fluorophore decay plots under apo conditons for GluK2*266C (black) and in the presence of Neto2 (blue). (b) Acceptor fluorophore decay plots under glutamate-bound conditions for GluK2*266C (black) and in the presence of Neto2 (blue). Measurements were made using terbium chelate (donor) and fluorescein (acceptor).

Agonist-binding domain LRET studies of the KAR-Neto complex

To measure the effect of Neto co-expression on the ABD dimer proximity, construct GluK2*458 was characterized using LRET, shown in **Figure 30**. Fluorescent decay plots are presented in **Figure 31**. Under all conditions, florescent decay plots which fit to double exponential decay were produced. Under apo conditions without Neto2 co-expressed, lifetimes of 669 and 1148 μs were obtained, which corresponds to distances of 43 ± 0.91 Å and 54 ± 1.6 Å. Under glutamate-bound conditions without Neto2 co-expression the lifetimes obtained were 529 and 1051 μs, which corresponds to distances of 40 ± 0.41 Å and 51 ± 1.47 Å. These distances are different than those obtained previously using cryo-EM; however, the faster lifetime corresponding to 40 Å fits well in the cryo-EM models, while the longer lifetime corresponding to 51 Å is significantly shorter than expected, as seen in **Figure 30**. It is also important to note that at this site it is not possible to determine if the longer lifetime has contribution from the diagonal distance between sites being measured (see **Figure 30**).

Under apo conditions with Neto2 co-expressed the lifetimes were 479 and 1016 μs, which corresponds to distances of 39 ± 0.53 Å and 50 ± 1.3 Å, **Figure 31b**. Under glutamate-bound conditions with Neto2 co-expression the lifetimes were 503 and 1055 μs, which corresponds to distances of 40 ± 0.32 Å and 51 ± 1.2 Å. These data show a decrease in distance between ABD dimer pairs when co-expressed with Neto2. This indicates that Neto2 induces a tighter packing of the ABD layer and likely explains the gain in function by conferring additional support between the dimer pairs.

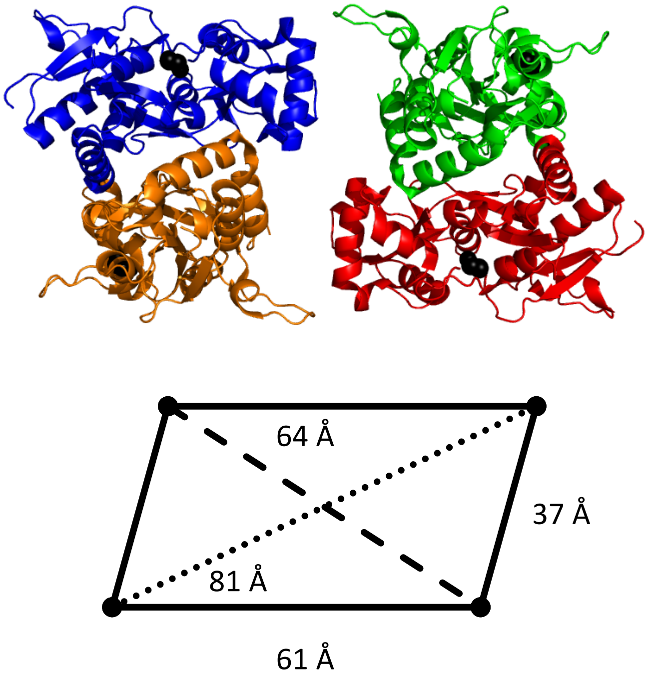

Figure 30. Structural model of a homomeric kainate receptor showing site 458. (Upper panel) top-down view of homomeric GluK2 with site 458 shown as black spheres. (Lower panel) geometry of distances between site 458.

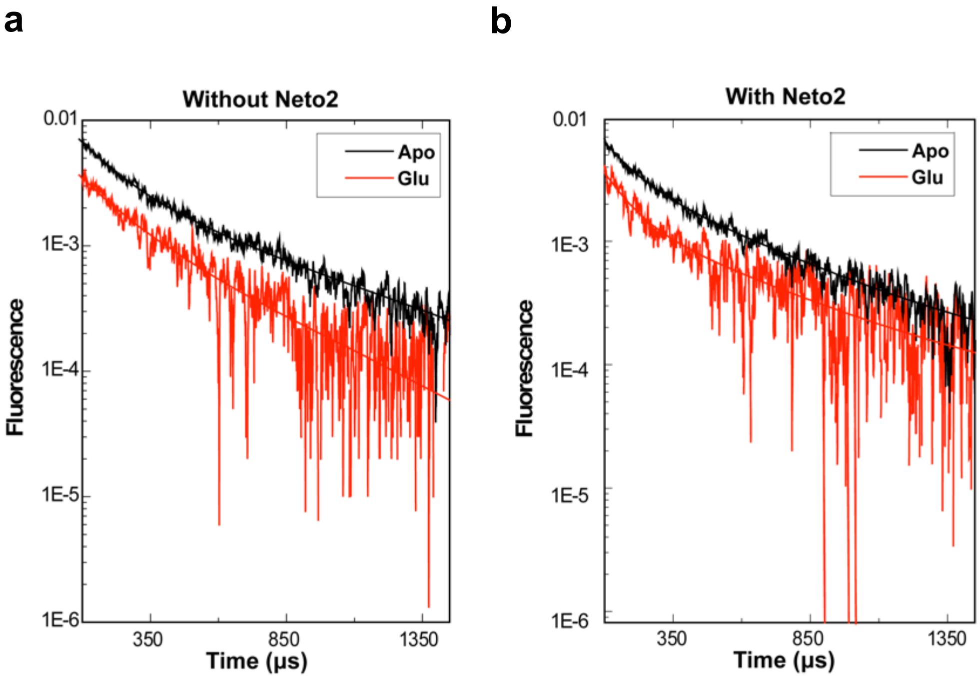

Figure 31. Agonist-binding domain LRET acceptor decay plots with double exponential lifetime fits.

(A) Construct GluK2*458C measured under apo conditions (black) and glutamate-bound conditions (red). (B) Construct GluK2*458C co-expressed with Neto2 measured under apo conditions (black) and glutamate-bound conditions (red).

Cryo-electron microscopy studies of the KAR-Neto complex

Styrene maleic acid solubilization

As previously discussed, there are experimental difficulties in studying the KAR-Neto complex which result from the inability to create a tandem construct for characterization. The concern results from the inability to ensure that all of the KARs are paired with Neto proteins. When using detergent to solubilize proteins, the detergent molecules typically displace the lipids and proteins interacting with the receptor at the membrane. This problem can be overcome through the use of styrene maleic acid (SMA) to solubilize the complex. Previous studies have shown that receptors solubilized in SMA not only retain a disk of lipids surrounding the protein, they retain the native lipids normally associated with the proteins (205, 206).

Solubilization of KRAS

There are a number of structural models and molecular dynamic simulations published for KRAS proteins; however, resolving functionally relevant conformational states has been limited by their functional requirement for a bilayer. Therefore, the data available for KRAS proteins makes it an ideal protein to validate and optimize a protocol for SMA solubilization. In order to optimize a SMA purification protocol for use in smFRET and cryo-EM, experiments characterizing the membrane protein KRAS using smFRET were performed.

The mammalian RAS family of proteins includes the isoforms NRAS, HRAS, and KRAS. RAS proteins are GTP signaling proteins tethered to the inner side of the plasma membrane. After binding GTP, RAS proteins transduce extracellular signals to the nucleus through signaling cascades. KRAS has become of particular interest for its potential in treating cancer due to studies showing that mutations altering its GTP activity lead to a variety of cancers (207, 208).

The structure of KRAS proteins is composed of a bi-lobed catalytic domain and a flexible C-terminal hypervariable region containing a polybasic and farnesylated lipid anchor. It is known that the KRAS catalytic domain can also interact with anionic model membranes in three orientation states (OS). OS1 involves interactions with α-helices 3-5 on lobe 2. OS2 involves interactions with β-strands 1-3 on lobe 1, and OS0 in which α-helices are perpendicular to the membrane. The OS1 and OS2 conformations show different accessibility to the β-stand loops critical for coordination with downstream signaling proteins, which suggests the KRAS signaling could be modulated by membrane reorientation (209, 210). However, currently only inferences can be made from MD simulations and indirect spectroscopic techniques in simple model membranes (209-212).

In these studies, we characterize the dynamic interactions between the catalytic domain of KRAS and membrane lipids using a combination of atomistic MD simulation and single-molecule fluorescence resonance energy transfer (smFRET). Given the importance of the lipid membrane to KRAS structure, these experiments were conducted with KRAS solubilized in styrene maleic acid nanodiscs.

MD simulations were run and the distance between residue 132 on lobe 2 of the catalytic domain and residue 183 on the C-terminal were analyzed. The MD simulations yielded results showing three dominant KRAS orientations with distances of 19, 33 and 49 Å between sites 132 and 183, corroborating the 3 state model including OS1, OS2 and OS0. However, the short timescales of the MD simulations limited the number of transitions between different orientations. Therefore, smFRET measurements were made to help resolve the frequency of transitions between the different orientations. The smFRET efficiency histogram for G12V-KRAS is shown in **Figure 32**. Efficiency peaks were found centered at 0.40, 0.74, and 0.94. These FRET efficiencies correspond to distances of 49, 39, and 29 Å, which are very similar distribution to the distances obtained with MD simulations. These results indicate that the SMA purification strategy is sufficient to isolate the KRAS protein into nanodiscs suitable for use in biophysical characterization. These results showed promise in utilizing SMA for purification of the KAR-Neto complex, and that process was investigated further.

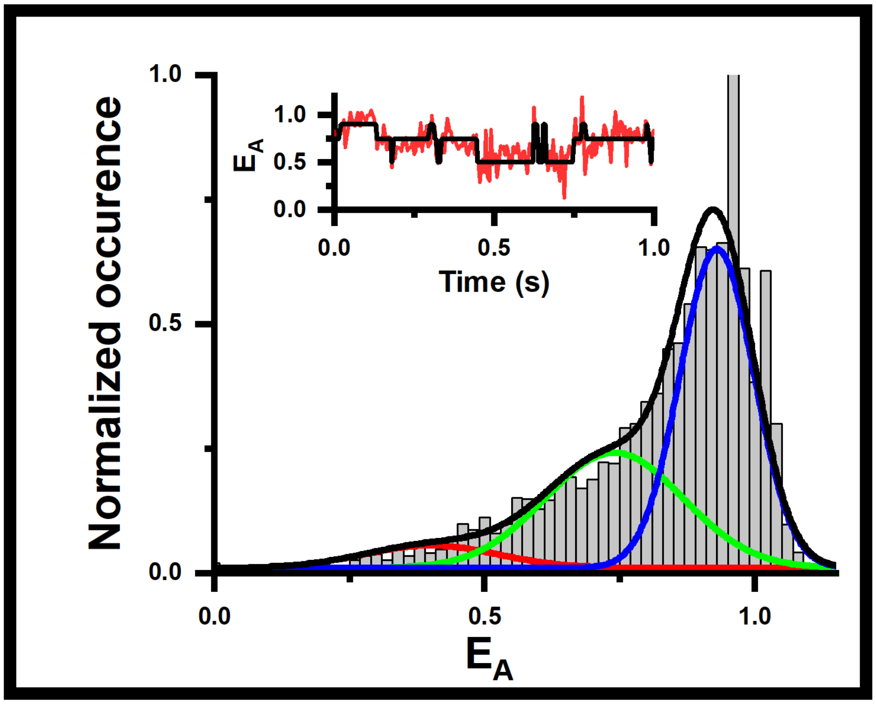

Figure 32. Representative trace and efficiency histogram for KRAS FRET construct.

(A) FRET efficiency (EA) histogram fitted to three Gaussians, indicating three distinct conformational states, with the high FRET state in blue, mid-FRET state in green, and low FRET state in red. A representative EA trajectory indicating fast transitions between states is shown as an inset, with the observed signal in red and state transitions highlighted in black.

Purification and imaging of the GluK2-Neto2 complex

Characterizing the structural arrangement and molecular interactions between GluK2 and Neto2 would be best accomplished using cryo-EM imaging. There are now several molecular models for the AMPA receptor in complex with its auxiliary proteins resolved using cryo-EM, but no structural data is available for the KAR-Neto complex. Therefore, the purification strategy optimized for the KRAS protein was adopted for use with the KAR-Neto complex.

Initially, the KAR-Neto complex was expressed and purified using HEK293T cells; however, the yields obtained from this expression system were inadequate for cryo-EM imaging. Therefore, the insert containing the GluK2 and Neto2 constructs were separately cloned into pFastBac1 vectors to be used in the generation of baculovirus. The baculoviruses generated were then used to co-transfect SF9 insect cells in order to produce high quantities of the GluK2-Neto2 complex.

The SMA purification strategy optimized for the KRAS protein was then adapted to a double purification scheme. For affinity chromatography purposes, the GluK2 construct included a hexa-histidine tag and the Neto2 construct included a FLAG tag. After SMA solubilization, the SF9 cell lysates were applied to a Ni-NTA resin and followed by elution using imidazole. Next the eluate was applied to a anti-FLAG resin, washed and eluted using 3X FLAG peptide. Both GluK2 and Neto2 were clearly detected in the double purified eluate on western blots and ran as a single band on a native page gel, see **Figure 33**.

The samples obtained following the double FLAG and His purification were then imaged on a Technai G2 Polara cryo-electron microscope. The microscopy resulted in successful imaging of the receptor; example micrograph shown in **Figure 34**. The receptors appear as tetrameric Y-shaped molecules, similar to what has previously been described.

While these initial micrographs were promising, there were difficulties in producing a signal oligomeric species with the purification protocol. The eluate obtained from purification likely contains a mixture of various oligomeric states of the complex. This is commonplace when purifying oligomers for structural imaging and gel filtration chromatography is the traditional method for separating the different oligomeric species. The yield obtained from the double purification was typically in the 0.1-0.4 mg/ml range. However, the yield following gel filtration chromatography dropped to between 0.005-0.01 mg/ml. The UV chromatograph also showed that the majority of the protein was either retained in the column or exited in the void volume as aggregate. Therefore, additional work must be done refining the purification strategy to obtain samples that are homogenous enough to move forward with image analysis.

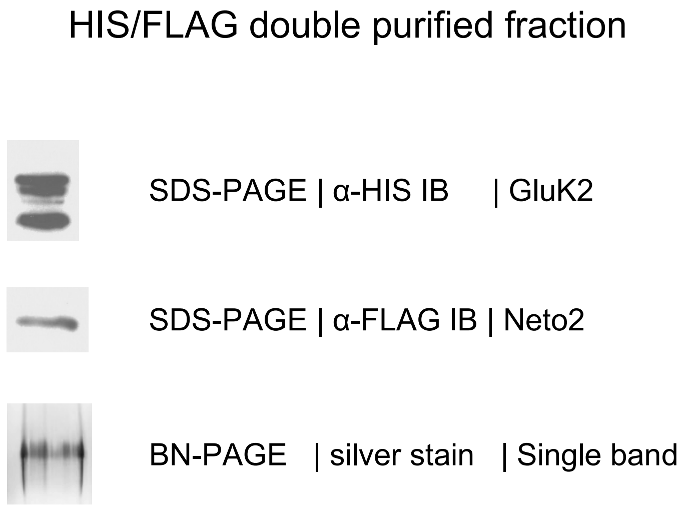

Figure 33. Representative SDS and native PAGE gel imaging.

Representative SDS-page imaging using anti-GluK2 and anti-Neto2 antibodies.

Representative blue native page gel imaging using silver stain.

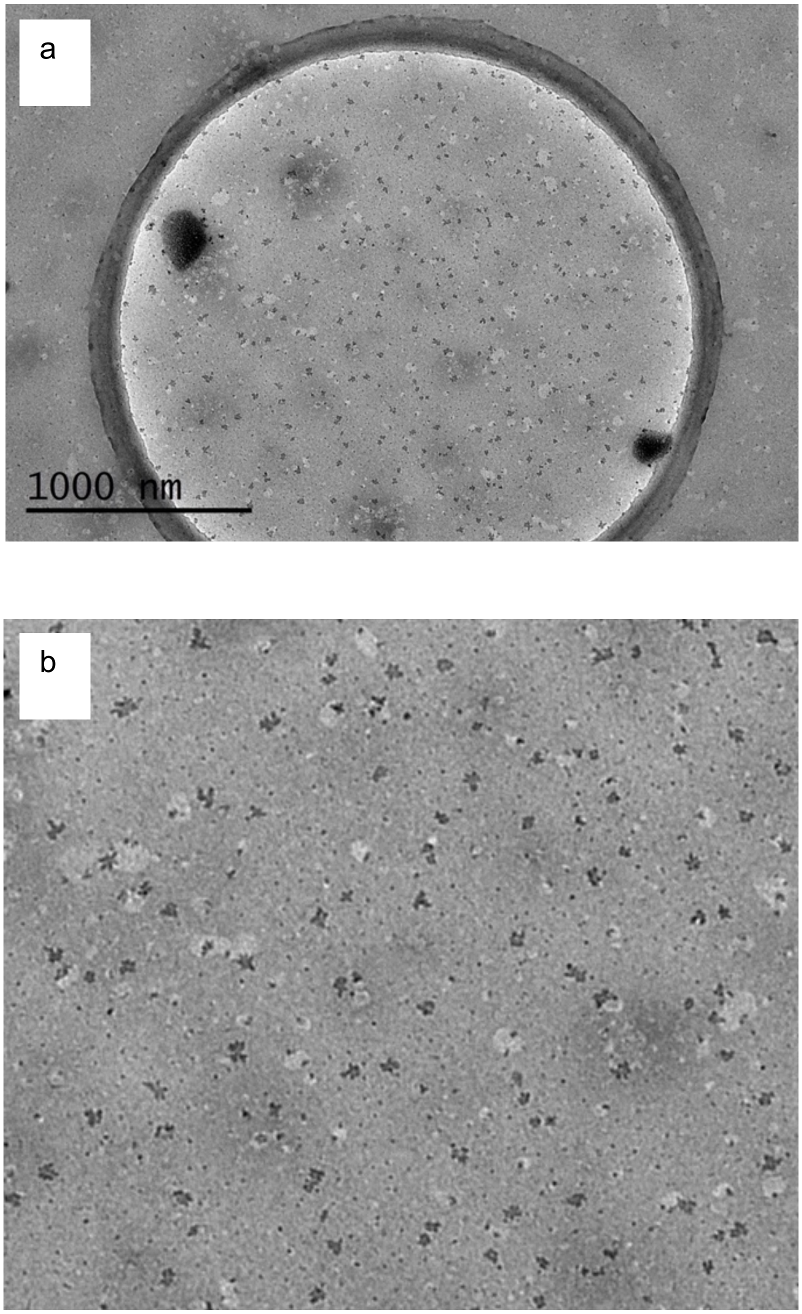

Figure 34. Representative cryo-EM micrograph.

(a) Representative cryo-electron micrograph of the GluK2-Neto2 purified fraction on a holey carbon grid. (b) Enlarged area from the micrograph showing the KAR-Neto2 complex.

Discussion

The LRET experiments presented show that Neto2 modulation affects the conformational arrangement of the ABD layer. Neto2 co-expression produced measurements with shorter distances between dimer pairs, indicating the ABDs are in a more tightly packed arrangement. These are intriguing data showing that, not surprisingly, KAR kinetics are being modulated by altering the conformation and therefore the dimer interface interactions. Unfortunately, the mutations required for LRET experiments nullified the function of the receptor when positioned to measure within the ABD layer. Therefore, it could not be determined that the structural effects we found are relevant to the true function involved in Neto2 modulation or if they arise from misfolding introduced through the mutated residues. These limitations are not a concern for investigations utilizing smFRET and these experiments will be performed.

The strategy for purification of the KAR-Neto2 complex has produced promising results; however, the problems in obtaining high-yield samples following gel filtration chromatography have limited the progress made imaging the complex. These studies are currently being continued through a collaborative effort with Columbia University and preliminary results look promising.

Chapter 9: Conclusions and Future Directions

The work presented herein contributes to our understanding of the structure function relationship in kainate receptors. Prior to these studies, there were no data characterizing the structural dynamics of either full length homomeric or heteromeric kainate receptors. Here we used a combination of LRET and smFRET to reveal the underlying structural dynamics that drive kainate receptor function and modulation by ions and auxiliary proteins. The data we obtained are consistent with many of the previous studies regarding kainate receptor gating, ion modulation and auxiliary protein modulation. However, our findings regarding the dynamics of the glutamate-bound state refine our understanding iGluR gating.

These studies show that unlike what is seen in the AMPA receptor, the ATDs of the homomeric and heteromeric KAR maintain relatively low dynamics and remain in close proximity throughout the gating cycle. We show that the ABDs retain a tightly coupled dimer interface under apo conditions which agrees with previous structural studies. We show for the first time in kainate receptors that the ABDs remain tightly coupled during the active state and that separation at the dimer interface is the initiating step for entry into the desensitized state. Interestingly, the glutamate-bound data confirm the previously-hypothesized existence of multiple receptor states. In addition, the data show that the higher FRET states are favored indicating that the extreme decoupling seen in current KAR models is likely an artifact of the purification process for cryo-EM. This finding stands in contrast to our current understanding of KAR desensitization, yet is in agreement with a previous study suggesting that decoupling at the ABD dimer interface is not required for gating.

The heteromeric studies show that the ATDs occupy similar distances and dynamics between homomeric and heteromeric KARs and are in agreement with previous structural studies. The ABDs, however, show significant differences between homomeric and heteromeric receptors with the heteromer showing decoupling in both the apo and glutamate-bound states. The decoupling found in the heteromeric glutamate-bound state shows less preference for the more coupled interface as compared to the homomeric receptor. These structural differences are in agreement with functional differences seen between homomeric and heteromeric KARs, showing more rapid entry into the desensitized state in heteromers.

The investigations into the structural effects of Neto modulation show that, similar to what is found in the AMPARs, the auxiliary protein is reorienting the ABD dimer pairs into a more compact arrangement. A reorientation of this nature would affect the stability of the ABD dimer interface and explains the gain in function resulting from Neto co-expression. Collectively these experiments highlight the importance of the ABD dimer interface in receptor function.

As discussed and examined throughout this dissertation, the interface within the ABD dimers is critical for receptor function. The current model of iGluR gating puts the decoupling of the ABD dimer interface as the major driving force regulating receptor kinetics. While the ABD interface is certainly the most important site regulating gating kinetics, the decoupling previously found in KAR models is not corroborated by our data nor by structural models of the AMPA receptor co-expressed with auxiliary proteins. In both the homomeric and heteromeric studies, distances corresponding to current structural models are found but represent the least favored state. This finding highlights the importance of characterizing the dynamics of proteins under conditions more similar to what the receptor experiences in its native environment. While imaging the receptor under crystalized or vitrified conditions is critical for understanding the tertiary and quaternary arrangement of the proteins, it is insufficient for accurately resolving structural dynamics and the conformational arrangements involved with function.

Given the difficulties in obtaining high resolution KAR models and the inherently dynamic nature of iGluRs, it seems clear that a combination of static and dynamic experimentation is required for a comprehensive understanding of mechanisms underlying the processes of activation and desensitization. The work presented in this dissertation advances our understanding of KARs by combining previously resolved structural models with physiologically relevant conformational states and the dynamics of the full-length homomeric and heteromeric KAR. The combination of these data makes it possible to more accurately model receptor behavior using MD simulations and identify topological chemistries ideal to discriminate between iGluR subtypes and KAR subunit compositions. The advances in knowledge made through these studies bring the possibility of introducing novel therapeutic drugs targeting iGluRs closer to reality.

Future directions

While these data progress our understanding of the structure/function relationship in KARs, significant work remains to be done. KARs have consistently proven to be difficult receptors to work with in regard to advancing our understanding of their molecular structure and mechanisms. However, our laboratory is well positioned to unite the most cutting-edge structural dynamic experimentation with static models to resolve these difficult questions.

Further investigations into the agonist-binding domain

The experiments performed here on the ABD identify the one-dimensional changes in distance relevant to receptor function in homomeric and heteromeric KARs. In the homomeric receptor, we were limited to measurements being made across the dimer interface near site 479 due to the convoluting effects of having the labeling site on all four subunits. While these measurements are critical for understanding the dynamics at this interface, it cannot resolve the 3-dimensional movements of this domain in homomeric KARs.

The heteromeric receptor provides a platform in which a series of one-dimensional measurements made from different positions within the ABD and between the ABD and ATDs can be made. While only measurements complementary to the homomeric site have been made thus far, additional points of measurement are not restricted as in the homomeric receptor. Further studies performed on additional sites within the ABD, between the ABD and the ATD, and measurements made between the ABD and lipids would integrate the 3-dimensional movements within the protein complex, providing a complete picture of the dynamic landscape to be used as constraints in MD simulations.

Neto interactions at the amino-terminal domain

The KAR amino-terminal domain has received the least attention of all the domains. As previously discussed, there are no allosteric regulatory effects found in the ATD and very little dynamics are shown. Our data align with previous studies identifying the ATD's involvement in Neto trafficking, which is significant for receptor function. Currently only LRET studies have shown that Neto co-expression significantly alters the conformational arrangement of the ATDs. Further experiments utilizing smFRET to characterize the effect of Neto proteins on the ATD should be performed. smFRET measurements made between ATD dimers and within the ATD dimer pairs would verify the altered conformation observed using LRET. Additionally, smFRET measurements made between the ATDs and different CUB domains within the Neto proteins could be used to triangulate the position of Neto proteins relative to the receptor; similar to what our laboratory has previously done with the AMPA-stargazin complex.

A closer look at the transmembrane domain

Of the ordered domains of KARs, the transmembrane domain has been most difficult to study due to experimental limitations. In the homomeric KAR it is not possible to make LRET or smFRET measurements in this region due to its small radius. However, as seen in this dissertation, the heteromer allows for measurements to be made in this domain. Measurements characterizing the effect of Neto modulation would be of great value given that studies have shown that residues just above the transmembrane helices are critical for Neto modulation.

The carboxyl-terminal domain

The CTD remains the most mysterious region of KARs due to their intrinsically disordered nature. While it is unlikely that detailed crystallography or cryo-EM models will resolve this region, smFRET could provide detailed insight into this question. Fluorescent proteins have already been used in FRET experiments on CTD position and smFRET with organic fluorophores would increase the resolution significantly. Experiments measuring the dynamic effects of calmodulin and many other intracellular signaling proteins binding to the CTD would shed light on the structure-function relationship of this domain for the first time.

Neto proteins and modulation

We have shown that Neto proteins affect the orientation of the ABD and ATD using LRET. Yet the mechanisms mediating their interaction, their sites of interaction and the conformational arrangement of the Neto proteins remain in question. Fortunately, there are a number of structural studies performed on CUB domain-containing proteins homologous to Neto proteins. Given that we have structural insight into CUB domains, and the tertiary structure of those domains is highly conserved, these questions can and should be addressed using smFRET. smFRET measurements made within and between the CUB domains when bound to the KAR would resolve the structural arrangement of Neto proteins. Additional measurements made between the Neto protein and the KAR ATD and ABD would reveal the architecture of the KAR-Neto complex. Importantly, these data would provide a complementary view of the complex to be compared to the cryo-EM structure of the complex when it becomes available.

New technologies for the study of membrane protein complexes

Cell signaling is one of the most important physiological functions in biology. Given that signaling involves transducing a signal across a membrane, it is no surprise that the majority of proteins involved in signaling cascades are membrane proteins. Difficulties in studying membrane proteins arise from their transmembrane architecture. Solubilizing membrane proteins for studies requires the use of amphipathic molecules to bind their hydrophobic TM regions. Traditionally detergents are used for solubilization; however, the nature of detergent and the concentration used needs to be precisely optimized for success.

In recent years, membrane scaffold protein (MSP) and SMA copolymers have been used to more efficiently solubilize membrane proteins. MSPs are advantageous in that they allow for relatively precise control of the nanodisc size obtained; however, they typically require prior solubilization into detergent. SMA, on the other hand, allows for the direct solubilization of membrane proteins from native membranes. This retains the native lipid environment and keeps the receptor associated with other membrane proteins. Structures have been published using SMA solubilized samples and have shown the utility of SMA while removing the need for time consuming detergent screening. Given the success of previous studies and our own SMA purification, it seems that SMA has a bright future in structural biology.

More recently, developments in fluorophore and microscope technology have increased the power of smFRET measurements to operate with four fluorescent molecules, termed four-color FRET. This is groundbreaking technology in that it converts the single dimensional measurement obtained in traditional FRET measurements into multidimensional measurements. Experiments utilizing four color FRET are able to quantitate the allosteric motions involved in complex protein complexes in single measurements. iGluRs serve as a perfect subject for four color FRET and, if used in combination with the ever-increasing power of MD simulations, will revolutionize our view into the dynamics of the molecular world.

Final thoughts

Kainate receptors are fascinating and yet underappreciated proteins which, along with other ionotropic receptors, have been instrumental in the evolution of cognition in vertebrate species. The work presented in this dissertation has increased our understanding of the structure-function relationship of kainate receptors, yet much remains to be discovered. However, as computational technology and scientific techniques continue to evolve, the mysterious link between synaptic transmission, neural oscillation patterns, and cognition will be revealed.

Appendix: Materials and Methods

Homomeric Studies

Parts of this section are based upon research originally published in *Scientific Reports*. Litwin, D. B., E. Carrillo, S. A. Shaikh, V. Berka, and V. Jayaraman. The structural arrangement at intersubunit interfaces in homomeric kainate receptors. *Scientific Reports*. 2019; 9(1):6969 © Springer Nature Publishing AG.

Generation of FRET mutants

The *R. norvegicus* $\mathrm{GluK2_{EM}}$ construct (26, 29) was kindly provided by Dr. Mark Mayer and retained the native glutamine at site 590. The coding sequence for GluK2 was PCR amplified and inserted into pcDNA3.1. Mutations were introduced using standard PCR-based mutagenesis methods. To create the background construct GluK2*, non-disulfide-bonded cysteines at sites C91, C199, C432, were mutated to serines. On this background two constructs were made; one with S266 mutated to cysteine and one with A479 mutated to cysteine. A third construct was made in which both A479C and D776K mutations were introduced.

Electrophysiology

Mutant HEK 293T cells were transfected using jetPRIME PolyPlus (wt-GluK2, GluK2*S266C, and GluK2*A479C) or lipofectamine 2000 Invitrogen (GluK2*A479C-D776K), and were, in both conditions, co-transfected with GFP at a microgram ratio of 3:1 per 10 ml of media. After 4-6 h of incubation, cells were re-plated (30 mm dishes) at low density. Cells were labeled in dish with 400 nM of donor fluorophore Alexa 555 maleimide (ThermoFisher) and 400 nM of acceptor fluorophore Alexa 647 maleimide (ThermoFisher) in 2 mL extracellular buffer pH 7.4 (150 mM NaCl, 1.8 mM $MgCl_2$, 1 mM $CaCl_2$, 3 mM KCl, 10 mM glucose, and 10 mM HEPES). Whole cell patch clamp recordings were performed 24-48 h after transfection, using fire-polished borosilicate glass (Sutter instruments) pipettes with 3-5 mΩ resistance, filled with internal solution: 110 mM CsF, 30 mM CsCl, 4 mM NaCl, 0.5 mM $CaCl_2$, 10 mM HEPES, and 5 mM EGTA (adjusted to pH 7.4 with CsOH). The external solutions containing 150 mM NaCl or CsCl, 2.8 mM KCl, 1.8 mM $CaCl_2$, 1.0 mM $MgCl_2$, and 10 mM HEPES (adjusted to pH 7.4 with NaOH or CsOH) were (without and with 10 mM glutamate) applied to lifted cells using a stepper motor system (SF-77B; Warner Instruments) with triple barrel tubing. Recordings were performed using an Axopatch 200B amplifier (Molecular Devices) at –60 mV hold potential, acquired at 10 kHz using pCLAMP10 software (Molecular Devices), and filtered online at 5 kHz.

LRET sample preparation

HEK293T cells were transiently transfected according to JetPrime protocol at 10 µg per 10 cm plate and maintained in DMEM. For LRET measurements, cells were transfected with a GluK2 construct alone. Cells were collected and washed three times using extracellular buffer containing 160 mM NaCl, 1.8 mM MgCl2, 1 mM CaCl2, 3 mM KCl, 10 mM glucose, and 10 mM HEPES (pH 7.4). The washed HEK cells were then labeled with 400 nM donor and 100 nM acceptor fluorophores in 3 ml extracellular buffer, rotating at room temperature in the dark for 1 hr. The donor fluorophore was terbium chelate (Invitrogen), and the acceptor fluorophore was fluorescein maleimide (Thermo Fisher Scientific) for cysteine mutants. After labeling, cells were washed and resuspended in 2 ml extracellular buffer and used for LRET measurements. Extracellular buffer used in Cs^+ substitution experiments contained 150mM CsCl in place of NaCl.

LRET data collection

A cuvette-based system consisting of a fluorescence lifetime instrument (EasyLife L;Hoiba) and analysis software (Fluorescan 5.5; Optical building blocks) was used for LRET measurements. All samples were excited at 337 nm. Emission was detected at 545 nm for donor-only samples, at 515 nm for fluorescein-labeled samples. LRET measurements were taken in triplicate for a given condition followed by scans after Factor Xa protease cleavage to quantitate the samples' background signals without the labeled receptors' contribution to the signal. Fluorescent decay plots obtained for given conditions and the background for that condition were then plotted in Origin and averaged, and the background was subtracted from the full signal. Following background subtraction, the resulting decay plots were fit to double exponential decay functions thereby quantitating the decay lifetime of the acceptor fluorophore. Error in the distance estimates was then calculated by propagating the errors in the donor and acceptor lifetimes using the Error Propagation Calculator developed by Thomas Huber in the Physics Department of Gustavus Adolphus College. Lifetimes were quantitated for samples labeled with only the donor (t_D) and samples labeled with both donor and acceptor (t_{DA}), to be used to calculate the distance between the fluorophores using the Forster equation:

$$\boldsymbol{R = R_0(\frac{\tau_{DA}}{\tau_D - \tau_{DA}})^{1/6}}$$

where R is the distance between donor and acceptor fluorophore, R_0 is the distance yielding half-maximal energy transfer for a given fluorophore pair (45 Å for terbium-fluorescein), t_D is the measured lifetime of the donor when bound to the protein and without acceptor fluorophore present, and t_{DA} is the lifetime of the donor fluorophore when bound to the protein and transferring energy to the acceptor fluorophore, which we have measured here as the lifetime of the sensitized emission of the acceptor. For LRET experiments, the number of biological replicates for apo, glutamate, apo-CsCl, and glutamate–CsCl was, respectively, $n = 3$. Final lifetime values for given conditions were obtained by averaging the Background-subtracted lifetime values per day.

smFRET sample preparation

HEK293T cells were transiently transfected according to JetPrime protocol at 10 μg per 10 cm plate. One day post-transfection, cells from two 10-cm dishes were harvested and washed with extracellular buffer and labeled for 1 h at room temperature with 400 nM of donor fluorophore Alexa 555 maleimide (ThermoFisher) and 400 nM of acceptor fluorophore Alexa 647 maleimide (ThermoFisher) in 3 mL extracellular buffer. This concentration of fluorophore was determined to be optimal for single donor and single acceptor labeling. After washing, labeled cells were then solubilized for 1 h at 4 °C in solubilization buffer consisting of phosphate-buffered saline, 1% lauryl maltose neopentyl glycol (MNG-3) (Anatrace), 2 mM cholesteryl hydrogen succinate (MP Biomedicals), and ¼ protease inhibitor tablet (Pierce). Unsolubilized debris were then spun down for 1 h at 100,000 × g at 4°C, and the supernatant used as the smFRET sample. Samples were then diluted 1:2 in cold SB before application.

smFRET flow chamber preparation

Coverslips (22 × 22 mm No. 1) were washed with Liqui-Nox phosphate-free detergent (Alconox Inc.) and 4.3% NH_4OH and 4.3% H_2O_2. Coverslips were then plasma cleaned using a Harrick Plasma PDC-32G Plasma Cleaner and then aminosilanized through Vectabond treatment (Vector Laboratories). A circular area on the slide was then isolated using Silicone templates (Grace bio-Labs) and treated with a PEG solution containing 5 kDa biotin-terminated PEG (2.5% w/w in molecular biology grade (MB) water, NOF Corp.), and 5 kDa mPEG succinimidyl carbonate (25% w/w in MB water, Laysan Bio Inc.) in 0.1M sodium bicarbonate (Sigma-Aldrich) overnight in a dark and moist environment. On the day of the experiment, the coverslips were washed with PBS, treated with short chain 333 Da NHS-ester PEG (Thermo Scientific) and incubated for 2–3 h. Slides were then washed and dried with N_2 gas. A chamber was then constructed over the treated circular area by applying hybriwell chambers (Grace bio-Labs) then dual silicon press-fit tubing connectors (Grace bio-Labs).

smFRET protein preparation and attachment to coverslip

Streptavidin was applied to the chamber by flowing 32 μl of a buffer solution containing phosphate-buffered saline (PBS), 1 mM DDM (*n*-dodecyl-β-D-maltoside), 0.2 mM CHS (cholesteryl hydrogen succinate), and 0.2 mg/mL Streptavidin through the flow chamber and incubating for 10 min. 10nM of biotinylated goat Anti-Rabbit IgG (H+L) secondary antibody (Jackson Immunoresearch Laboratories, Inc., cat. no. 111-065-003) was then flowed into the chamber, incubated for 20–30 min, then washed with PBS. Next, 10 nM of anti-GluK2 (C-terminal epitope) mouse monoclonal primary antibody (Abcam, cat. no. ab15307) was flowed in, incubated for 20–30 min, and washed with PBS. This antibody was chosen as it is far from the extracellular sites being studied. Detergent solubilized HEK293T cell membranes containing GluK2 receptors were then bound to a glass slide using the *in situ* immuno-precipitation (SiMPull(213)) method for FRET data acquisition. 60 μL of the sample was applied twice through the chamber followed by a 20–30 min incubation before flushing the chamber with 60 μl oxygen scavenging solution buffer system (ROXS) buffer twice. ROXS buffer used consisted of 1 mM methyl viologen, 1 mM ascorbic acid, 0.01% w/w pyranose oxidase, 0.001% w/v catalase, 3.3% w/w glucose (all from Sigma-Aldrich), 1 mM DDM (Chem-Impex), and 0.2 mM CHS (MP Biomedicals, LLC) in PBS, pH 7.4. 1 mM glutamate was added and/or 150 mM CsCl was used to replace NaCl in the ROXS to achieve the experimental conditions and 1mM UBP310 was included for antagonist-bound experiments.

smFRET data acquisition

For Single molecule FRET measurements were acquired using a custom-built PicoQuant MicroTime 200 Fluorescence Lifetime Microscope. smFRET data acquisitions were conducted using pulsed interleaved excitation at 80 MHz. Both 532 nm (LDH-D-TA-530; Picoquant) and 637 nm (LDH-D-C-640; Picoquant) lasers were simultaneously used to characterize the fluorescent behavior of both fluorophores and the efficiency of energy transfer between molecules potentially showing FRET. The sample slide was immobilized on a scanning *x*-*y*-*z* piezo stage (P-733.2CD; Physik Instrumente) while being excited and observed through a 100x oil immersed lens (100× 1.4 NA; Olympus). The photons emitted from the sample post-excitation were collected back through the objective, separated through a dual band dichroic beam splitter (Zt532/640rpc-UF3; AHF/Chroma) and sent to two SPAD photodiodes (SPCM CD3516H; Excelitas technologies) preceded by excitation filters. A 550 nm (FF01-582/64;AHF/Semrock) and 650 nm (2XH690/70;AHF) emission filter were used for the donor and acceptor channels, respectively. All acquisitions were performed in the presence of a photo-stabilizer and oxygen scavenging solution buffer system (ROXS).

smFRET molecules selection and analysis

Since the kainate receptors studied here are homomeric, there is a distribution of various donor/acceptor combinations. To exclude signal from those channels having multiple donors or multiple acceptors, the fluorescence intensity of single channels and the step-wise photobleaching was studied. Multiple donors or acceptors have multiple photobleaching steps and these traces were not used. The number of photobleaching steps per molecule in the 266 and 479 data sets exhibited the following distribution: 10% showed four steps, 50% showed three steps, 35% showed two steps, and 5% showed one step. The FRETing regions of the smFRET traces obtained for all constructs were on average 1 to 3 seconds in length. Only the traces with a clear single photobleaching step in both donor and acceptor channels were included in the analysis. This molecule hence reports on a single distance between single donor and single acceptor. Such a strategy has been used successfully by us as well as several other laboratories (134, 158, 214, 215).

The fluorescence intensity of the donor and acceptor (upon excitation of donor) were used to calculate FRET efficiencies as described in these references (134, 155-158, 160, 170, 178). The photon counts produced per donor and acceptor excitation were acquired at 1 ms resolution, binned to 5 ms, and denoised with wavelet decomposition, and the calculated efficiencies were then plotted as separate histograms showing the occurrence of photons at their observed FRET efficiencies. Each count in the histogram represents one 5 ms bin, with the cumulative of all such counts from all the molecules normalized.

The number of states that best describes the distribution of FRET efficiencies found in the obtained FRET data was then determined using Step Transition and State Identification (STaSI) analysis (180) and hidden Markov modeling using HAMMY (179) and fit to Gaussian distributions.

While we have provided distances based on the smFRET intensities it should be noted the distances are between the fluorophores and hence the size and length of the fluorescent probes brings additional errors in the estimation of distances. Thus we focus on the change in distances and heterogeneity between the different states being studied. This is a reasonable assumption as the size of the probes is not expected to change between the states being studied. Furthermore, the heterogeneity and transitions across states are evident in the single molecule traces where a given donor-acceptor pair is being probed.

<u>Free energy calculations</u>

The free energy of the most populated state identified by STaSI analysis was set to 0 kBT. The percent occupancies as determined by STaSI were then used to calculate the equilibrium constant K_{eq} between states, and the free energy of every state relative to the most populated state was determined using the equation:

$$\Delta G^0 = -k_B T \ln K_{\text{eq}}$$

The transition probabilities between each pair of states, given our 5 ms bin time, was used to determine the reaction rate for each transition, and the heights of the energy of activation barriers were calculated assuming a first-order reaction rate and using the Arrhenius equation:

$$k = Ae^{-Ea/k\text{B}T}$$

Where k is the rate constant, the concentration of the starting state was taken as the STaSI-derived fractional occupancy of that state, and the value of the pre-exponential was chosen to be 10 ms^{-1}. Forward and reverse energies of activation were averaged in the final figure.

Statistics

Data were analyzed using Origin (OriginLab Corp.), MATLAB (MathWorks), and Excel (MicrosoftCorp.). For smFRET experiments, the numbers of molecules that passed cross- and anti-correlation checks for A479C-apo, A479C-glutamate, A479C-apo-CsCl, A479C-glutamate–CsCl, S266C-apo, S266C-glu, D776K-glutamate, D776K-glutamate- CsCl, S266C-UBP310 and A479C-UBP310 were, respectively, *n* = 57, 66, 55, 52, 47, 50, 47, 55, 29 and 28.

Heteromeric studies

Parts of this section are based upon research originally published in *Biochimica et Biophysica Acta- Biomembranes*. Litwin, D. B., N. Paudyal, E. Carrillo, V. Berka, and V. Jayaraman. The structural arrangement and dynamics of the heteromeric GluK2/GluK5 kainate receptor as determined by smFRET. *Biochimica et Biophysica Acta- Biomembranes*. 2019; DOI: 10.1016/j.bbamem.2019.05.023 © Elsevier B.V.

Homology modeling

3 homology structures were made for heteromeric GluK2/GluK5. 2 models were built based on homomeric GluK2 one in antagonist bound form (PDB 5KUF) and other in agonist-bound form exhibiting desensitized state (PDB:5KUH). These models were built using SWISS MODEL server accessible via EXPASy web server (216). The third model was built based on the antagonist bound AMPA structure (PDB:3KG2). This model was built using MODELLER software (217) . Antagonist bound structures represent closed state similar to apo structure and hence are used for the analysis of apo state.

Generation of FRET constructs

The R. norvegicus GluK2 construct used previously in cryo-EM (26, 29) and smFRET (200) experiments was used and retained the native glutamine at site 590. The GluK2 coding sequence was PCR amplified and inserted into pcDNA3.1. The background GluK2 FRET construct was created by mutating the non-disulfide bonded cysteines C91, C199 and C432 to serines. From this background five constructs were created. One with S266 mutated to cysteine, one with A479 mutated to cysteine, one with S523 mutated to cysteine, one with both A479C and D776K mutations, and one with both S523C and D776K mutations.

The R. Norvegicus construct containing GluK5 was kindly provided by Geoffrey Swanson, PhD. The GluK5 coding sequence was PCR amplified and inserted into pcDNA3.1. The background GluK5 FRET construct was created by mutating the cysteines C14, C88 and C270 to serines. From this background five constructs were created. One with S265 mutated to cysteine, one with A471 mutated to cysteine, one with S515, one with both A471C and D776K mutations and one with both S515C and D776K mutations.

<u>Electrophysiology</u>

HEK 293T cells at 30% confluency were transfected using lipofectamine 2000 (Invitrogen) with GluK2 and GluK5, co-transfected with GFP at a microgram ratio of 1:4:0.5. Whole cell patch clamp recordings were performed 24-48 h after transfection, using firepolished borosilicate glass (Sutter instruments) pipettes with 3-5 mΩ resistance, filled with internal solution: 110 mM CsF, 30 mM CsCl, 4 mM NaCl, 0.5 mM CaCl2, 10 mM HEPES, and 5 mM EGTA (adjusted to pH 7.4 with CsOH). The external solutions contained 150 mM NaCl, 2.8 mM KCl, 1 mM CaCl2 and 10 mM HEPES (adjusted to pH 7.4 with NaOH). The glutamate (10 mM) was applied to cells using a stepper motor system (SF-77B; Warner Instruments) with Triple barrel tubing. Recordings were performed using an Axopatch 200B amplifier (Molecular Devices) at

–60 mV hold potential, acquired at 10 kHz using pCLAMP10 software (Molecular Devices) and filtered online at 5 kHz.

smFRET sample preparation

HEK293T cells grown on 10cm plates were checked for approximately 50% confluency. The cells were then transfected with 20 µg DNA per 10 cm plate following JetPrime protocol. DMEM media was changed after four hours of transfection and was left for overnight expression. Next day, cells were collected from two transfected 10 cm plates and were washed with 3mL of extracellular buffer (ECB). The sample was then wrapped in foil and was labeled with 400 nM of Alexa 555 maleimide (ThermoFisher), a donor fluorophore and 400 nM of Alexa 647 maleimide (ThermoFisher), an acceptor fluorophore, in 3mL ECB at room temperature for 1hr. The labelled cells were washed with 3mL ECB and were resuspended in 2mL of solubilization buffer by nutating at 4°C for one hour. Solubilization buffer consists of phosphate-buffered saline, 1% lauryl maltose neopentyl glycol (Anatrace), 2 mM cholesteryl hydrogen succinate (MP Biomedicals), and ¼ protease inhibitor tablet (Pierce). The nutated sample was then transferred to an ultracentrifuge tube and was spun for one hour at 44000 rpm at 4°C using a TLA 100.3 rotor for filtering unsolubilized debris. Supernatant thus collected were used as smFRET samples and were kept on ice until they were used.

smFRET slide preparation

Microscope glass slides (20 × 20 mm) were cleaned in a solution of Liquinox phosphate-free detergent (Alconox Inc.) via bath sonication followed by washing with solution consisting 4.3% NH_4OH and 4.3% H_2O_2. Slides were then washed with purified water, dried with nitrogen gas and placed in metal slide holder. Plasma cleaning of the slides was done using Harrick Plasma PDC-32G Plasma Cleaner and then the slides were treated with Vectabond (Vector Laboratories, CA) for aminosilanization and stored under vacuum. Clean silicone templates (Grace bio-Labs) which were bath sonicated, and methanol treated were dried using nitrogen flow and were placed at the center of the slides. The slides were then treated with 50µl of PEG solution (0.25% w/w biotinylated PEG, 25% w/w mPEG-succinimidyl carbonate, 0.1M $NaHCO_3$) and incubated in a dark moist environment overnight. On the day of the experiment, after cleaning the slides with purified water and dried with nitrogen, slides were applied with short chain PEG solution (25mM short-chain 333 Da $MS(PEG)_4$ Methyl-PEG-NHS-Ester Reagent, 0.1 M $NaHCO_3$) and were incubated at room temperature for two to three hours. Then, the slides were washed with water, dried with nitrogen and silicone templates were removed followed by applying Hybridwell chambers and press-fit tubing connectors (Grace bio-Labs). 36 µl of streptavidin solution (0.2 mg/mL streptavidin, 1×smFRET imaging buffer (1mM DDM (n-dodecyl-β-D-maltoside), 0.2mM CHS (cholesteryl hydrogen succinate), 1×PBS) was applied to the chamber, incubated for 10 minutes and was washed with 1×PBS. The smFRET sample was then applied to the slide and incubated at 4°C for 20 minutes followed by washing of slides two times with 60 µl ROXS (reactive oxygen species) scavenging solution (3.3% w/w glucose, 0.1mg/mL pyranose oxidase, 0.01 mg.mL catalase, 1mM ascorbic acid, 1mM methyl viologen and/or 1mM glutamate) (Sigma-Aldrich). Finally, the slides were ready for imaging.

smFRET data collection

A PicoQuant MicroTime 200 Fluorescence Lifetime Microscope, a kind of confocal microscope, was used for acquiring the smFRET data with pulsed interleaved excitation (PIE) set at 80 MHz. The fluorophores were excited by using 532 nm (LDH-D-TA-530; Picoquant) and 637 nm (LDH-D-C-640; Picoquant) lasers simultaneously. The sample slide positioned on a scanning x-y-z piezo stage (P-733.2CD; Physik Instrumente) was observed through an oil immersed 100X objective lens (100× 1.4 NA; Olympus). Two SPAD photodiodes (SPCM CD3516H; Excelitas technologies) collected photons emitted from the sample passing through objective to the emission filters 550 nm (FF01-582/64; AHF/Semrock) and 650 nm (2XH690/70;AHF) to the photodiodes.

smFRET data analysis

Molecules exhibiting a single donor and single acceptor photobleaching step with anticorrelation upon acceptor bleaching were used for analysis. Intensities for donor and acceptor were then used for the calculation of FRET efficiencies. MATLAB (MathWorks) was used for denoising donor and acceptor traces using wavelet based denoising. Origin (OriginLab Corp) was used for obtaining smFRET histograms which included overlaid denoised and observed data, and gaussian curve fitting to represent FRET states. The total number of molecules used for the analysis of each conditions are, 28 molecules for GluK2*-266 - GluK2*-266, 26-28 molecules for GluK2*-479 - GluK5*-471, and 27-31 molecules for GluK2*-523 - GluK2*-523 and GluK5*-515 - GluK5*-515.

KRAS smFRET studies

Parts of this section are based upon research originally published in *Biophysical Journal*. Prakash, P., D.B. Litwin, H. Liang, J. Hancock, V. Jayaraman and A. Gorfe. Dynamics of membrane-bound G12V-KRAS from simulations and single-molecule FRET in native nanodiscs. *Biophysical Journal*. 2019; 116(2): 179-183 © Biophysical Society.

Extraction of G12V-KRAS in native NDs

To measure FRET distance between fluorophore-labeled residues 132 and 183 (ζ^*), we generated a hemagglutinin (HA)-His-tagged G12V-KRAS with D132C/T183C/C118S mutations (G12V-KRAS*). In this construct, D132C and T183C provide surface-exposed cysteines for site-specific fluorescent labeling, whereas C118S eliminates the only surface cysteine to avoid nonspecific labeling. The C118S mutation does not affect structure or function (218). Similarly, we do not expect major structural or functional effects from mutations at the surface residues D132 or T183. The His tag was added to aid surface immobilization, and HA to enhance expression of the Cys mutant KRAS. The construct was expressed in baby hamster kidney (BHK), cells grown to confluency, and styrene-maleic acid (SMA) extracted in NDs, as follows. Intact cells suspended in phosphate-buffered saline (PBS) containing 20 μg/mL deoxyribonuclease and 0.5 mM phenylmethylsulfonyl fluoride were treated with 2% SMA for 1 h at room temperature under rotation. After ultracentrifugation at 100,000 × g for 1 h at 4°C, the supernatant containing ND-bound G12V-KRAS* was collected and quantified using Western blotting. On the day of analysis, the supernatant containing ND-G12V-KRAS* was incubated with a 1:4 molar ratio of Alexa Fluor 555 (donor) and Alexa Fluor 647 (acceptor) maleimide (Invitrogen, Carlsbad, CA) for 1 h at room temperature under rotation. Excess dye was removed using a PD-10 desalting column (GE Healthcare Life Sciences, Waukesha, WI).

FRET data acquisition and analysis

The labeled protein was diluted 5× and immobilized on a glass surface for smFRET measurements. A custom-built PicoQuant MicroTime 200 Fluorescence Lifetime Microscope was used for smFRET measurements at 80 MHz using pulsed interleaved excitation. The 532 nm (LDH-D-TA-530; PicoQuant, Berlin, Germany) and 637 nm (LDH-D-C-640; PicoQuant) lasers were used to characterize the efficiency of energy transfer between molecules potentially showing FRET. The sample was excited and observed through a 100× oil immersed lens (100× 1.4 NA; Olympus, Tokyo, Japan) while immobilized on a scanning x-y-z piezo stage (P-733.2CD; Physik Instrumente, Auburn, MA). The photons emitted from the sample post excitation were separated through a dual-band dichroic beam splitter (Zt532/640rpc-UF3; adaptive high frequency [AHF]/Chroma, Los Angeles, CA) and sent to two single-photon avalanche photodiodes (SPCM CD3516H; Excelitas Technologies, Fremont, CA). The 550 nm (FF01-582/64; AHF/Semrock, Rochester, NY) and 650 nm (2XH690/70; AHF) emission filters were used for the donor and acceptor channels, respectively. ROXS was used during all data acquisitions. The photon counts were acquired at 1-ms resolution, binned to 10 ms, denoised with wavelet decomposition, and plotted as separate histograms showing the occurrence of photons FRETing at their observed efficiencies.

Step transition and state identification (STaSI) analysis was then used to determine the number of states that best describes the distribution of FRET efficiencies found in the obtained FRET data. The free energy (in terms of k_BT) associated with each STaSI-identified state (ΔG) was calculated by setting the most populated state to 0 k_BT and using the frequency of state occurrences relative to the most populated state as . The energy barriers between states were assumed to be of first-order kinetics and calculated using the Arrhenius equation. The concentration of the starting state was taken as the STaSI-derived fractional occupancy of that state. Forward and reverse energies of activation were averaged. Data were analyzed using Origin (OriginLab, Northampton, MA), MATLAB (The MathWorks, Natick, MA), and Excel (Microsoft, Tulsa, OK). For smFRET experiments, after filtering out the molecules that failed the anticorrelation check, the number of particles was $n = 13$.

LRET and cryo-EM into Neto2 modulation

LRET studies of Neto2

LRET experiments were prepared and analyzed as previously discussed.

Generation of baculovirus constructs

The open reading frame containing GluK2 and eGFP used previously in cryo-EM experiments (26) was cloned into a pFastBac1 vector using the Gibson Assembly method. The open reading frame for Neto2 was cloned into a pFastBac1 vector using the Gibson Assembly method.

P1 baculovirus stock

Approximately 8x10^5 SF9 cells were plated into a six well plate and allowed to adhere for 20 min. media was aspirated and replaced with plating media (1.5 ml Grace's insect medium- 10% FBS with 8.5 ml Grace's insect medium) 8 µl of Cellfectin reagent was then diluted into 100 µl Grace's media unsupplemented. 2 µl of bacmid DNA was diluted into plating media, then mixed by lightly flicking the tube. The Cellfectin and DNA solutions were then mixed and incubated at room temperature for 30 minutes. The mixture was added dropwise onto the cells, mixed and incubated at 27°C for 5 hours. After 5 hours, the media was aspirated and replaced with Graves's medium + 10% FBS. After observing 70% of cells lysing, the supernatant was removed, centrifuged at 500 x *g* for 5 minutes and the remaining supernatant was kept as the P1 stock. Viral titers were determined using 1:10 dilutions and plaque quantitation. P2 viral stocks were generated by applying the P1 stock at an MOI of 0.1 to SF9 cells seeded at 2x10^6 cells per well, incubating 48 hours, and collecting the supernatant. Again, viral titers were determined using 1:10 dilutions and plaque quantitation.

Expression

500 ml SF9 suspension cultures were prepared at 1 x 10^6 cells per ml. P2 viral stock was added at an MOI of 1 per construct and incubated at 27°C for 48 hours. The media was collected, centrifuged at 1,000 x *g* for 15 minutes and the cell pellet was kept for analysis. Cell viability was quantitated using trypan blue.

Purification for cryo-EM

Approximately 300 x 10^6 transfected SF9 cells were resuspended in 5 ml PBS. The cells were centrifuged at 1,000 x *g* for 15 minute and the supernatant was removed. The cells were resuspended in lysis buffer (5 mM MgCl, 2.5 mM KCl, 1.5 mM KH2PO4, 150 mM NaCl, 8 mM Na2HPO4, 0.1 mM CaCl2, 1 µg/ml DNase, pH 7.4), then lysed using a *parr* bomb pressurized to 750 psi for 5 min. cell debris was cleared by centrifuging at 500 x *g* for 10 minutes, then membrane fractions were collected by centrifuging at 100,000 x *g* for 30 minutes. The supernatant was aspirated, and the cell pellet transferred to a Dounce homogenizer. The pellet was then homogenized into 7 ml lysis buffer (no DNase with fresh protease inhibitors). The homogenized membrane fraction was then mixed with 7 ml SMA buffer (5 mM MgCl, 2.5 mM KCl, 1.5 mM KH2PO4, 150 mM NaCl, 8 mM Na2HPO4, 0.1 mM CaCl2, 3.3 % SMA, pH 7.4) and incubated overnight at room temperature with gentle shaking. The sample was then spun at 100,000 x *g* for 1 hour. The supernatant was then applied to Ni-NTA resin in batch format and gently rocked at 4°C for 4 hours. The resin was allowed to settle at 1 x *g* for 20 minutes. The resin was then washed three times in 10 ml PBS-Arg buffer and followed by elution in 2 ml PBS-Arg buffer containing 400 mM imidazole. The eluate was fractionated using a superdex 6 10/200 gel filtration column (GE) and the fractions containing the complex were combined and concentrated using spin columns (Amicon).

Cryo-EM imaging

The purified KAR-Neto2 complex at approximately 0.3 mg/ml protein were plunge frozen on Quantifoil holey grids (Quantifoil Micro Tools GmbH) The grids were previously covered with a thin continuous carbon film and glow-discharged for 5 seconds. Vitrification was performed at 80–90% humidity, 22°C using a Vitrobot (FEI). The grids were imaged using a Technai G2 Polara electron microscope (FEI) operated at 200 kV using a K2 Summit direct electron detector camera (Gatan).

Funding Acknowledgements

This project was supported by NIH grant R35- GM122528 (Vasanthi Jayaraman), the Houston Area Molecular Biophysics Program Grant No. T32GM008280-28 (Douglas Bryan Litwin)

Bibliography

1. Dingledine, R., K. Borges, D. Bowie, and S. F. Traynelis. 1999. The glutamate receptor ion channels. *Pharmacological Reviews* 51: 7-62.
2. Traynelis, S. F., L. P. Wollmuth, C. J. McBain, F. S. Menniti, K. M. Vance, K. K. Ogden, K. B. Hansen, H. Yuan, S. J. Myers, and R. Dingledine. 2010. Glutamate receptor ion channels: Structure, regulation, and function. *Pharmacological Reviews* 62: 405-496.
3. Chen, W., R. Prithviraj, A. H. Mahnke, K. E. McGloin, J. W. Tan, A. K. Gooch, and F. M. Inglis. 2009. AMPA glutamate receptor subunits 1 and 2 regulate dendrite complexity and spine motility in neurons of the developing neocortex. *Neuroscience* 159: 172-182.
4. Contractor, A., C. Mulle, and G. T. Swanson. 2011. Kainate receptors coming of age: Milestones of two decades of research. *Trends in Neuroscience* 34: 154-163.
5. Bowie, D. 2008. Ionotropic glutamate receptors & CNS disorders. *CNS & Neurological Disorders - Drug Targets* 7: 129-143.
6. Yuan, H., C. M. Low, O. A. Moody, A. Jenkins, and S. F. Traynelis. 2015. Ionotropic GABA and glutamate receptor mutations and human neurologic diseases. *Molecular Pharmacology* 88: 203-217.
7. Drejer, J., and T. Honore. 1988. New quinoxalinediones show potent antagonism of quisqualate responses in cultured mouse cortical neurons *Neuroscience Letters* 87: 104-108.
8. Ornstein, P. L., D. D. Schoepp, M. B. Arnold, N. K. Augenstein, D. Lodge, J. D. Millar, J. Chambers, J. Campbell, and J. W. Paschal. 1992. 6-substituted

decahydroisoquinoline-3-carboxylic acids as potent and selective conformationally constrained NMDA receptor antagonists. *Journal of Medical Chemistry* 35: 3547–3560.

9. Johansen, T. H., J. Drejer, F. Waitjen, and E. O. Nielsen. 1993. A novel non-NMDA receptor antagonist shows selective displacement of low-affinity [3H]kainate binding. *European Journal of Pharmacology* 246: 195-204.

10. Gill, M., S. Frausto, M. Ikoma, M. Sasaki, M. O. Sakai, and G. Swanson. 2010. A series of structurally novel heterotricyclic a-amino-3-hydroxyl-5-methyl-4-isoxazole-propionate receptor-selective antagonists. *British Journal of Pharmacology* 160: 1417–1429.

11. Solly, K., R. Klein, M. Rudd, M. K. Holloway, E. N. Johnson, D. Henze, and M. F. A. Finley. 2015. High-throughput screen of GluK1 receptor identifies selective inhibitors with a variety of kinetic profiles using fluorescence and electrophysiology assays. *Journal of Biomolecular Screening* 20: 708–719.

12. Zhang, Q., F. Guo, Z.-w. Fu, B. Zhang, C.-g. Huang, and Y. Li1. 2016. Timosaponin derivative yy-23 acts as a non-competitive NMDA receptor antagonist and exerts a rapid antidepressant-like effect in mice. *Acta Pharmacologica Sinica* 37: 166-176.

13. Jambrina, E., R. Cerne, E. Smith, L. Scampavia, M. Cuadrado, J. Findlay, M. J. Krambis, M. Wakulchik, P. Chase, M. Brunavs, K. D. Burris, P. Gallagher, T. P. Spicer, and D. Ursu. 2016. An integrated approach for screening and identification of positive allosteric modulators of n-methyl-d-aspartate receptors. *Journal of Biomolecular Screening* 21: 468–479.

14. Azumaya, C. M., E. L. Days, P. N. Vinson, S. Stauffer, G. Sulikowski, C. D. Weaver, and T. Nakagawa. 2017. Screening for AMPA receptor auxiliary subunit specific modulators. *PLoS One* 12: e0174742.

15. Guo, H., L. M. Camargo, F. Yeboah, M. E. Digan, H. Niu, Y. Pan, S. Reiling, G. Soler-Llavina, W. A. Weihofen, H.-R. Wang, Y. G. Shanker, T. Stams, and A. Bill. 2017. A NMDA-receptor calcium influx assay sensitive to stimulation by glutamate and glycine/d-serine. *Scientific Reports* 7.

16. Mercadante, S., E. Arcuri, W. Tirelli, and A. Casuccio. 2000. Analgesic effect of intravenous ketamine in cancer patients on morphine therapy. *Journal of Pain and Symptom Management* 20: 246-252.

17. Carlsson, K. C., N. O. Hoem, E. R. Moberg, and L. C. Mathisen. 2004. Analgesic effect of dextromethorphan in neuropathic pain. *Acta Anaesthesiologica Scandinavica* 48: 328-336.

18. Parsons, C. G., A. Stöffler, and W. Danysz. 2007. Memantine: A NMDA receptor antagonist that improves memory by restoration of homeostasis in the glutamatergic system - too little activation is bad, too much is even worse. *Neuropharmacology*: 699-723.

19. Swanson, G. T. 2009. Targeting AMPA and kainate receptors in neurological disease: Therapies on the horizon? *Neuropsychopharmacology* 34: 249–250.

20. Vanle, B., W. Olcott, J. Jimenez, L. Bashmi, I. Danovitch, and W. W. IsHak. 2018. NMDA antagonists for treating the non-motor symptoms in parkinson’s disease. *Translational Psychiatry* 8.

21. TrineKvist, J. R.Greenwood, K. B.Hansen, S. F.Traynelis, and HansBräuner-Osborne. 2013. Structure-based discovery of antagonists for GluN3-containing n-methyl-d-aspartate receptors. *Neuropharmacology* 75: 324-336.

22. Montfort, R. L. M. v., and P. Workman. 2017. Structure-based drug design: Aiming for a perfect fit. *Essays in Biochemistry* 61.

23. Wang, X., K. Song, L. Li, and L. Chen. 2018. Structure-based drug design strategies and challenges. *Topics in Medical Chemistry* 18.

24. Sobolevsky, A. I., M. P. Rosconi, and E. Gouaux. 2009. X-ray structure, symmetry and mechanism of an AMPA-subtype glutamate receptor. *Nature* 462: 745-756.

25. Schauder, D. M., O. Kuybeda, J. Zhang, K. Klymko, A. Bartesaghi, M. J. Borgnia, M. L. Mayer, and S. Subramaniam. 2013. Glutamate receptor desensitization is mediated by changes in quaternary structure of the ligand binding domain. *Proceedings of the National Academy of Sciences* 110: 5921-5926.

26. Meyerson, J. R., J. Kumar, S. Chittori, P. Rao, J. Pierson, A. Bartesaghi, M. L. Mayer, and S. Subramaniam. 2014. Structural mechanism of glutamate receptor activation and desensitization. *Nature* 514: 328-334.

27. Durr, K. L., L. Chen, R. A. Stein, R. De Zorzi, I. M. Folea, T. Walz, H. S. McHaourab, and E. Gouaux. 2014. Structure and dynamics of AMPA receptor GluA2 in resting, pre-open, and desensitized states. *Cell* 158: 778-792.

28. Yelshanskaya, M. V., M. Li, and A. I. Sobolevsky. 2014. Structure of an agonist-bound ionotropic glutamate receptor. *Science* 345: 1070-1074.

29. Meyerson, J. R., S. Chittori, A. Merk, P. Rao, T. H. Han, M. Serpe, M. L. Mayer, and S. Subramaniam. 2016. Structural basis of kainate subtype glutamate receptor desensitization. *Nature* 537: 567-571.

30. Chen, S., Y. Zhao, Y. Wang, M. Shekhar, E. Tajkhorshid, and E. Gouaux. 2017. Activation and desensitization mechanism of AMPA receptor-TARP complex by cryo-EM. *Cell* 170: 1234-1246 e1214.

31. Twomey, E. C., M. V. Yelshanskaya, R. A. Grassucci, J. Frank, and A. I. Sobolevsky. 2017. Channel opening and gating mechanism in AMPA-subtype glutamate receptors. *Nature* 549: 60-65.

32. Twomey, E. C., M. V. Yelshanskaya, R. A. Grassucci, J. Frank, and A. I. Sobolevsky. 2017. Structural bases of desensitization in AMPA receptor-auxiliary subunit complexes. *Neuron* 94: 569-580 e565.

33. Yelshanskaya, M. V., K. Saotome, and A. I. Sobolevsky. 2016. Probing intersubunit interfaces in AMPA-subtype ionotropic glutamate receptors. *Scientific Reports* 6.

34. Mayer, M. L. 2017. The challenge of interpreting glutamate-receptor ion-channel structures. *Biophysical Journal* 113: 2143–2151.

35. Shinozaki, H., and I. Shibuya. 1974. Potentiation of glutamate-induced depolarization by kainic acid in the crayfish opener muscle. *Neuropharmacology* 10: 1057-1065.

36. Turski, W., and L. T. S. J. C. Z. Kleinrok. 1981. (rs)-alpha-amino-3-hydroxy-5-methyl-4-isoxazolepropionic acid: Wet dog shakes, catalepsy and body temperature changes in rats. *Pharmacology Biochemistry and Behavior* 15: 545-549.

37. Foster, A. C., and G. E. Fagg. 1984. Acidic amino acid binding sites in mammalian neuronal membranes: Their characteristics and relationship to synaptic receptors. *Brain Research* 319: 103-164.

38. Chittajallu, R., M. Vignes, K. K. Dev, J. M. Barnes, G. L. Collingridge, and J. M. Henley. 1996. Regulation of glutamate release by presynaptic kainate receptors in the hippocampus. *379*: 78-81.

39. Castillo, P. E., R. C. Malenka, and R. A. Nicoll. 1997. Kainate receptors mediate a slow postsynaptic current in hippocampal CA3 neurons. *Nature* 388: 182-186.

40. Vignes, M., and G. L. Collingridge. 1997. The synaptic activation of kainate receptors. *Nature* 388: 179-182.

41. Frerking, M., R. C. Malenka, and R. A. Nicoll. 1998. Synaptic activation of kainate receptors on hippocampal interneurons. *Nature Neuroscience* 1: 479–486.

42. DeVries, S. H., and E. A. Schwartz. 1999. Kainate receptors mediate synaptic transmission between cones and 'off' bipolar cells in a mammalian retina. *Nature* 397: 157-160.

43. Li, P., T. J. Wilding, S. J. Kim, A. A. Calejesan, J. E. Huettner, and M. Zhuo. 1999. Kainate-receptor-mediated sensory synaptic transmission in mammalian spinal cord. *Nature* 397: 161-164.

44. H, L., and R. MA. 1998. GluR5 kainate receptor mediated synaptic transmission in rat basolateral amygdala in vitro. *Neuropharmacology* 37: 1279-1286.

45. Kidd, F. L., and J. T. R. Isaac. 1999. Developmental and activity-dependent regulation of kainate receptors at thalamocortical synapses. *Nature* 400: 569–573.

46. Campbell, S. L., S. S. Mathew, and J. J. Hablitz. 2007. Pre- and postsynaptic effects of kainate on layer ii/iii pyramidal cells in rat neocortex. *Neuropharmacology* 53: 37-47.

47. Delaney, A. J., and C. E. Jahr. 2002. Kainate receptors differentially regulate release at two parallel fiber synapses. *Neuron*: 475-482.

48. Clarke, V. R. J., B. A. Ballyk, K. H. Hoo, A. Mandelzys, A. Pellizzari, C. P. Bath, J. Thomas, E. F. Sharpe, C. H. Davies, P. L. Ornstein, D. D. Schoepp, R. K. Kamboj, G. L. Collingridge, D. Lodge, and D. Bleakman. 1997. A hippocampal GluR5 kainate receptor regulating inhibitory synaptic transmission. *Nature*: 599–603.

49. Cossart, R., R. Tyzio, C. Dinocourt, M. Esclapez, J. CHirsch, Y. Ben-Ari, and C. Bernard. 2001. Presynaptic kainate receptors that enhance the release of GABA on CA1 hippocampal interneurons. *Neuron*: 497-508.

50. Rodríguez-Moreno, A., and J. Lerma. 1998. Kainate receptor modulation of GABA release involves a metabotropic function. *Neuron* 20: 1211-1218.

51. Barbon, A., and S. Barlati. 2011. Glutamate receptor RNA editing in health and disease. *Biochemistry* 76: 882.

52. Jaskolski, F., F. Coussen, N. Nagarajan, E. Normand, C. Rosenmund, and C. Mulle. 2004. Subunit composition and alternative splicing regulate membrane delivery of kainate receptors. *Journal of Neuroscience* 24: 2506-2515.

53. Traynelis, S. F., and P. Wahl. 1997. Control of rat GluR6 glutamate receptor open probability by protein kinase a and calcineurin. *Journal of Physiology* 503: 513-531.

54. Kornreich, B. G., L. Niu, M. S. Roberson, and R. E. Oswald. 2009. Identification of c-terminal domain residues involved in protein kinase a-mediated potentiation of GluR6. *Journal of Neuroscience* 146: 1158–1168.

55. Rojas, A., P. Gueorguieva, N. Lelutiu, Y. Quan, R. Shaw, and R. Dingledine. 2014. The prostaglandin ep1 receptor potentiates kainate receptor activation via a protein kinase c pathway and exacerbates status epilepticus. *Neurobiology of Disease* 70: 74-89.

56. Vignes, M., C. Mathiesen, and G. L. Collingridge. 1996. Activation of a kainate-induced inward current in CA3 hippocampal neurons of immature rats in vitro. *Journal of Physiology*.

57. Mulle, C., A. Sailer, I. P. rez-Otan, H. Dickinson-Anson, P. E. Castillo, I. Bureau, C. Maron, F. H. Gage, J. R. Mann, B. Bettler, and S. F. Heinemann. 1998. Altered synaptic physiology and reduced susceptibility to kainate-induced seizures in GluR6-deficient mice. *Nature* 392: 601-605.

58. Fernandes, H. B., J. S. Catches, R. S. Petralia, B. A. Copits, J. Xu, T. A. Russell, G. T. Swanson, and A. Contractor. 2009. High affinity kainate receptor subunits are necessary for ionotropic but not metabotropic signaling. *Neuron* 63: 818–829.

59. Dong, Z., B. Gong, H. Li, Y. Bai, X. Wu, Y. Huang, W. He, T. Li, and Y. T. Wang. 2012. Mechanisms of hippocampal long-term depression are required for memory enhancement by novelty exploration. *Journal of Neuroscience* 32: 11980-11990.

60. Nicoll, R. A. 2017. A brief history of long-term potentiation. *Neuron* 93: 281-290.

61. Lauri, S. E., Z. A. Bortolotto, D. Bleakman, D. Lodge, J. T. R. Isaac, and G. L. Collingridge. 2001. A critical role of a facilitatory presynaptic kainate receptor in mossy fiber LTP. *Neuron* 32: 697-709.

62. Park, Y., J. Jo, J. T. R. Isaac, and K. Cho. 2006. Long-term depression of kainate receptor-mediated synaptic transmission. *Neuron* 49: 95-106.

63. Shi, T.-Y., S.-F. Feng, M.-X. Wei, Y. Huang, G. Liu, Hai-TaoWu, Y.-X. Zhang, and W.-X. Zhou. 2018. Kainate receptor mediated presynaptic LTP in agranular insular cortex contributes to fear and anxiety in mice. *Neuropharmacology* 128: 388-400.

64. Ko, S., M.-G. Zhao, H. Toyoda, C.-S. Qiu, and M. Zhuo. 2005. Altered behavioral responses to noxious stimuli and fear in glutamate receptor 5 (GluR5)- or GluR6-deficient mice. *The Journal of Neuroscience* 25: 977-984.

65. Wu, L.-J., S. W. Ko, H. Toyoda, M.-G. Zhao, H. Xu, K. I. Vadakkan, M. Ren, E. Knifed, F. Shum, J. Quan, X.-H. Zhang, and M. Zhuo. 2007. Increased anxiety-like behavior and enhanced synaptic efficacy in the amygdala of GluR5 knockout mice. *PLoS One* 2.

66. Shaltiel, G., S. Maeng, O. Malkesman, B. Pearson, R. Schloesser, T. Tragon, M. Rogawski, M. Gasior, D. Luckenbaugh, G. Chen, and H. Manji. 2008. Evidence for the involvement of the kainate receptor subunit GluR6 (GriK2) in mediating behavioral displays related to behavioral symptoms of mania. *Molecular Psychiatry* 13: 858–872.

67. Catches, J. S., J. Xu, and A. Contractor. 2012. Genetic ablation of the GluK4 kainate receptor subunit causes anxiolytic and antidepressant-like behavior in mice. *Behavioral Brain Research* 228: 406-414.

68. Lowry, E. R., A. Kruyer, E. H. Norris, C. R. Cederroth, and S. Stricklanda. 2013. The GluK4 kainate receptor subunit regulates memory, mood, and excitotoxic neurodegeneration. *Neuroscience* 235: 215-235.

69. Micheau, J., A. Vimeney, E. Normand, C. Mulle, and G. Riedel. 2014. Impaired hippocampus-dependent spatial flexibility and sociability represent autism-like phenotypes in GluK2 mice. *Hippocampus* 24: 1059-1069.

70. Xu, J., J. J. Marshall, H. B. Fernandes, T. Nomura, B. A. Copits, D. Procissi, S. Mori, L. Wang, Y. Zhu, G. T. Swanson, and A. Contractor. 2017. Complete disruption of

the kainate receptor gene family results in corticostriatal dysfunction in mice. *Cell Reports* 18: 1848–1857.

71. Zhuo, M. 2017. Cortical kainate receptors and behavioral anxiety. *10* 16.

72. Guzmán, Y. F., K. Ramsey, J. R. Stolz, D. W. Craig, M. J. Huentelman, V. Narayanan, and G. T. Swanson. 2017. A gain-of-function mutation in the GriK2 gene causes neurodevelopmental deficits. *Neurology Genetics* 3: e129.

73. Paternain, A. V., M. Morales, and J. Lerma. 1995. Selective antagonism of AMPA receptors unmasks kainate receptor-mediated responses in hippocampal neurons. *Neuron* 14: 185-189.

74. Paternain, A. V., A. Rodrı´guez-Moreno, A. Villarroel, and J. Lerma. 1998. Activation and desensitization properties of native and recombinant kainate receptors. *Neuropharmacology*: 1249–1259.

75. Kornau, H., L. Schenker, M. Kennedy, and P. Seeburg. 1995. Domain interaction between NMDA receptor subunits and the postsynaptic density protein PSD-95. *Science* 269: 1737-1740.

76. Liu, S.-H., H.-H. Cheng, S.-Y. Huang, P.-C. Yiu, and Y.-C. Chang. 2006. Studying the protein organization of the postsynaptic density by a novel solid phase- and chemical cross-linking-based technology. *Molecular & Cellular Proteomics* 5.

77. Zhang, W., F. St-Gelais, C. P. Grabner, J. C. Trinidad, A. Sumioka, M. Morimoto-Tomita, K. S. Kim, C. Straub, A. L. Burlingame, J. R. Howe, and S. Tomita. 2009. A transmembrane accessory subunit that modulates kainatetype glutamate receptors. *Neuron* 61: 385–396.

78. Copits, B. A., and G. T. Swanson. 2012. Dancing partners at the synapse: Auxiliary subunits that shape kainate receptor function. *Nat Rev Neurosci* 13: 675-686.

79. Eibl, C., and A. J. Plested. 2018. AMPA receptors: Mechanisms of auxiliary protein action. *Current Opinion in Physiology* 2: 84-91.

80. Ng, D., G. M. Pitcher, R. K. Szilard, A. Sertié, M. Kanisek, S. J. Clapcote, T. Lipina, L. V. Kalia, D. Joo, C. McKerlie, M. Cortez, J. C. Roder, M. W. Salter, and R. R. McInnes. 2009. Neto1 is a novel CUB-domain NMDA receptor–interacting protein required for synaptic plasticity and learning. *PLoS Biology* 7.

81. Tang, M., K. A. Pelkey, D. Ng, E. Ivakine, C. J. McBain, M. W. Salter, and R. R. McInnes. 2011. The CUB domain protein Neto1 is an auxiliary protein of native synaptic kainate receptors. *Journal of Neuroscience* 31: 10009–10018.

82. Straub, C., W. Zhang, and J. R. Howe. 2011. Neto2 modulation of kainate receptors with different subunit compositions. *The Journal of Neuroscience* 31: 8078 – 8082.

83. Tomita, S., and P. E. Castillo. 2012. Neto1 and Neto2: Auxiliary subunits that determine key properties of native kainate receptors. *The Journal of Physiology* 590: 2217–2223.

84. Fisher, J. L. 2015. The auxiliary subunits neto1 and neto2 have distinct, subunitdependent effects at recombinant GluK1- and GluK2-containing kainate receptors. *Neuropharmacology*: 471–480.

85. Fisher, J. L., and D. D. Mott. 2012. The auxiliary subunits Neto1 and Neto2 reduce voltage-dependent inhibition of recombinant kainate receptors. *The Journal of Neuroscience* 32: 12928 –12933.

86. Sheng, N., Y. S. Shi, R. M. Lomash, K. W. Roche, and R. A. Nicoll. 2015. Neto auxiliary proteins control both the trafficking and biophysical properties of the kainate receptor GluK1. *eLife*.

87. Bork, P., and G. Beckmann. 1993. The CUB domain: A widespread module in developmentally regulated proteins. *Journal of Molecular Biology* 2: 539-545.

88. Gu, C., B. J. Limberg, G. B. Whitaker, B. Perman, D. J. Leahy, J. S. Rosenbaum, D. D. Ginty, and A. L. Kolodkin. 2002. Characterization of Neuropilin-1 structural features that confer binding to Semaphorin 3a and Vascular Endothelial Growth Factor 165. *The Journal of Biological Chemistry* 277: 18069–18076.

89. Rudenko, G., L. Henry, K. Henderson, K. Ichtchenko, M. S. Brown, J. L. Goldstein, and J. Deisenhofer. 2002. Structure of the LDL receptor extracellular domain at endosomal pH. *Science* 298: 2353-2358.

90. Blanc, G., B. Font, D. Eichenberger, C. Moreau, S. Ricard-Blum, D. J. S. Hulmes, and C. Moali. 2007. Insights into how CUB domains can exert specific functions while sharing a common fold. *The Journal of Biological Chemistry* 282: 16924–16933.

91. Appleton, B. A., P. Wu, J. Maloney, J. Yin, W.-C. Liang, S. Stawicki, K. Mortara, K. K. Bowman, J. M. Elliott, W. Desmarais, J. F. Bazan, A. Bagri, M. Tessier-Lavigne, A. W. Koch, Y. Wu, R. J. Watts, and C. Wiesmann. 2007. Structural studies of Neuropilin/antibody complexes provide insights into Semaphorin and VEGF binding. *The EMBO Journal*: 4902–4912.

92. Kwon, H. J., T. A. Lagace, M. C. McNutt, J. D. Horton, and J. Deisenhofer. 2008. Molecular basis for LDL receptor recognition by PCSK9. *PNAS* 105: 1820-1825.

93. Nogi, T., N. Yasui, E. Mihara, Y. Matsunaga, M. Noda, N. Yamashita, T. Toyofuku, S. Uchiyama, Y. Goshima, A. Kumanogoh, and J. Takagi1. 2010. Structural basis for Semaphorin signalling through the Plexin receptor. *Nature* 467: 1123-1127.

94. Gaboriaud, C., L. Gregory-Pauron, F. Teillet, N. M. Thielens, I. Bally, and G. r. J. Arlaud. 2011. Structure and properties of the Ca2 + -binding CUB domain, a

widespread ligand-recognition unit involved in major biological functions. *Biochemical Journal*: 185–193.

95. Janssen, B. J. C., T. Malinauskas, G. A. Weir, M. Z. Cader, C. Siebold, and E. Y. Jones. 2012. Neuropilins lock secreted semaphorins onto plexins in a ternary signaling complex. *Nature Structural & Molecular Biology* 19: 1293-1299.

96. Parker, M. W., A. D. Linkugel, H. L. Goel, T. Wu, A. M. Mercurio, and C. W. V. Kooi. 2015. Structural basis for VEGF-c binding to Neuropilin-2 and sequestration by a soluble splice form. *Cell Structure*: 677–687.

97. Nikolic, J., L. Belot, H. Raux, P. Legrand, Y. Gaudin, and A. A. Albertini. 2018. Structural basis for the recognition of LDL-receptor family members by VSV glycoprotein. *Nature Communications* 9.

98. Zhao, Y., S. Chen, C. Yoshioka, I. Baconguis, and E. Gouaux. 2016. Architecture of fully occupied GluA2 AMPA receptor – TARP complex elucidated by cryo-EM. *Nature* 536: 108–111.

99. Herguedas, B., J. F. Watson, H. Ho, O. Cais, J. García-Nafría, and I. H. Greger. 2019. Architecture of the heteromeric GluA1/2 AMPA receptor in complex with the auxiliary subunit TARP γ8. *Science*.

100. Paoletti, P., P. Ascher, and J. Neyton. 1997. High-affinity zinc inhibition of NMDA NR1–NR2a receptors. *Journal of Neuroscience* 17.

101. Rassendren, F.-A., P. Lory, J.-P. Pin, and J. Nargeot. 1990. Zinc has opposite effects on NMDA and non-NMDA receptors expressed in Xenopus oocytes. *Neuron* 4: 733-740.

102. Hoo, K. H., S. L. Nutt, E. J. Fletcher, C. E. Elliott, B. Korczak, R. M. Deverill, V. Rampersad, R. P. Fantaske, and R. K. Kamboj. 1994. Functional expression and

pharmacological characterization of the human EAA4 (GluR6) glutamate receptor: A kainate selective channel subunit. *Receptors and channels* 2: 327-337.

103. Dreixler, J. C., and J. P. Leonard. 1997. Effects of external calcium on zinc modulation of AMPA receptors. *Brain research* 1: 170-174.

104. Shen, Y., and X.-L. Yang. 1999. Zinc modulation of AMPA receptors may be relevant to splice variants in Carp retina. *Neuroscience Letters*: 177-180.

105. Dao-Qi Zhang, C. R., Stuart C. Mangel, and Douglas G. McMahon. 2002. Suppression by zinc of AMPA receptor-mediated synaptic transmission in the retina. *Journal of Neurophysiology* 88: 1245-1251.

106. Fukushima, T., R. Shingai, T. Ogurusu, and M. Ichinose. 2003. Inhibition of willardiine-induced currents through rat GluR6/KA-2 kainate receptor channels by zinc and other divalent cations. *Neuroscience Letters* 2: 107-110.

107. Blakemore, L., and P. Trombley. 2004. Diverse modulation of olfactory bulb AMPA receptors by zinc. *NeuroReport* 15: 919-923.

108. Mott, D. D., M. Benveniste, and R. J. Dingledine. 2008. pH-dependent inhibition of kainate receptors by zinc. *Journal of Neuroscience* 28: 1659-1671.

109. Kreitzer, M. A., A. D. Birnbaum, H. Qian, and R. P. Malchow. 2009. Pharmacological characterization, localization, and regulation of ionotropic glutamate receptors in skate horizontal cells. *Visual Neuroscience* 26: 375-387.

110. Bowie, D. 2002. External anions and cations distinguish between AMPA and kainate receptor gating mechanisms. *Journal of Physiology* 539: 725-733.

111. Wong, A. Y. C. 2006. External ions are coactivators of kainate receptors. *Journal of Neuroscience* 26: 5750-5755.

112. Wong, A. Y., D. M. MacLean, and D. Bowie. 2007. Na+/Cl- dipole couples agonist binding to kainate receptor activation. *Journal of Neuroscience* 27: 6800-6809.

113. Plested, A. J., R. Vijayan, P. C. Biggin, and M. L. Mayer. 2008. Molecular basis of kainate receptor modulation by sodium. *Neuron* 58: 720-735.

114. Maclean, D. M., A. Y. Wong, A. M. Fay, and D. Bowie. 2011. Cations but not anions regulate the responsiveness of kainate receptors. *Journal of Neuroscience* 31: 2136-2144.

115. Plested, A. J. R. 2011. Kainate receptor modulation by sodium and chloride. In *Advances in experimental medicine and biology*, Boston, MA. 93-113.

116. Paternain, A. V., A. Cohen, Y. Stern-Bach, and J. Lerma. 2003. A role for extracellular Na in the channel gating of native and recombinant kainate receptors. *The Journal of Neuroscience* 23: 8641– 8648.

117. Dawe, G. B., M. Musgaard, E. D. Andrews, B. A. Daniels, M. R. Aurousseau, P. C. Biggin, and D. Bowie. 2013. Defining the structural relationship between kainate-receptor deactivation and desensitization. *Nature Structural & Molecular Biology* 20: 1054-1061.

118. Griffith, T. N., and G. T. Swanson. 2015. Identification of critical functional determinants of kainate receptor modulation by auxiliary protein Neto2. *The Journal of Physiology* 593: 4815–4833.

119. Attwell, D., and J. F. Iles. 1979. Synaptic transmission: Ion concentration changes in the synaptic cleft. *Proceedings of the Royal Society B* 206: 115-131.

120. Ma, W., A. Korngreen, N. Uzlaner, Z. Priel, and S. D. Silberberg. 1999. Extracellular sodium regulates airway ciliary motility by inhibiting a P2x receptor. *Nature* 400: 894–897.

121. Kaczmarek, L. K. 2013. Slack, slick, and sodium-activated potassium channels. *ISRN Neuroscience* 2013.

122. Jara-Oseguera, A., C. Bae, and K. J. Swartz. 2016. An external sodium ion binding site controls allosteric gating in Trpv1 channels. *Elife* 5: e13356.

123. Kanellopoulos, A. H., J. Zhao, E. C. Emery, and J. N. Wood. 2017. Intracellular sodium regulates opioid signalling in peripheral neurons. *bioRxiv* 117952.

124. Reiner, A., R. J. Arant, and E. Y. Isacoff. 2012. Assembly stoichiometry of the GluK2/GluK5 kainate receptor complex. *Cell Rep* 1: 234–240.

125. Kumar, J., P. Schuck, and M. L. Mayer. 2011. Structure and assembly mechanism for heteromeric kainate receptors. *Neuron* 71: 319–331.

126. Furukawa, H. 2011. Structure and function of glutamate receptor amino terminal domains. *Journal of Physiology* 590: 63-72.

127. Kumar, J., P. Schuck, R. Jin, and M. L. Mayer. 2009. The n-terminal domain of GluR6-subtype glutamate receptor ion channels. *Nature Structural & Molecular Biology* 16: 631–638.

128. Kumar, J., and M. L. Mayer. 2010. Crystal structures of the glutamate receptor ion channel GluK3 and GluK5 amino-terminal domains. *Journal of Molecular Biology* 404: 680-696.

129. Zhao, H., S. Lomash, S. Chittori, C. Glasser, M. L. Mayer, and P. Schuck. 2017. Preferential assembly of heteromeric kainate and AMPA receptor amino terminal domains. *eLife* 6.

130. Pasternack, A., S. K. Coleman, A. Jouppila, D. G. Mottershead, M. Lindfors, M. Pasternack, and K. Keinänen. 2002. A-amino-3-hydroxy-5-methyl-4-

isoxazolepropionic acid (AMPA) receptor channels lacking the n-terminal domain. *Journal of Biological Chemistry* 277: 49662-49667.

131. Plested, A. J. R., and M. L. Mayer. 2007. Structure and mechanism of kainate receptor modulation by anions. *Neuron* 53: 829-841.

132. Sheng, N., Y. S. Shi, and R. A. Nicoll. 2017. Amino-terminal domains of kainate receptors determine the differential dependence on Neto auxiliary subunits for trafficking. *Proceedings of the National Academy of Sciences* 114: 1159-1164.

133. Duan, G.-F., S. X. Yaxin Ye, W. Tao, S. Zhao, T. Jin, R. A. Nicoll, Y. S. Shi, and N. Sheng. 2018. Signal peptide represses GluK1 surface and synaptic trafficking through binding to amino-terminal domain. *Nature Communications* 9.

134. Shaikh, S. A., D. M. Dolino, G. Lee, S. Chatterjee, D. M. MacLean, C. Flatebo, C. F. Landes, and V. Jayaraman. 2016. Stargazin modulation of AMPA receptors. *Cell Reports* 17: 328-335.

135. Nanao, M. H., T. Green, Y. Stern-Bach, S. F. Heinemann, and S. Choe. 2005. Structure of the kainate receptor subunit GluR6 agonist-binding domain complexed with domoic acid. *Proceedings of the National Academy of Sciences* 102: 1708-1713.

136. Unno, M., M. Shinohara, K. Takayama, H. Tanaka, K. Teruya, K. Doh-ura, R. Sakai, M. Sasaki, and M. Ikeda-Saito. 2011. Binding and selectivity of the marine toxin neodysiherbaine a and its synthetic analogues to GluK1 and GluK2 kainate receptors. *Journal of Molecular Biology* 413: 667-683.

137. Venskutony, R., K. Frydenvanga, H. Haldab, A. C. d. Rabassaa, M. Gajhedea, P. K. Ahring, and J. S. Kastrupa. 2012. Kainate induces various domain closures in AMPA and kainate receptors. *Neurochemistry International* 61: 536-545.

138. Juknaitė, L., R. Venskutonytė, Z. Assaf, S. Faure, T. Gefflaut, D. J. Aitken, B. Nielsen, M. Gajhede, J. S. Kastrup, L. Bunch, K. Frydenvang, and D. S. Pickering. 2012. Pharmacological and structural characterization of conformationally restricted (s)-glutamate analogues at ionotropic glutamate receptors. *Journal of Structural Biology* 180: 39-46.

139. Assaf, Z., A. P. Larsen, R. Venskutonytė, L. Han, B. Abrahamsen, B. Nielsen, M. Gajhede, J. S. Kastrup, A. A. Jensen, D. S. Pickering, K. Frydenvang, T. Gefflaut, and L. Bunch. 2013. Chemoenzymatic synthesis of new 2,4-syn-functionalized (s)-glutamate analogues and structure–activity relationship studies at ionotropic glutamate receptors and excitatory amino acid transporters. *Journal of Medical Chemistry* 56: 1614–1628.

140. Møllerud, S., A. Pinto, L. Marconi, K. Frydenvang, T. S. Thorsen, S. Laulumaa, R. Venskutonytė, S. Winther, A. M. C. Moral, L. Tamborini, P. Conti, D. S. Pickering, and J. S. Kastrup. 2017. Structure and affinity of two bicyclic glutamate analogues at AMPA and kainate receptors. *ACS Chemical Neuroscience* 8: 2056–2064.

141. Du, M., A. Rambhadran, and V. Jayaraman. 2008. Luminescence resonance energy transfer investigation of conformational changes in the ligand binding domain of a kainate receptor. *Journal of Biological Chemistry* 283: 27074-27078.

142. Musgaard, M., and P. C. Biggin. 2016. Steered molecular dynamics simulations predict conformational stability of glutamate receptors. *Journal of Chemical Information and Modeling* 56: 1787-1797.

143. Zhang, Y., N. Nayeem, M. H. Nanao, and T. Green. 2006. Interface interactions modulating desensitization of the kainate-selective ionotropic glutamate receptor subunit GluR6. *Journal of Neuroscience* 26: 10033-10042.

144. Nayeem, N., Y. Zhang, D. K. Schweppe, D. R. Madden, and T. Green. 2009. A nondesensitizing kainate receptor point mutant. *Molecular Pharmacology* 76: 534-542.

145. Wo, Z. G., and R. E. Oswald. 1994. Transmembrane topology of two kainate receptor subunits revealed by n-glycosylation. *Proceedings of the National Academy of Sciences* 91: 7154-7158.

146. Wo, Z. G., and R. E. Oswald. 1995. A topological analysis of goldfish kainate receptors predicts three transmembrane segments. *Journal of Biological Chemistry* 270: 2000-2009.

147. Bernard, A., L. Ferhat, F. Dessi, G. Charton, A. Represa, Y. Ben-Ari, and M. Khrestchatisky. 2008. Q/r editing of the rat GluR5 and GluR6 kainate receptors in vivo and in vitro: Evidence for independent developmental, pathological and cellular regulation. *European Journal of Neuroscience* 11: 604-616.

148. Nasu-Nishimura, Y., D. Hurtado, S. Braud, T. T.-T. Tang, J. T. R. Isaac, and K. W. Roche. 2006. Identification of an endoplasmic reticulum-retention motif in an intracellular loop of the kainate receptor subunit KA2. *Journal of Neuroscience* 26: 7014 –7021.

149. Amin, J. B., C. L. Salussolia, K. Chan, M. C. Regan, J. Dai, H.-X. Zhou, H. Furukawa, M. E. Bowen, and L. P. Wollmuth. 2017. Divergent roles of a peripheral transmembrane segment in AMPA and NMDA receptors. *Journal of General Physiology* 149: 661–680.

150. Yan, S., J. M. Sanders, J. Xu, Y. Zhu, A. Contractor, and G. T. Swanson. 2004. A c-terminal determinant of GluR6 kainate receptor trafficking. *Journal of Neuroscience* 24: 679-691.

151. Ren, Z., N. J. Riley, E. P. Garcia, J. M. Sanders, G. T. Swanson, and J. Marshall. 2003. Multiple trafficking signals regulate kainate receptor KA2 subunit surface expression. *Journal of Neuroscience* 23.

152. Copits, B. A., and G. T. Swanson. 2013. Kainate receptor post-translational modifications differentially regulate association with 4.1n to control activity-dependent receptor endocytosis. *Journal of Biological Chemistry* 288: 8952-8965.

153. Martin, S., A. Nishimune, J. R. Mellor, and J. M. Henley. 2012. Sumoylation regulates kainate-receptor-mediated synaptic transmission. *Nature* 447: 321–325.

154. Zhu, Q.-J., F.-S. Kong, H. Xu, Y. Wang, C.-P. Du, C.-C. Sun, Y. Liu, Ting Li, and X.-Y. Hou. 2014. Tyrosine phosphorylation of GluK2 up-regulates kainate receptor-mediated responses and downstream signaling after brain ischemia. *Proceedings of the National Academy of Sciences* 111: 13990-13995.

155. MacLean, D. M., S. S. Ramaswamy, M. Du, J. R. Howe, and V. Jayaraman. 2014. Stargazin promotes closure of the AMPA receptor ligand-binding domain. *Journal of General Physiology* 144: 503-512.

156. Sirrieh, R. E., D. M. MacLean, and V. Jayaraman. 2015. A conserved structural mechanism of NMDA receptor inhibition: A comparison of ifenprodil and zinc. *Journal of General Physiology* 146: 173-181.

157. Ramaswamy, S., D. Cooper, N. Poddar, D. M. MacLean, A. Rambhadran, J. N. Taylor, H. Uhm, C. F. Landes, and V. Jayaraman. 2012. Role of conformational dynamics in alpha-amino-3-hydroxy-5-methylisoxazole-4-propionic acid (AMPA) receptor partial agonism. *Journal of Biological Chemistry* 287: 43557-43564.

158. Dolino, D. M., S. Chatterjee, D. M. MacLean, C. Flatebo, L. D. C. Bishop, S. A. Shaikh, C. F. Landes, and V. Jayaraman. 2017. The structure-energy landscape of NMDA receptor gating. *Nature Chemical Biology* 13: 1232-1238.

159. Bal, M., O. Zaika, P. Martin, and M. S. Shapiro. 2008. Calmodulin binding to m-type K+ channels assayed by TIRF/FRET in living cells. *Journal of Physiology* 586: 2307–2320.

160. Landes, C. F., A. Rambhadran, J. N. Taylor, F. Salatan, and V. Jayaraman. 2011. Structural landscape of isolated agonist-binding domains from single AMPA receptors. *Nature Chemical Biology* 7: 168-173.

161. McLoughlin, S. Y., M. Kastantin, D. K. Schwartz, and J. L. Kaar. 2013. Single-molecule resolution of protein structure and interfacial dynamics on biomaterial surfaces. *Proceedings of the National Academy of Sciences USA* 110: 19396–19401.

162. Wang, Y., Y. Liu, H. A. DeBerg, T. Nomura, M. T. Hoffman, P. R. Rohde, K. Schulten, B. Martinac, and P. R. Selvin. 2014. Single molecule FRET reveals pore size and opening mechanism of a mechano-sensitive ion channel. *eLife* 3: e01834.

163. Gouridis, G., G. K. Schuurman-Wolters, E. Ploetz, F. Husada, R. Vietrov, M. d. Boer, T. Cordes, and B. Poolman. 2015. Conformational dynamics in substrate-binding domains influences transport in the ABC importer Glnpq. *Nature Structural & Molecular Biology* 22: 57–64.

164. Cooper, D. R., D. M. Dolino, H. Jaurich, B. Shuang, S. Ramaswamy, C. E. Nurik, J. Chen, V. Jayaraman, and C. F. Landes. 2015. Conformational transitions in the glycine-bound GluN1 NMDA receptor LBD via single-molecule FRET. *Biophys J* 109: 66-75.

165. Kim, J.-Y., C. Kim, and N. K. Lee. 2015. Real-time submillisecond single-molecule FRET dynamics of freely diffusing molecules with liposome tethering. *Nature Communications* 6: 6992.

166. Song, C.-X., J. Diao, A. T. Brunger, and S. R. Quake. 2016. Simultaneous single-molecule epigenetic imaging of DNA methylation and hydroxymethylation. *Proceedings of the National Academy of Sciences USA* 113: 4338–4343.

167. Stockmar, F., A. Y. Kobitski, and G. U. Nienhaus. 2016. Fast folding dynamics of an intermediate state in RNase H measured by single-molecule FRET. *Journal of Physical Chemistry B* 120: 641-649.

168. Wang, S., R. Vafabakhsh, W. F. Borschel, T. Ha, and C. G. Nichols. 2016. Structural dynamics of potassium channel gating revealed by single molecule FRET. *Nature Structural and Molecular Biology* 23: 31-36.

169. Baker, K. A., R. Lamichhane, T. Lamichhane, D. Rueda, and P. R. Cunningham. 2016. Protein–RNA dynamics in the central junction control 30s ribosome assembly. *Journal of Molecular Biology* 428: 3615-3631.

170. Dolino, D. M., S. Rezaei Adariani, S. A. Shaikh, V. Jayaraman, and H. Sanabria. 2016. Conformational selection and submillisecond dynamics of the ligand-binding domain of the n-methyl-d-aspartate receptor. *Journal of Biological Chemistry* 291: 16175-16185.

171. Gomes, G.-N., and C. C. Gradinaru. 2017. Insights into the conformations and dynamics of intrinsically disordered proteins using single-molecule fluorescence. *Biochimica et Biophysica Acta* 1865: 1696-1706.

172. Kempe, D., M. Cerminara, S. Poblete, A. Schöne, M. Gabba, and J. Fitter. 2017. Single-molecule FRET measurements in additive-enriched aqueous solutions. *Analytical Chemistry* 89: 694–702.

173. Martinac, B. 2017. Single-molecule FRET studies of ion channels. *Progress in Biophysics and Molecular Biology* 130: 192-197.

174. Warhaut, S., K. R. Mertinkus, P. Höllthaler, B. Fürtig, M. Heilemann, M. Hengesbach, and H. Schwalbe. 2017. Ligand-modulated folding of the full-length adenine riboswitch probed by NMR and single-molecule FRET spectroscopy. *Nucleic Acids Research* 45: 5512-5522.

175. Roy, R., S. Hohng, and T. Ha. 2008. A practical guide to single-molecule FRET. *Nature Methods* 5: 507-516.

176. Sisamakis, E., A. Valeri, S. Kalinin, P. J. Rothwell, and C. A. M. Seidel. 2010. Accurate single-molecule FRET studies using multiparameter fluorescence detection. *Methods in Enzymology* 475: 455-513.

177. Ye, S., C. Köhrer, T. Huber, M. Kazmi, P. Sachdev, E. C. Y. Yan, A. Bhagat, U. L. RajBhandary, and T. P. Sakmar. 2008. Site-specific incorporation of keto amino acids into functional G protein-coupled receptors using unnatural amino acid mutagenesis. *Journal of Biological Chemistry* 283: 1525-1533.

178. Dolino, D. M., D. Cooper, S. Ramaswamy, H. Jaurich, C. F. Landes, and V. Jayaraman. 2015. Structural dynamics of the glycine-binding domain of the n-methyl-d-aspartate receptor. *Journal of Biological Chemistry* 290: 797-804.

179. McKinney, S. A., C. Joo, and T. Ha. 2006. Analysis of single-molecule FRET trajectories using hidden Markov modeling. *Biophysical Journal* 91: 1941–1951.

180. Shuang, B., D. Cooper, J. N. Taylor, L. Kisley, J. Chen, W. Wang, C. B. Li, T. Komatsuzaki, and C. F. Landes. 2014. Fast step transition and state identification (STASI) for discrete single-molecule data analysis. *Journal of Physical Chemistry Letters* 5: 3157-3161.

181. Lee, C. H., W. Lu, J. C. Michel, A. Goehring, J. Du, X. Song, and E. Gouaux. 2014. NMDA receptor structures reveal subunit arrangement and pore architecture. *Nature* 511: 191-197.

182. Zhu, S., R. A. Stein, C. Yoshioka, C. H. Lee, A. Goehring, H. S. McHaourab, and E. Gouaux. 2016. Mechanism of NMDA receptor inhibition and activation. *Cell* 165: 704-714.

183. Yelshanskaya, M. V., A. K. Singh, J. M. Sampson, C. Narangoda, M. Kurnikova, and A. I. Sobolevsky. 2016. Structural bases of noncompetitive inhibition of AMPA-subtype ionotropic glutamate receptors by antiepileptic drugs. *Neuron* 91: 1305–1315.

184. Paramo, T., P. Brown, M. Musgaard, D. Bowie, and P. C. Biggin. 2017. Functional validation of heteromeric kainate receptor models. *Biophysical Journal* 113: 2173-2177.

185. Ramaswamy, S. S., D. M. MacLean, A. A. Gorfe, and V. Jayaraman. 2013. Proton-mediated conformational changes in an acid-sensing ion channel. *Journal of Biological Chemistry* 288: 35896-35903.

186. Litwin, D. B., R. Durham, and V. Jayaraman. 2019. Single molecule FRET methods to study glutamate receptors. Glutamate receptors. *Methods in Molecular Biology* 1941: 3-16.

187. Hadzic, M. C. A. S., R. Börner, S. L. B. König, D. Kowerko, and R. K. O. Sigel. 2018. Reliable state identification and state transition detection in fluorescence intensity-based single-molecule förster resonance energy-transfer data. *Journal of Physical Chemistry B* 122: 6134–6147.

188. Oswald, R. E. 2007. Flexibility of a glutamate-binding domain. *Cell* 15: 1157-1158.

189. Fenwick, M. K., and R. E. Oswald. 2010. On the mechanisms of amino-3-hydroxy-5-methylisoxazole-4-propionic acid (AMPA) receptor binding to glutamate and kainate. *The Journal of Biological Chemistry* 285: 12334-12343.

190. Dutta, A., J. Krieger, and I. Bahar. 2015. Cooperative dynamics of intact AMPA and NMDA glutamate receptors: Similarities and subfamily-specific differences. *Structure* 23: 1692-1704.

191. Krieger, J., I. Bahar, and I. H. Greger. 2015. Structure, dynamics, and allosteric potential of ionotropic glutamate receptor n-terminal domains. *Biophysical Journal* 109: 1136-1148.

192. Krieger, J., J. Y. Lee, I. H. Greger, and I. Bahar. 2018. Activation and desensitization of ionotropic glutamate receptors byselectively triggering pre-existing motions. *Neuroscience Letters*.

193. Porter, R. H. P., S. L. Eastwood, and P. J. Harrison. 1997. Distribution of kainate receptor subunit mrnas in human hippocampus, neocortex and cerebellum, and bilateral reduction of hippocampal GluR6 and KA2 transcripts in schizophrenia. *Brain research* 751: 217-231.

194. Barberis, A., S. Sachidhanandam, and C. Mulle. 2008. GluR6/KA2 kainate receptors mediate slow-deactivating currents. *The Journal of Neuroscience* 28: 6402– 6406.

195. Fisher, J. L., and D. D. Mott. 2011. Distinct functional roles of subunits within the heteromeric kainate receptor. *The Journal of Neuroscience* 31: 17113–17122

196. Fisher, M. T., and J. L. Fisher. 2014. Contributions of different kainate receptor subunits to the properties of recombinant homomeric and heteromeric receptors. *Neuroscience* 278: 70-80.

197. Stern-Bach, Y., S. Russo, M. Neuman, and C. Rosenmund. 1998. A point mutation in the glutamate binding site blocks desensitization of AMPA receptors. *Neuron* 21: 907-918.

198. Sun, Y., R. Olson, M. Horning, N. Armstrong, M. Mayer, and E. Gouaux. 2002. Mechanism of glutamate receptor desensitization. *Nature* 417: 245-253.

199. Gonzalez, J., M. Du, K. Parameshwaran, V. Suppiramaniam, and V. Jayaraman. 2010. Role of dimer interface in activation and desensitization in AMPA receptors. *Proc Natl Acad Sci U S A* 107: 9891-9896.

200. Litwin, D. B., E. Carrillo, S. A. Shaikh, V. Berka, and V. Jayaraman. 2019. The structural arrangement at intersubunit interfaces in homomeric kainate receptors. *Scientific Reports* 9: 6969.

201. Jr, F. G., S. M. Ball, and E. Molnar. 2003. Assembly and cell surface expression of KA-2 subunit-containing kainate receptors. *Journal of Neurochemistry* 86: 141-1427.

202. Hayes, D. M., S. Braud, D. E. Hurtado, J. McCallum, S. Standley, J. T. Isaac, and K. W. Roche. 2003. Trafficking and surface expression of the glutamate receptor subunit, ka2. *Biochemical and Biophysical Research Communications* 310: 8-13.

203. Ma-Högemeier, Z. L., C. Körber, M. Werner, D. Racine, E. Muth-Köhne, D. Tapken, and M. Hollmann. 2010. Oligomerization in the endoplasmic reticulum

and intracellular trafficking of kainate receptors are subunit-dependent but not editing-dependent. *Journal of Neurochemistry* 113: 1403-1415.

204. Ayalon, G., and Y. Stern-Bach. 2001. Functional assembly of AMPA and kainate receptors is mediated by several discrete protein-protein interactions. *Neuron* 31: 103-113.

205. Pardo, J. J. D. 2015. Solubilization of membranes by styrene maleic acid (SMA) results in formation of nanodiscs with retention of native lipid composition. *Biophysical Journal* 108.

206. Smirnova, I. A., P. Ädelroth, and P. Brzezinski. 2018. Extraction and liposome reconstitution of membrane proteins with their native lipids without the use of detergents. *Scientific Reports* 8.

207. Malumbres, M., and M. Barbacid. 2003. Ras oncogenes: The first 30 years. *Nature Reviews Cancer* 3: 459–465.

208. Schubbert, S., K. Shannon, and G. Bollag. 2007. Hyperactive RAS in developmental disorders and cancer. *Nature Reviews Cancer* 7: 295–308.

209. Mazhab-Jafari, M. T., C. B. Marshall, M. J. Smith, G. M. C. Gasmi-Seabrook, P. B. Stathopulos, F. Inagaki, c. Lewis E. Kay, d Benjamin G. Neel, and M. Ikuraa. 2015. Oncogenic and rasopathy-associated K-RAS mutations relieve membrane-dependent occlusion of the effector-binding site. *Proceedings of the National Academy of Sciences USA* 112: 6625–6630.

210. Prakash, P., Y. Zhou, H. Liang, J. F. Hancock, and A. A. Gorfe. 2016. Oncogenic K-RAS binds to an anionic membrane in two distinct orientations: A molecular dynamics analysis. *Biophysical Journal* 110: 1125–1138.

211. Gorfe, A. A., M. Hanzal-Bayer, D. Abankwa, J. F. Hancock, and J. A. McCammon. 2007. Structure and dynamics of the full-length lipid-modified H-RAS protein in a 1,2-dimyristoylglycero-3-phosphocholine bilayer. *Journal of Medical Chemistry* 50: 674–684.

212. Cao, S., S. Chung, S. Kim, Z. Li, D. Manor, and M. Buck. 2019. K-RAS g-domain binding with signaling lipid phosphatidyl inositol (4,5) phosphate (PIP2): Membrane association, protein orientation and function. *Journal of Biological Chemistry*.

213. Jain, A., R. Liu, B. Ramani, E. Arauz, Y. Ishitsuka, K. Ragunathan, J. Park, J. Chen, Y. K. Xiang, and T. Ha. 2011. Probing cellular protein complexes using single-molecule pull-down. *Nature* 473: 484-488.

214. Wang, Y., Y. Liu, H. A. DeBerg, T. Nomura, M. T. Hoffman, P. R. Rohde, K. Schulten, B. Martinac, and P. R. Selvin. 2014. Single molecule FRET reveals pore size and opening mechanism of a mechano-sensitive ion channel. *eLife* 3.

215. Mujoo, H., J. N. J. Reynolds, and I. G. Tucker. 2018. A real-time in vitro assay to evaluate the release of macromolecules from liposomes. *Drug Testing and Analysis* 10: 1025-1032.

216. Waterhouse, A., M. Bertoni, S. Bienert, G. Studer, G. Tauriello, R. Gumienny, F. T. Heer, T. A. P. d. Beer, C. Rempfer, L. Bordoli, R. Lepore, and T. Schwede. 2018. Swiss-model: Homology modelling of protein structures and complexes. . *Nucleic Acids Res*.

217. Webb, B., and A. Sali. 2016. Comparative protein structure modeling using modeller. *Current Protocols in Bioinformatics*.

218. Mott, H. R., J. W. Carpenter, and S. L. Campbell. 1997. Structural and functional analysis of a mutant RAS protein that is insensitive to nitric oxide activation. *Biochemistry* 36: 3640–3644.

Vita

Douglas Bryan Litwin was born in Houston, Texas, the son of Bruce Douglas Litwin and Mary Bryan Litwin. After completing his work at Humble High School, Humble, Texas in 2002, he entered the University Houston-Downtown in Houston, Texas. During this time, he was introduced to basic science research after being given the opportunity to head a research project in the laboratory of Philip Lyons, PhD. He also participated in a geophysical research project in the laboratory of Penny Morris-Smith, PhD and Donald Musselwhile, PhD. He received the degree of Bachelor of Science with a major in Biological and Physical Sciences from the University Houston-Downtown in May, 2011. He spent the following year working as a laboratory technician at the University of Texas Health Science Center at Houston-School of Dentistry in the laboratory of Millicent Goldschmidt, PhD. In the fall of 2012, he began a Master of Science program at the University of Texas Health Science Center at Houston in the Department of Microbiology and Molecular Genetics in the laboratory of Heidi Kaplan, PhD. After completing his Master's degree in Microbiology and Molecular Genetics in 2014, he began a PhD program in the Department of Biochemistry and Molecular biology the University of Texas Health Science Center in the laboratory of Vasanthi Jayaraman, PhD.